Experimentelle Physik
Kern- und Teilchenphysik

High precision measurement of the η meson mass at COSY - ANKE

Inaugural-Dissertation
zur Erlangung des Doktorgrades
der Naturwissenschaften im Fachbereich Physik
der Mathematisch-Naturwissenschaftlichen Fakultät
der Westfälischen Wilhelms-Universität Münster

vorgelegt von

Paul Goslawski

aus Beuthen

- Münster 2013 -

Dekan:	Prof. Dr. Markus Donath
Erster Gutachter:	Prof. Dr. Alfons Khoukaz
Zweiter Gutachter:	Prof. Dr. Johannes P. Wessels

Tag der Disputation:
Tag der Promotion:

Zusammenfassung

Frühere Messungen an verschiedenen Großforschungsanlagen zur Bestimmung der η-Mesonmasse lieferten hochpräzise Ergebnisse, die sich jedoch um mehr als acht Standardabweichungen voneinander unterscheiden, d.h. $0.5\,\mathrm{MeV/c^2}$. Bemerkenswert dabei ist, dass im Gegensatz zu den jüngsten "Invariant Mass" Experimenten insbesondere zwei "Missing Mass" Experimente, bei denen das η-Meson im $^3\mathrm{He}\,\eta$ Endzustand produziert wurde, zu kleineren Massenwerten abweichen. Das Ziel der neuen Messung an COSY-ANKE war daher die uneindeutige Massensituation zu klären. So wurde in einem verfeinerten "Missing Mass" Experiment die Produktionsschwelle der Reaktion $\mathrm{d\,p} \to {}^3\mathrm{He}\,\eta$, die direkt von der η-Masse abhängt, bestimmt. Dies gelang durch die Messung eines schwellennahen Datensatzes von zwölf Deuteronstrahlimpulsen und den dazugehörigen ^{3}He-Endzustandsimpulsen der Reaktion $\mathrm{d\,p} \to {}^3\mathrm{He}\,X$. Die η-Produktion wurde dabei durch Berechnung der "Missing Mass" klar identifiziert. Für die Messung der einzelnen Strahlimpulse wurde ein polarisierter COSY-Deuteronenstrahl durch eine künstlich erzeugte Spinresonanz, die bei eindeutig definierten Umlauffrequenzen auftritt, depolarisiert. Mit dieser Methode wurden die Strahlimpulse um $3\,\mathrm{GeV/c}$ mit einer bis daher noch nicht erreichten Genauigkeit von 3×10^{-5} bestimmt. Die einfache Kinematik der Zwei-Teilchen-Reaktion $\mathrm{d\,p} \to {}^3\mathrm{He}\,\eta$ und die vollständige geometrische Akzeptanz von ANKE für die gewünschte Reaktion ermöglichten eine sehr genaue Kalibrierung des Vorwärtsdetektorsystems und somit eine genaue Bestimmung der ^{3}He-Endzustandsimpulse. Bei der Kalibrierung wurde die Impulskugel des $^3\mathrm{He}\,\eta$ Endzustandes auf ihre Symmetrie untersucht. Aufgrund der vollständigen geometrischen Akzeptanz für den gesamten Raumwinkelbereich wurde die Abhängigkeit des ^{3}He-Endzustandsimpulses für alle Streuwinkel im Schwerpunktsystem untersucht. Insgesamt lieferte die COSY-ANKE Messung mit

$$m_\eta \;=\; (547.873 \;\pm\; 0.005_{\mathrm{stat.}} \pm 0.027_{\mathrm{syst.}})\,\mathrm{MeV/c^2}$$

somit weltweit den genauesten Wert der η-Masse. Während dieser Wert im Gegensatz zu den älteren "Missing Mass" Experimenten steht, stimmt er mit den Ergebnissen der "Invariante Masse" Experimente, in denen das Meson über seine Zerfallsprodukte nachgewiesen wurde, überein.

Abstract

Previous measurements of the η meson mass performed at different experimental facilities resulted in very precise data but differ by up to more than eight standard deviations, i.e., 0.5 MeV/c. Interestingly, the difference seems to be dependent on the measuring method: two missing mass experiments, which produce the η meson in the $^3\mathrm{He}\,\eta$ final state, deviate from the recent invariant mass ones. In order to clarify this ambiguous situation a high precision mass measurement was realised at the COSY-ANKE facility. Therefore, a set of deuteron laboratory beam momenta and their associated ^{3}He centre-of-mass momenta was measured in the $\mathrm{d\,p} \to {}^3\mathrm{He}\,X$ reaction near the η production threshold. The η meson was identified by the missing mass peak, whereas its mass was extracted by fixing the production threshold. The individual beam momenta were determined with a relative precision of 3×10^{-5} for values just above 3 GeV/c by using a polarised deuteron beam and inducing an artificial depolarising spin resonance occurring at a well-defined frequency. The final state momenta in the two-body reaction $\mathrm{d\,p} \to {}^3\mathrm{He}\,\eta$ were investigated in detail by studying the size of the ^{3}He momentum sphere with the forward detection system of the ANKE spectrometer. Final alignment and momentum calibration of the spectrometer was achieved by a comprehensive study of the ^{3}He final state momenta as a function of the centre-of-mass angles, taking advantage of the full geometrical acceptance. The value obtained for the mass at COSY-ANKE

$$m_\eta = (547.873 \pm 0.005_{\mathrm{stat.}} \pm 0.027_{\mathrm{syst.}})\,\mathrm{MeV/c^2}$$

is therefore worldwide the most precise one. This mass value is contrary to earlier missing mass experiments but it is consistent and competitive with recent invariant mass measurements, in which the meson was detected through its decay products.

Contents

1. Introduction

Searching for the basic building blocks of matter and investigating the forces interacting between them are two main objectives of modern particle physics. First ideas that matter consists of indivisible, fundamental, and elementary particles were introduced in Ancient Greece. Since the end of the 19th century experiments confirmed a kind of basic component of matter, the atom, indicating at the same time its substructure composed of a dense, central, and positively charged nucleus surrounded by a cloud of negatively charged electrons. Further experiments of J.J. Thomson, E. Rutherford, and J. Chadwick identified the individual constituents beside electrons as protons and neutrons. According to the current state of knowledge the electron is an indivisible point-like particle, whereas proton and neutron show an internal structure consisting of quarks.

The development of the first particle accelerators, the Van-de-Graaff accelerator and the cyclotron of E. Lawrence in the 1930s, made it feasible to investigate by way of scattering experiments the proton and neutron structure in more detail. Unexpectedly, a lot of unknown, subatomic, short-lived and unstable particles named as hadrons and leptons were produced in these experiments.
The large number of hadrons is classified into two different groups: baryons consisting of three quarks and mesons consisting of a quark-antiquark pair, the latter including the η meson. Main research focal points of modern particle physics tend to understand physical processes and interactions between these particles on a length scale of $< 10^{-15}$ m. Therefore extensive investigations of particle properties are imperatively necessary. One of the most essential properties of a subatomic particle is its mass, often used in theoretical models and calculations. Hence an accurate knowledge of particle masses is of prime importance and can only be provided by high precision experiments.

Every year the Review of Particle Physics is published by an international collaboration, the Particle Data Group (PDG), summarising all published results of particle property measurements. Looking back to the year 2000 the PDG masses and uncertainties of the lightest pseudoscalar mesons barely changed with exception of the η meson mass. During last 20 years the PDG had to adjust the η mass value and its uncertainty four times, due to new experimental results. Currently the PDG [N+10] quotes a η mass value of

$$m_\eta = (547.853 \pm 0.024)\,\mathrm{MeV/c^2},$$

whereas in the review of 2006 [Y+06] the η meson mass value was still listed with $m_\eta = (547.51 \pm 0.18)\,\mathrm{MeV/c^2}$. Compared to other pseudoscalar mesons the precision differed by up to two orders of magnitude. The pion masses were known with a precision of $\Delta m_\pi/m_\pi \approx 10^{-6}$, the kaon masses with $\Delta m_K/m_K \approx 10^{-5}$, but the mass of the η meson was specified with a precision of $\Delta m_\eta/m_\eta \approx 10^{-4}$ only. The large uncertainty in 2006 and the variations of the PDG value in the last decade were originated by contradictory results of different experiments. Presently, results of experiments producing the η meson in the reaction

$$\mathrm{d\,p} \to {}^3\mathrm{He}\,\eta$$

differ by up to $\approx 0.5\,\mathrm{MeV/c}$ from the PDG value.

In order to clarify this unsatisfactory and ambiguous situation a new high precision η mass measurement was proposed in October 2007 [Kho07] via this reaction using the ANKE spectrometer [B+01] installed at COSY, the COoler SYnchrotron [Mai97] ring of the Forschungszentrum Jülich. This proposal was immediately accepted by the Program Advisory Committee of this facility and in March 2008 the measurement was realised in a four week long beam time.
By producing the η meson in a simple two-body reaction it was possible to deduce the mass exclusively from pure kinematics. In order to be competitive and comparable in accuracy with recent results two kinematic quantities had to be determined with a precision never reached at COSY-ANKE before: the beam momentum p_d of the deuteron beam stored in COSY and the ^{3}He final state momentum p_f measured with ANKE.

For the determination of the beam momentum a new technique was implemented at COSY, the so called resonant depolarisation technique or also named as spin-resonance method. It increased the reachable accuracy compared to the conventional one by more than one order of magnitude, i.e., $\Delta p/p < 10^{-4}$. Large parts of the beam momentum determination were carried out in a former Diploma thesis [Gos08]. Nevertheless, the analysis was finalised in the scope of this Phd thesis and the results were published [G+10].
For that reason, one main emphasis of this Phd thesis lies on the precise determination of the ${}^3\mathrm{He}\,\eta$ final state momentum defined in the centre-of-mass frame. Therefore, it was necessary in the analysis to clearly identify the reaction of interest, describe the background, carefully verify the detector calibration to gain a deeper understanding of the ${}^3\mathrm{He}\,\eta$ signal. In particular, it was indispensable to put a lot of effort to understand the resolution effects of the ANKE detector, which

influences the measuring process.
Finally, the COSY-ANKE experiment provides the world's best measurement for the η meson mass of

$$m_\eta = (547.873 \pm 0.005_{\text{stat.}} \pm 0.027_{\text{syst.}})\,\text{MeV/c}^2\ .$$

This result is in agreement with the current PDG estimation for the mass and the precision achieved is similar to those ones of recent experiments.

Briefly introducing the current situation of the η meson mass in Chapter 2, the measuring method and experimental apparatus are presented in Chapters 3 and 4. Chapter 5 shortly summarises the beam momentum determination, followed by a detailed description for the analysis of the final state momenta in Chapter 6. The η mass determination and its uncertainties are discussed in more detail in Chapter 7. Finally, the COSY-ANKE result is compared with those ones of other experiments in Chapter 8.

2. Nature of the η meson

By scattering experiments at particle accelerators since the 1930s scientists pushed forward to smaller length scales to investigate the basic building blocks of matter. Doing these experiments the η meson as well as a large number of other new subatomic particles were discovered named as leptons and hadrons. According to current knowledge leptons are indivisible, whereby hadrons are composite particles consisting of elementary quarks. Introducing the quark model Gell-Mann [GM62] and Zweig [Zwe64] grouped hadrons into baryons and mesons according to their quantum numbers. The quark model is derivable from the theory of strong interaction, i.e., quantum chromodynamics (QCD) explaining the interaction between quarks and gluons. QCD, the electroweak interaction and the Higgs mechanism are the main components of a more extensive model: "the standard model of particle physics". Up to the 1980s by the interplay of theoretical considerations and experimental results in particle physics the standard model was developed describing the elementary particles and the forces acting among them.

In the following sections the standard model and quantum chromodynamics will be shortly introduced. Afterwards in context of the quark model the η meson properties will be discussed with main focus on the particle mass.

2.1. Standard model and quantum chromodynamics

The standard model of particle physics is a relativistic quantum field theory describing three of the four known fundamental forces of nature acting between elementary particles. The fundamental interactions are gravitation, electromagnetic interaction, and finally the weak nuclear and the strong nuclear forces. Above the unification energy electromagnetic and weak interactions are unified in electroweak theory. The gravitation is not considered in the standard model. On the length scale of particle physics gravity is many orders of magnitude weaker than the other forces and therefore negligible.

In the standard model the fundamental forces among elementary matter particles known as fermions are described by the exchange of force mediating particles known as gauge bosons. Figure 2.1 shows the indivisible particles of the standard model. According to the spin-statistics theorem particles with half integer spin are fermions and those with integer spin are bosons. The force carrying gauge bosons, which represent the action of force fields, are generated by a special property of fermions: called charge. The massless photon transmits the electromagnetic interaction among electrically charged particles, which is described by the quantum electrodynamics (QED). The massive $W^{\pm}$, Z^0 gauge bosons act as carrier of the weak interaction between particles with weak isospin. The eight massless gluons mediate the strong interaction between colour-charged particles, i.e., quarks and gluons. In contrast to the other force mediating particles gluons carry colour-charge. Consequently, they interact strongly among themselves.

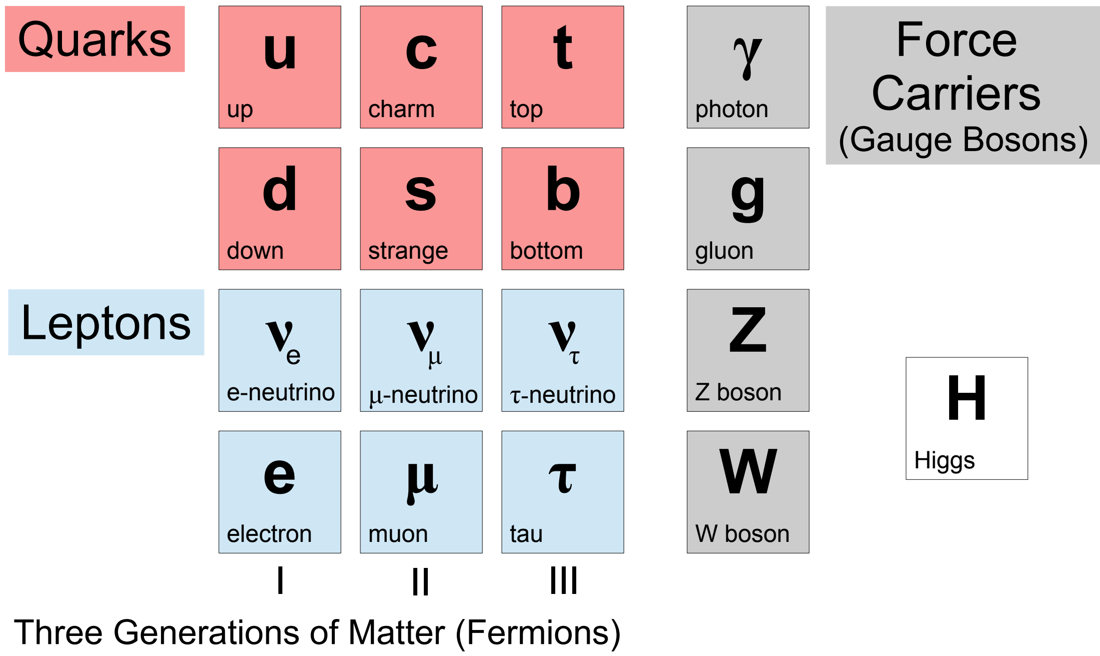

Figure 2.1.: The elementary particles of the standard model are grouped into fermions, the force mediating gauge bosons, and the higgs boson. (Fermions are grouped into six quarks and six leptons.)

According to quantum field theory, there is an associated antiparticle to each particle with identical mass and spin, but exactly opposite additive quantum numbers[1]. That means there are associated antileptons and antiquarks corresponding to the fundamental fermions.

[1] Additive quantum numbers are for example electric charge, colour charge, lepton or baryon number. Particles with additive quantum numbers equal zero are their own antiparticles, like the η meson or the photon.

Predicted in 1964 by P. Higgs, F. Englert, and R. Brout [Hig64, EB64] the scalar Higgs boson is an elementary particle with zero spin which had not been observed experimentally for a long time. The Higgs mechanism, i.e., the scalar higgs field, was introduced as part of the Standard model in order to explain why the gauge bosons of weak interaction ($W^{\pm}$, Z^0) have mass in contrast to the photon in QED. Furthermore, this methodology can explain the origin of the mass of elementary fermions.
From 2011 to the end of 2012 two experiments, ATLAS and CMS, placed at the Large Hadron Collider (LHC) at CERN, collected a lot of data from proton proton collisions searching for the higgs boson. At the end of 2012 the two experiments announced the discovery of a new particle with a mass of $\approx 125\,\mathrm{GeV/c^2}$ which might be the higgs introduced in the standard model [ATL12, CMS12].

The twelve elementary fermions listed in Table 2.1 are grouped into three generations or families of matter with four particles. Each generation contains two quarks and two leptons. The strongly interacting quarks have different flavour and fractional electric charge. The two leptons consist of a charged one (e, μ, τ) and the associated neutrino (ν_e, ν_μ, ν_τ), which interacts weakly only. The different generations are characterised by different mass ranges. Particles of the second and third generation are often referred as heavier copies of particles of the lightest one. The basic components of atoms forming the existing baryonic matter surrounding us are the charged particles of the first generation, i.e., up-quark, down-quark, and the electron.

Quark	Charge	Mass		**Lepton**	Charge	Mass	
u	$+2/3\ e$	$1.8 - 3.0$	$\mathrm{MeV/c^2}$	e	$-1\ e$	0.511	$\mathrm{MeV/c^2}$
d	$-1/3\ e$	$4.5 - 5.5$	$\mathrm{MeV/c^2}$	ν_e	0	< 2	$\mathrm{eV/c^2}$
c	$+2/3\ e$	$1.25 - 1.30$	$\mathrm{GeV/c^2}$	μ	$-1\ e$	105.7	$\mathrm{MeV/c^2}$
s	$-1/3\ e$	$90 - 100$	$\mathrm{MeV/c^2}$	ν_μ	0	< 0.19	$\mathrm{MeV/c^2}$
t	$+2/3\ e$	≈ 173.5	$\mathrm{GeV/c^2}$	τ	$-1\ e$	1776.8	$\mathrm{MeV/c^2}$
b	$-1/3\ e$	$4.15 - 4.21$	$\mathrm{GeV/c^2}$	ν_τ	0	< 18.2	$\mathrm{MeV/c^2}$

Table 2.1.: The three generations of elementary fermions, quarks, and leptons, with electrical charge and mass [N+10].

Due to their different interactions fundamental fermions are separated into quarks and leptons. Unlike all other elementary particles, only quarks and gluons interact strongly, described by QCD, a non-abelian quantum field theory. In QCD quarks have an additional quantum number called colour charge. It occurs in three different types, red, green, and blue. Antiquarks carry a corresponding anti-charge, like antired, antigreen, or antiblue. In contrast to the single electrical uncharged force carrier in QED, the photon, there are eight different colour-charged gauge bosons in QCD. These are the gluons possessing different colour and anticolour. Carrying colour gluons interact strongly among themselves leading to colour confinement, a special property of QCD. Colour confinement means that colour-charged particles like quarks cannot exist freely in nature, but only in colour-neutral or colourless systems confined with other quarks. Colour-neutral states can be formed by all three different colour or anticolour values or by the combination of a colour-anticolour pair. These bound quark systems are denoted as hadrons. Until now, all hadrons observed in experiments are colour-neutral. They are organised in baryons and mesons depending on how the colourless bound state is constructed.

Baryons or antibaryons consist of three quarks ($\mathrm{q\,q\,q}$) or antiquarks ($\bar{\mathrm{q}}\,\bar{\mathrm{q}}\,\bar{\mathrm{q}}$) with three different colour or anticolour charges forming a colourless bound system. Their spin is based on the half integer quark spin which can be combined to 1/2 or 3/2. By this baryons are fermions and obey the Pauli exclusion principle. The best-known baryons are the nuclear components, i.e., the proton consisting of ($\mathrm{u\,u\,d}$)-quarks and the neutron of ($\mathrm{u\,d\,d}$)-quarks.

Mesons are composed of a quark-antiquark pair ($\mathrm{q}\,\bar{\mathrm{q}}$) with colour and anticolour charge. Consequently, the spin is combined to 0 or 1. Thus, mesons are bosons. The π^+ meson is one example comprising an up-quark and a down-antiquark pair ($\mathrm{u}\,\bar{\mathrm{d}}$). Another example is the η meson consisting of a combination of the three lights quarks (u, d, s). According to the current state of knowledge the proton is the only stable hadron, whereas all others are unstable, decaying via the fundamental interactions into lighter particles.

According to QCD the inner structure of baryons and mesons is much more complex than described above as a three quark or a quark-antiquark system. In the framework of the quark model these quarks are called valence quarks, defining the quantum numbers of hadrons. Additionally to their valence quarks in QCD hadrons contain a large number of virtual gluons and virtual quark-antiquark pairs, called sea quarks, interacting with each other.

2.2. General properties of the η meson

The η particle is one of the mesons. In the quark model mesons are bound states of a quark-antiquark pair ($\mathrm{q}\,\bar{\mathrm{q}}$) with spin $s = 0$ (antiparallel quark spins) or $s = 1$ (parallel quark spins) determined by the combination of the quark spins. The total angular momentum $\vec{J}$ and the associated quantum number J are given by the spin $\vec{S}$ and the orbital angular momentum $\vec{L}$ via the relation

$$\vec{J} = \vec{S} + \vec{L} \qquad \text{with} \qquad |l - s| \leqslant J \leqslant |l + s| \ . \tag{2.1}$$

While states with orbital angular momentum $l = 0$ are ground states with lightest mass, those one with orbital excitation $l > 0$ are treated as excited states linked to higher masses. The abundance of different mesons is arranged by their quantum numbers J^{PC} in multiplets. The parity P and the charge conjugation C, or C-parity are given for mesons by

$$P = (-1)^{l+1} \qquad \text{and} \qquad C = (-1)^{l+s} \ . \tag{2.2}$$

C-parity is defined for neutral particles only, but it can be generalised to G-parity including charged particles. While states with $l = 0$ are denoted as pseudoscalar mesons $J^{PC} = 0^{-+}$ and vector mesons $J^{PC} = 1^{--}$, those ones with $l = 1$ are classified as scalar $J^{PC} = 0^{++}$, axial vector $J^{PC} = 1^{+\pm}$, and tensor mesons $J^{PC} = 2^{++}$.

The η meson has quantum numbers $J^{PC} = 0^{-+}$ and is assigned to the pseudoscalar mesons. Considering only the three lightest quark flavours $(\mathrm{u}, \mathrm{d}, \mathrm{s})$, nine different meson states or quark-antiquark combinations can be arranged. Mathematically the multiplication is described by the SU(3) flavour symmetry resulting in a anti-symmetric octet and a symmetric singlet of light quark meson states. This can be visualised in a weight diagram by plotting the strangeness versus the isospin. In Figure 2.2 it is depicted for the pseudoscalar mesons with $J^{PC} = 0^{-+}$. Particles with non vanishing strangeness are named as kaons, whereas the $(\mathrm{u}\,\bar{\mathrm{d}}), (\mathrm{d}\,\bar{\mathrm{u}})$ combinations are identified as π^+, π^- mesons. States in the centre of the diagram with same strangeness and isospin quantum numbers can interfere with each other.

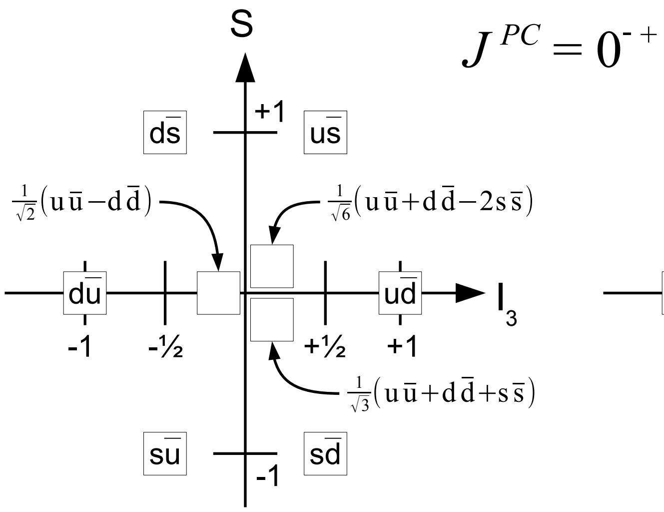

Figure 2.2.: Pseudoscalar mesons with quantum numbers $J^{PC} = 0^{-+}$.
Left: Theoretical states according to SU(3) flavour symmetry.
Right: Particles measured experimentally.

If the particles observed in experiments π^0, η and η' were pure eigenstates of the SU(3) flavour symmetry, they could be directly assigned to the three theoretical states. This is not the case because the quarks have different masses and so the flavour symmetry is broken. While the π^0 is assigned to the state $1/\sqrt{2}(\mathrm{u\bar{u}} - \mathrm{d\bar{d}})$, the η and η' are given as linear combinations of the theoretical states

$$\eta_0 = \frac{1}{\sqrt{3}}\left(\mathrm{u\bar{u}} + \mathrm{d\bar{d}} + \mathrm{s\bar{s}}\right) \qquad \text{and} \qquad \eta_8 = \frac{1}{\sqrt{6}}\left(\mathrm{u\bar{u}} + \mathrm{d\bar{d}} - 2\mathrm{s\bar{s}}\right) \ . \tag{2.3}$$

The values of the mixing angle θ published in literature differ from $\theta \approx -11°$ to $-20°$ [BLN90], depending on the determination method. However, using the average value of $\theta \approx -15°$ the quark content of the η meson is composed of 30% $(\mathrm{u}, \mathrm{\bar{u}})$, 30% $(\mathrm{d}, \mathrm{\bar{d}})$, and 40% $(\mathrm{s}, \mathrm{\bar{s}})$ quarks approximately. The η' particle contains 20% $(\mathrm{u}, \mathrm{\bar{u}})$, 20% $(\mathrm{d}, \mathrm{\bar{d}})$, and 60% $(\mathrm{s}, \mathrm{\bar{s}})$ quarks.

The electrically uncharged η meson cannot be measured experimentally in a direct way, because it is unstable decaying into lighter particles, mainly photons and pions. It has a very short mean life time of $\tau \approx 5 \times 10^{-19}$ s corresponding to a narrow decay width of $\Gamma = (1.30 \pm 0.07)$ keV. Due to energy and momentum conservation, it is possible to reconstruct the η meson produced in a reaction, using two different ways: the *missing mass* or the *invariant mass* method. Both approaches are described in the appendix in Section A.1 in detail.

The η meson decay proceeds via the strong and electromagnetic interaction, dominated by two neutral and two charged decay modes of about 99 % [N+10].

$$\begin{array}{lllllll}
\eta & \rightarrow & 2\gamma & & & \text{with} & 39.31\ \% \\
\eta & \rightarrow & 3\pi^0 & \rightarrow & 6\gamma & \text{with} & 32.57\ \% \\
\eta & \rightarrow & \pi^+\pi^-\pi^0 & & & \text{with} & 22.74\ \% \\
\eta & \rightarrow & \pi^+\pi^-\gamma & & & \text{with} & 4.60\ \%
\end{array}$$

The final state of the two neutral channels results in photons, because pions of the $3\pi^0$ channel mainly decay into two photons. Other decay channels are possible, too, but strongly suppressed. Furthermore, the η meson is suitable to study forbidden decay modes violating C-, P- or CP-parity. One example is shown by the search for the C-parity violating decay $\eta \rightarrow \pi^0 e^+ e^-$ by the WASA-at-COSY experiment [Ber09, Win11, Ber13].

Besides these features mentioned above, the mass is another fundamental property of a subatomic particle. The chronological development of the world average value of the η meson mass determined by the PDG is illustrated and listed for the last 50 years in Figure 2.3. Until 1990 the PDG had quoted a value of (548.8 $\pm$0.6) MeV/c^2, which then has decreased by about $1 - 1.5\,\mathrm{MeV/c^2}$ because of new measurements with better precision. Nevertheless, since 1992, the PDG had to correct its average mass value four times. It was only be excluding results of high precision experiments that in 2008 an accuracy comparable to other pseudoscalar mesons could be reached for the first time.

As mentioned at the beginning, the variations of the mass value over the last two decades are the consequence of contradictory outcomes of various experiments. The next section will emphasise the details by presenting the ambiguous results of the individual measurements. Finally the current situation of the η meson mass will be discussed.

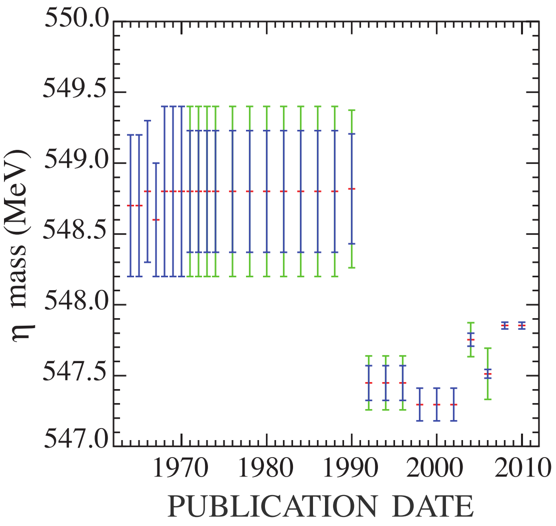

Publication Date	PDG values of the η mass / (MeV/c^2)
until 1990	548.800 ± 0.600
1992	547.450 ± 0.190
1997	547.300 ± 0.120
2003	547.750 ± 0.120
2006	547.510 ± 0.180
2008	547.853 ± 0.024

Figure 2.3.: Chronological development of the PDG estimation for η meson mass value [N+10].

2.3. Ambiguous results of η mass experiments

At the beginning of the 60s, when Gell-Mann and Zweig predicted the nonet of pseudoscalar mesons, other scientists at the Lawrence Radiation Laboratory in Berkley observed a new particle resonance in a bubble chamber experiment [P+61]. The signal appeared at a mass value of $\approx 546\,\mathrm{MeV/c^2}$ with a half-width at half maximum of $\leqslant 25\,\mathrm{MeV/c^2}$ consisting of 24 events only. It was identified as the pseudoscalar η meson. Shortly after the first observation of η mesons, the mass was measured with higher precision by using two different decay modes [B+62].

$$K^- + \text{p} \rightarrow \Lambda + \eta$$
$$\eta \rightarrow \pi^+ + \pi^- + \pi^0 \qquad m_\eta = (550.0 \pm 1.5)\,\text{MeV/c}^2$$
$$\eta \rightarrow \text{neutrals} \qquad m_\eta = (548.0 \pm 2.0)\,\text{MeV/c}^2$$

As depicted in Figure 2.3 the uncertainties of the PDG η mass value decreased over time which is due to the development of new detector technology. While in the 60s bubble chambers were used for particle detection reaching a precision of about $1\,\text{MeV/c}^2$ for mass determination, nowadays an accuracy better than one order of magnitude, i.e., better than $100\,\text{keV/c}^2$, is achieved by using more refined detector systems.

Figure 2.4 and Table 2.2 show the obtained η mass values of different experiments in chronological order. Earlier results of bubble chamber experiments are excluded, being too high by about $1\,\text{MeV/c}^2$ systematically.

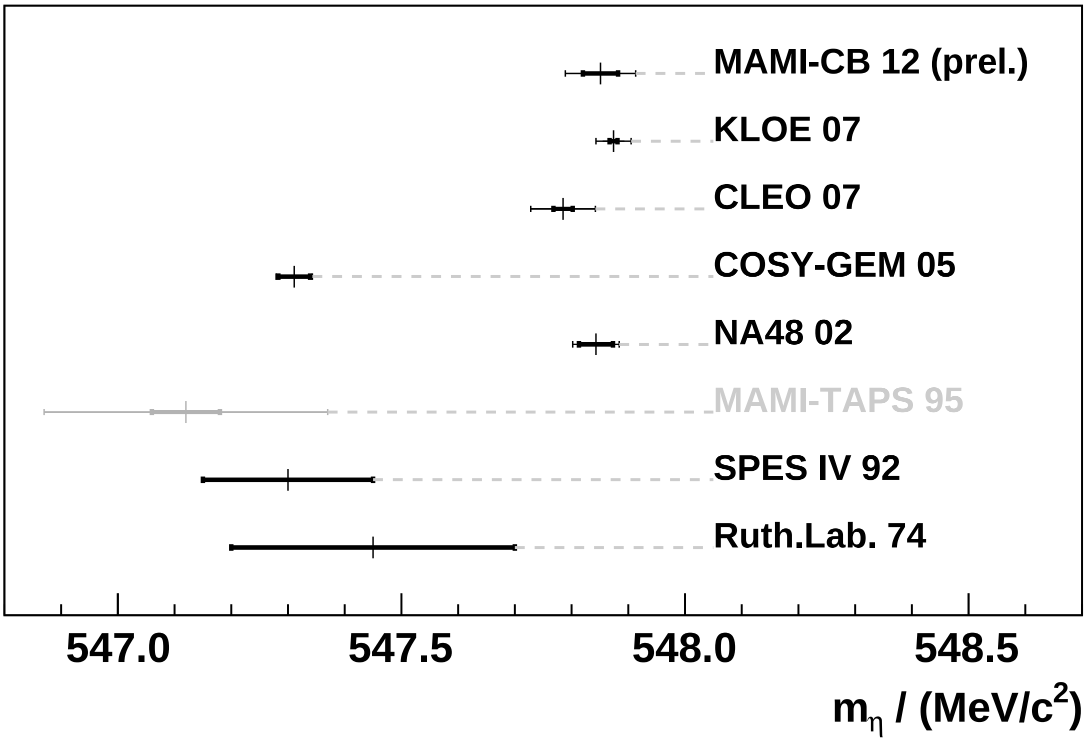

Figure 2.4.: Results of different η mass measurements in chronological order. Where two error bars are shown, the heavy line indicates the statistical uncertainty and the feint ones the systematic.

Year	Experiment	η mass (MeV/c^2)	Stat. error (MeV/c^2)	Syst. error (MeV/c^2)
2012	MAMI-CB (prel.) [Nik12]	**547.851**	0.031	0.062
2007	DAFNE-KLOE [A$^+$07b]	**547.874**	0.007	0.029
2007	CESR-CLEO [M$^+$07b]	**547.785**	0.017	0.057
2005	COSY-GEM [AB$^+$05]	**547.311**	0.028	0.032
2002	CERN/SPS-NA48 [L$^+$02]	**547.843**	0.030	0.041
1995	MAMI-TAPS [K$^+$95]	**547.120**	0.060	0.250
1992	SATURNE-SPES [P$^+$92]	**547.300**	0.150	
1974	Ruth.Lab. [D$^+$74]	**547.450**	0.250	

Table 2.2.: Results of different η mass measurements in chronological order. The experiment name comprises accelerator facility and detector used.

The MAMI-TAPS result coloured in grey will not be considered in the following discussion, because it is in contradiction to the new MAMI-CB measurement. The new one is submitted but not published yet [Nik11]. The calibration of the incident photon energy during the first experiment is suspected to be the reason for the disagreement, so the authors say [Nik12].

Although the measurement uncertainties decreased over the last years, the individual η mass results deviate by about 550 keV/c^2 and fluctuate in between 547.3 MeV/c^2 to 547.9 MeV/c^2. Recent experiments of MAMI-CB, KLOE, CLEO, and NA48, which agree within their uncertainty limits of below 60 keV/c^2, refer to the higher η mass value, whereas earlier ones done by Rutherford Laboratory[2], SPES IV, and COSY-GEM point to the lower value. The variations of the PDG estimation were mainly caused by the disagreement of about ten standard deviations of the first very precise results of NA48 and COSY-GEM.

The origin for this disagreement of the obtained η mass values is unknown and a widely discussed issue in the community. One speculative but possible explanation is that different mass determination methods could lead to inconsistent η mass results. Unconsidered effects could be provoked by the use of various reactions. The eight various experiments determining the η mass are based on three different types of mass measurements, discussed in the next section.

[2] The result of the Rutherford Laboratory is abbreviated in tables and figures as "Ruth.Lab".

2.4. Three different kinds of η mass determination

The individual experiments comprise three different kinds of methods for mass determination.

1. Invariant mass technique (NA48, CLEO, KLOE): In this case the η mass is deduced directly from the mean value of the invariant mass distribution of its decay products.

2. Interpolation of total cross sections to threshold (MAMI): Once the production threshold is determined, the mass can be extracted from kinematic quantities defined by the threshold.

3. Missing mass technique (Rutherford Laboratory, SPES IV, COSY-GEM): In this case the η meson is produced in a two-body reaction and reconstructed by calculating the missing mass. The mass is determined by the mean value of the missing mass distribution.

In the next sections the different methods will be described. Their advantages and disadvantages will be discussed. Further and more detailed informations can be found in the cited literature.

2.4.1. Invariant mass technique

The η meson was produced in various reactions at NA48, CLEO, and KLOE [L$^+$02, M$^+$07b, A$^+$07b] and the decay products, pions and photons were detected. The η mass was determined by calculating the invariant mass distribution of the decay products.

At the NA48 experiment a π^- beam was scattered on two thin polyethylene targets and the charge exchange reaction $\pi^-\,\mathrm{p} \to \eta\,\mathrm{n}$ was investigated. The η meson was clearly identified using the decay into $3\,\pi^0$ only, whereby each pion decays mainly into two photons. All six photons were detected with the liquid krypton calorimeter. By that 1134 η meson events could be reconstructed.

Using the $\psi(2S) \to \eta\,J/\psi$ decay at the CLEO detector a data sample of around 16000 η events were collected for mass determination. The $\psi(2S)$ charmonium state was produced by electron-positron scattering. By detecting the lepton-antilepton pair (electron-positron or muon-antimuon) of the J/ψ decay and all four main η decay channels listed in Section 2.2 the events could be clearly identified.

At the KLOE experiment, installed at the electron-positron collider DAΦNE, a ϕ meson factory, the η meson was produced via the decay channel $\phi \to \gamma\,\eta$. For mass determination η events decaying into two photons were taken into account only. The photons were measured with the lead/scintillating-fibre sampling calorimeter.

The accuracy of this mass determination relies mainly on the detection of the decay products, photons, and pions. Especially, their energy and momentum have to be reconstructed with highest precision. Therefore the calibration of the electromagnetic calorimeters has to be understood and studied carefully. It is needed for the precise photon detection of the two dominating neutral decay channels. In contrast to other methods, this one has the advantage that the kinematic variables of the initial state, e.g., the beam energy, do not have to be considered.

2.4.2. Interpolation of total cross sections to threshold

Doing the MAMI (MAinzer MIcrotron) experiments [K$^+$95, Nik12] the η meson was also reconstructed via the invariant mass of its decay products, however the mass was deduced in a completely different way. The η meson was produced by photoproduction at a proton $\gamma\,\mathrm{p} \rightarrow \mathrm{p}\,\eta$ close to reaction threshold in these two experiments. The reaction threshold is defined by the minimum initial state energy, which is necessary for producing the particles of the final state, in this case the η meson. By fixing the photon energy at threshold E_γ^{thr} the η mass m_η can be deduced via the relation [K$^+$95]

$$E_\gamma^{\mathrm{thr}} = m_\eta + \frac{m_\eta^2}{2m_p}\ , \tag{2.4}$$

where m_p is the proton mass. For a precise determination of the threshold the absolute number of produced η mesons, i.e., the total cross sections, as function of the photon energy had to be determined. The energy of each photon was measured with the Glasgow Photon Tagging-System. Therefore the incident monoenergetic electron beam with energy E_0 provided by the mainzer microtron was scattered at a radiator foil for producing high energy photons with energy E_γ through bremsstrahlung. After having penetrated the radiator foil the degraded electrons were deflected by a spectrometer magnet and detected in the tagger microscope, an array of plastic scintillators, to determine the residual electron energy E_{e^-}. Since the energy transferred to the nuclei of the radiator foil is negligible, the photon energy is directly given by $E_\gamma = E_0 - E_{e^-}$. Obviously the accuracy of the photon energy depends on the precision of E_0 and E_{e^-}.

In the same manner as at the invariant mass experiments, described in Section 2.4.1, the η meson was reconstructed by detection of its decay products. In the two experiments photons of the two neutral decay modes into 2γ or $3\pi^0 \rightarrow 6\gamma$, were measured. In the earlier experiment this was done by the TAPS detector and in the newer one by the Crystall Ball/TAPS detector. Total cross sections were obtained as function of the photon energy in the threshold vicinity. They were interpolated to threshold to determine the η mass. The interpolation of the cross sections requires a theoretical model to describe the excitation function and its contributions of s-, p-, and d-wave amplitudes of η-photoproduction close to threshold. Whereas the MAMI-TAPS experiment determined a mass of $m_\eta = 547.12\,\mathrm{MeV/c^2}$ the new MAMI-CB quotes a value of $m_\eta = 547.851\,\mathrm{MeV/c^2}$. One possible origin of mismatch is suspected to be the energy calibration of the Tagging-System [Nik12].

In contrast to invariant mass experiments the described method requires the control of a larger number of crucial quantities. The result is very sensitive to the photon energy measured with the Tagging-System, which depends on the incident electron energy and the energy measured after the bremsstrahlung process. In addition the behaviour of the excitation function close to threshold, i.e., the theoretical model, has to be very well understood for describing the total cross sections. And the determined cross section values, in turn, depend on a lot of experimental parameters as for example the detector acceptance and efficiency, and the luminosity calculated by photon flux and target thickness.

2.4.3. Missing mass technique

Rutherford Laboratory (Rutherford Laboratory), SATURNE-SPES and COSY-GEM studied hadronic two-body reactions at fixed target experiments [D$^+$74, P$^+$92, AB$^+$05]. The η mesons produced were identified through a missing mass peak by measuring the kinematic quantities of initial and final state. When doing fixed target experiments it is clear that the kinematics of the initial state is completely defined by the momentum of the beam. The η mass was deduced from the mean value of the missing mass distribution.

The prime objective of the Rutherford Laboratory experiment was the determination of decay width and mass of the η' meson. However, the η mass was measured as cross check on the equipment only. That means the η meson was produced in the fixed target reaction $\pi^-\,\mathrm{p} \to \eta\,\mathrm{n}$, where the neutrons were detected and the beam momentum was measured macroscopically to high precision using the floating wire technique [D$^+$74][3].

At SATURNE-SPES a deuteron beam was scattered on a fixed liquid hydrogen target to investigate the reaction

$$\mathrm{d\,p} \to {}^3\mathrm{He}\,\eta$$

[3] More detailed explanations are provided by the references therein.

close to threshold. The ^{3}He nuclei were detected by the high resolution double-focussing but small acceptance, SPES IV spectrometer. Due to the limited acceptance it was solely possible to measure forward and backward ($\cos\vartheta = \pm 1$) scattered ^{3}He nuclei in the centre-of-mass frame. Both, the beam momentum and spectrometer settings, were calibrated by the measurement of three additional two-body reactions with well known final states ($^3\mathrm{He}\,\pi^0$, $^3\mathrm{H}\,\pi^+$, $p\,d$) and masses. For each final state the first particle only was detected by the spectrometer. Investigating these three reactions the magnetic field of the spectrometer and the beam momentum had to be adjusted for each one because of the small spectrometer acceptance.

The COSY - GEM experiment studied the same final state $^3\mathrm{He}\,\eta$ produced by scattering a proton beam on a fixed liquid deuterium target

$$\mathrm{p\,d} \rightarrow {}^3\mathrm{He}\,\eta \;.$$

The method for mass determination is very similar to that one of SATURNE-SPES. By studying one additional two-body reaction $\mathrm{p\,d} \rightarrow {}^3\mathrm{H}\,\pi^+$ with well known final state in two different situations ($\pi^+\,{}^3\mathrm{H}$, $^3\mathrm{H}\,\pi^+$), the beam momentum as well as the spectrometer were calibrated and the target thickness was determined. For the two different situations the first particle only was detected with the spectrometer. In contrast to SATRUNE-SPES the used spectrometer BIG KARL had a much larger acceptance. This allows to study the two reactions of interest at one proton beam momentum of $p_p \approx 1641\,\mathrm{MeV/c}$ simultaneously. Nevertheless, particles in forward and backward direction only were detected. In consideration of the target thickness the η mass was deduced from the missing mass peak.

Compared to the η mass determination of photoproduction experiments, the missing mass ansatz is based on pure kinematics of a two-body reaction and therefore completely model independent. As well as the invariant mass technique[4] the method relies exclusively on the measurement of kinematic quantities, but in addition to the final state the initial one has to be taken into account, too. Therefore the momenta of the accelerator beam and of the particle produced together with the η meson have to be measured with high precision. This requires an accurate calibration of the detector, mostly a magnetic spectrometer.

2.5. Evaluation of the current η mass situation

Table 2.3 shows the η mass results of various experiments, techniques for mass determination, and reactions used. Curiously, it seems that the obtained value is

[4] The invariant mass technique is described in Section 2.4.1.

dependent on the mass determination method or even on how the η meson was reconstructed at the experiment.

Experiment	Technique and reaction	m_η / (MeV/c^2)
MAMI-CB (prel.)[Nik12]	Photoproduction: $\gamma\, \mathrm{p} \to \eta\, \mathrm{p}$	$547.851\ ^{\pm 0.031}_{\pm 0.062}$
DAFNE-KLOE [A+07b]	Invariant Mass: $\phi \to \gamma\, \eta$	$547.873\ ^{\pm 0.007}_{\pm 0.029}$
CESR-CLEO [M+07b]	Invariant Mass: $\psi(2S) \to \eta\, J/\psi$	$547.785\ ^{\pm 0.017}_{\pm 0.057}$
COSY-GEM [AB+05]	**Missing Mass: $\mathbf{p\, d \to {}^3He\, \boldsymbol{\eta}}$**	$\mathbf{547.311}\ ^{\pm 0.028}_{\pm 0.032}$
CERN/SPS-NA48 [L+02]	Invariant Mass: $\pi^-\, \mathrm{p} \to \eta\, \mathrm{n}$	$547.843\ ^{\pm 0.030}_{\pm 0.041}$
SATURNE-SPES [P+92]	**Missing Mass: $\mathbf{d\, p \to {}^3He\, \boldsymbol{\eta}}$**	$\mathbf{547.300} \pm 0.150$
Ruth.Lab. [D+74]	Missing Mass: $\pi^-\, \mathrm{p} \to \eta\, \mathrm{n}$	547.450 ± 0.250

Table 2.3.: Results for the η mass of the various experiments, reaction studied, and technique used for mass determination. Where two uncertainties are given the upper one indicates the statistical error and the lower one the systematic one.

The invariant mass experiments NA48, CLEO and KLOE, as well as the photoproduction experiment MAMI-CB, obtained consistent results to high accuracy and point to a higher value. In all these measurements the η meson was reconstructed by its decay products. However, all missing mass experiments Rutherford Laboratory, SATURNE-SPES and COSY-GEM reported a lower value of about 550 keV/c^2 for the mass (see Figure 2.4). When taking into account invariant mass experiments only, the PDG get their best estimation for the η mass as

$$m_\eta^{\mathrm{PDG}} = (547.853 \pm 0.024)\,\mathrm{MeV/c^2}\ . \tag{2.5}$$

In this case results of missing mass experiments are completely excluded and neglected. It is important to note that the MAMI-CB result was not considered by the PDG because it was not published at this time.

Assuming that the reason for the disagreement is caused by the missing mass experiments, then two explanations are possible:

1. There might be unknown and unconsidered systematic effects or errors at the measurement or analysis of the kinematic quantities of initial and final state.
2. Or physical process might have influence on the mass measurement.

In the first case the beam energy could be poorly determined, though this was done using different techniques for the three experiments. Another reason might be that the spectrometers have been insufficiently well calibrated.

In the second case it might be that physical process could have impact on the mass measurement. Worth noting is the fact that SATURNE-SPES and COSY-GEM, which have used the reaction $\mathrm{d\,p\,(p\,d)} \to {}^3\mathrm{He}\,\eta$, obtain a low η mass value of $m_\eta \approx 547.3\,\mathrm{MeV/c^2}$ to high precision. Maybe there is something peculiar about the reaction or the final state ${}^3\mathrm{He}\,\eta$. One possible cause might be that the multi pion background below the η peak could have been slightly distorted by a strong coupling of, e.g., $\eta\,{}^3\mathrm{He} \rightleftharpoons \pi\pi{}^3\mathrm{He}$. This would influence the missing mass distribution leading to a wrong or shifted η mass identification [Kho07].

A previous measurement of the reaction $\mathrm{d\,p} \to {}^3\mathrm{He}\,\eta$ at COSY-ANKE indicated already an unexpected behaviour of the excitation function near threshold [M$^+$07a, R$^+$09, Mer07, Rau09] (see Section 3.2.1). This measurement was specially dedicated to investigate the interaction between ^{3}He nucleus and η meson. Compared to phase space the total cross section shows a strong enhancement close to threshold. This could be described only by a very strong final state interaction implying a possible formation of a ${}^3\mathrm{He}\,\eta$ quasi bound state [W$^+$07]. Though highly speculative, one further possibility might be an influence on mass measurement by forming such a state of matter.

2.6. Motivation for a new η mass measurement

All considerations about the ambiguous η mass situation led to the conclusion to pursue a new mass measurement. Furthermore, various investigations of physical phenomena involving the η meson motivate a new mass measurement. Two examples will be presented in the following.

The interpretation of η meson production experiments close to threshold, as mentioned in the previous section, requires a precise knowledge of the mass value. In the mid-80s a bound state between η meson and nucleus, the so called η-mesic nucleus, was predicted by two physicists [HL86]. Since then a lot of various experiments were carried out to confirm such a state of matter. The search is going on and further experiments are planned and carried out today (e.g., [G$^+$11, K$^+$12]). In some of these researches the η nucleus system, such as $\eta\,{}^4\mathrm{He}$, $\eta\,{}^3\mathrm{He}$, and $\eta\,d$, was produced close to threshold to measure total and differential cross sections. Described by a final state interaction ansatz the scattering length and the pole position of the η nucleus system were extracted, providing information about the strength of the interaction. Since both quantities are dependent on the determined excess energy and by that on the η mass, a precise knowledge of this value is important in order to ensure a comparable interpretation of different results.

Besides η meson production close to threshold, the exploration of η decays depends strongly on the mass value. One example is the G-parity forbidden decay: $\eta \rightarrow 3\pi^0$. It is caused by an isospin violating part of the QCD Lagrangian, which is proportional to $m_d - m_u$, so it is possible to determine the u, d quark mass difference investigating this decay. Theoretical approaches provide predictions about the dalitz plot event distribution of the decay, which can be measured in experiments. The dalitz plot can be described by one single kinematic variable z and a quadratic slope parameter α, representing the difference of the event density from phase space. Since the kinematic variable z is affected by the η mass value, a precise knowledge is necessary for comparing various results. Different mass values would influence the result for α as it is shown in [A$^+$07a].

However, as shown in Figure 2.4 and Table 2.3, the situation of the η meson mass is ambiguous and could only be clarified by the performance of a much more precise missing mass experiment using the reaction $\mathrm{d\,p} \rightarrow {}^3\mathrm{He}\,\eta$.
Consequently, it was the objective of the COSY-ANKE mass measurement presented in this PhD thesis to provide an η mass value that is comparable in accuracy, i.e., $\Delta m_\eta \approx 50\,\mathrm{keV/c^2}$, to those that used the invariant mass technique [L$^+$02, M$^+$07b, A$^+$07b]. The obtained result will confirm or refute the previous $\mathrm{d\,p\,(p\,d)} \rightarrow {}^3\mathrm{He}\,\eta$ measurements of SATURNE-SPES and COSY-GEM. In the following chapter the mass determination method used at the COSY-ANKE experiment will be described in detail.

3. Method for mass determination at COSY-ANKE

The chosen approach for mass determination at COSY-ANKE differs from other missing mass experiments thats why it will be explained in the following sections. First the kinematics of a two-body reaction will be discussed in general. Afterwards the peculiarities of the reaction used $\mathrm{d\,p} \to {}^{3}\mathrm{He}\,\eta$ will be presented, focussing on the crucial points when determining the ^{3}He final state momentum.

3.1. Relativistic kinematics

It is for sure that relativistic effects cannot be neglected at high-energy scattering experiments, because the involved particles are moving with velocities close to the speed of light. Relativistic processes are most conveniently described in the Minkowski spacetime, a four dimensional real vector space. The kinematic variables are chosen in a way to simplify the mathematical transformation when changing the frame of reference (see Section 3.1.1). As usual in particle physics the "natural units" with $\hbar = c = 1$ will be applied in this thesis.

In relativistic kinematics a particle with energy E and classical three-momentum vector $\vec{p}$ is entirely defined by its four momentum vector

$$\mathbb{P} = (E, \vec{p}) = (E, p_x, p_y, p_z) \ . \tag{3.1}$$

Due to Minkowski metric the absolute value or the norm of the four momentum is given by

$$m_{\mathrm{inv}}^2 = \mathbb{P}^2 = E^2 - \vec{p}^{\,2} \ , \tag{3.2}$$

where m_{inv}^2 is designated as invariant mass. This quantity is constant in all frames of reference related by Lorentz transformation. According to the relativistic energy momentum relation for a free particle

$$E^2 = m_0^2 + p^2 \tag{3.3}$$

the invariant mass can be directly assigned to the particle's rest mass m_0.

3.1.1. Laboratory system and centre-of-mass frame

It is well known that fixed target experiments at accelerators are mainly mathematically discussed in two particular frames of reference, the laboratory system (LS) and the centre-of-mass (CM) frame. Figure 3.1 shows the transformation of the particles' four momenta between these two frames of reference for a two-body reaction a + b → c + d at a fixed target. The accelerator beam axis is usually chosen to define the z-axis of the coordinate system.

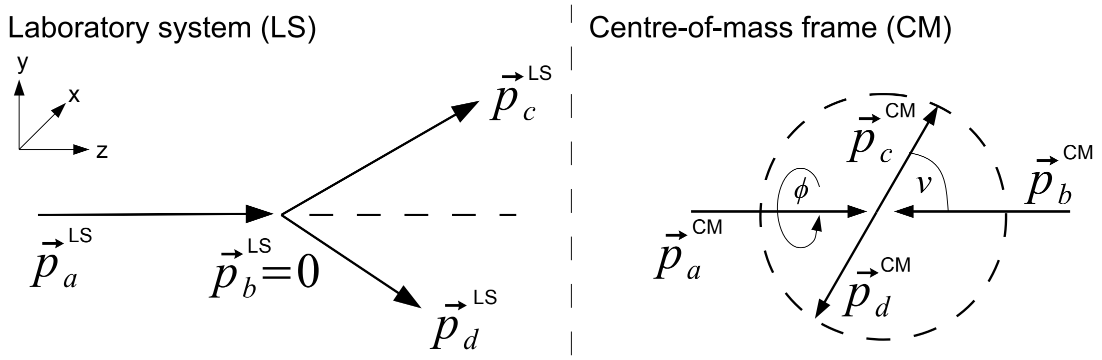

Figure 3.1.: Two-body reaction a + b → c + d shown in the laboratory frame (LS) and centre-of-mass (CM) one. The momenta can be expressed in cartesian or spherical coordinates with the polar angle ϑ and the azimuthal angle ϕ.

The four momenta of the particles involved are measured and reconstructed in the LS frame by the detection setup. In the LS frame the velocity of the centre-of-mass $\vec{\beta}$ is given by the relation

$$\vec{\beta} = \vec{p_a}^{\mathrm{LS}} / E_{\mathrm{tot}}^{\mathrm{LS}} \ , \tag{3.4}$$

with the beam momentum $\vec{p_a}^{\mathrm{LS}}$ and the total energy $E_{\mathrm{tot}}^{\mathrm{LS}} = E_a^{\mathrm{LS}} + E_b^{\mathrm{LS}}$ of the initial state. By definition the total momentum of the initial state in the CM frame is equal zero

$$\vec{p_a}^{\mathrm{CM}} + \vec{p_b}^{\mathrm{CM}} = 0 \ . \tag{3.5}$$

Thereby the CM is at rest, which simplifies the description of reaction kinematics. The four momentum components are transformed into the CM frame by the Lorentz transformation with $\gamma = 1/\sqrt{1-\beta^2}$:

$$\begin{aligned} p_{x,y}^{\mathrm{CM}} &= p_{x,y}^{\mathrm{LS}} \\ p_z^{\mathrm{CM}} &= \gamma \left(p_z^{\mathrm{LS}} - \beta E^{LS} \right) \\ E^{\mathrm{CM}} &= \gamma \left(E^{\mathrm{LS}} - \beta p_z^{LS} \right) \ . \end{aligned} \tag{3.6}$$

Wheras the x and y momentum components are equal in both frames of reference, the z components is transformed exclusively.

3.1.2. Kinematics of a two-body reaction

The kinematics of a two-body reaction $\mathrm{a} + \mathrm{b} \to \mathrm{c} + \mathrm{d}$ with the particle a, b in the entrance channel and c, d in the output one, as illustrated in Figure 3.1, is entirely described by the particles' four momentum vectors. According to energy and momentum conservation the sum of the four momenta of initial-state is equal to that one of the final one

$$\mathbb{P}_a + \mathbb{P}_b = \mathbb{P}_c + \mathbb{P}_d \ . \tag{3.7}$$

The total energy $\sqrt{s}$ or the CM energy of the reaction is defined by the Mandelstam variable s, given by the square of the four momentum sum of the incoming or outgoing particles

$$\begin{aligned} s &= (\mathbb{P}_a + \mathbb{P}_b)^2 = (\mathbb{P}_c + \mathbb{P}_d)^2 \\ &= (E_a + E_b)^2 - (\vec{p_a} + \vec{p_b})^2 \ . \end{aligned} \tag{3.8}$$

In a fixed-target experiment the target particle b is at rest and the total energy depends on the masses of the initial state particles and on the momentum of the accelerated one. In the final state the overall CM energy is given by the masses of the outgoing particles and their total kinetic energy Q, that is also denoted as excess energy

$$\sqrt{s} = m_c + m_d + Q \ . \tag{3.9}$$

The reaction threshold is defined for the case $Q = 0$, in which the collision of the two initial particles provide just enough energy to generate the masses m_c and m_d. As a result of that the outgoing particles are at rest in the CM frame. For excess energies $Q > 0$ the momenta of particles c and d are described in the CM frame in the most simple way, according to Equation (3.5) and due to momentum conservation:

$$\vec{p_a} + \vec{p_b} = \vec{p_c} + \vec{p_d} = 0 \ . \tag{3.10}$$

For a two-body reaction, as indicated in Figure 3.1, the CM momenta of the outgoing particles point into opposite direction, having the same length. They are distributed on a perfectly symmetric momentum sphere with constant radius $p_f = |\vec{p_c}| = |\vec{p_d}|$ named as final state momentum

$$p_f = \frac{\sqrt{\left[s - (m_c + m_d)^2\right]\left[s - (m_c - m_d)^2\right]}}{2\sqrt{s}} \ . \tag{3.11}$$

The final state momentum depends on the CM energy and the particle masses of the output channel only. The excess energy is directly linked to the final state momentum via the reduced mass $1/m_{\text{red.}} = 1/m_c + 1/m_d$ of the final state by this non relativistic approximation

$$Q = \frac{p_f^2}{2\,m_{\text{red}}} = \frac{p_f^2}{2\,(m_c + m_d)} \ . \tag{3.12}$$

3.2. Determination of the η meson mass using the reaction $\mathrm{d\,p} \to {}^3\mathrm{He}\,\eta$

The common missing mass experiments [P+92, AB+05] determined the η meson mass by studying the reaction $dp\,(pd) \to {}^3\mathrm{He}\,\eta$ and measuring the relevant kinematic variables, i.e., the momenta of the accelerated beam and the recoiling ^{3}He, at a single fixed energy. A much more effective and robust way to measure the mass relies on the identification of the reaction threshold, the chosen approach for COSY-ANKE experiment.

In the reaction $\mathrm{d\,p} \to {}^3\mathrm{He}\,\eta$ a deuteron of the accelerated beam fuses with a target proton to form a ^{3}He nucleus. In addition to that an η meson is produced. At a scattering experiment, this process occurs exclusively if the collision of the initial state particles provides enough CM energy, given by Equation (3.8), to generate the masses of the final state. For a fixed target experiment the CM energy relies on the masses of the incoming particles and on the momentum p_d of the accelerated deuteron beam

$$s(p_d) = 2m_p\sqrt{m_d^2 + p_d^2} + m_d^2 + m_p^2 \ . \tag{3.13}$$

By setting the beam momentum, the CM energy is defined, consequently the excess energy Q, too, as well as the the final state momentum p_f, according to Equations (3.9) and (3.11)

$$Q(s) = \sqrt{s} - m_{^3\mathrm{He}} - m_\eta \tag{3.14}$$

$$p_f(s) = \frac{\sqrt{\left[s - (m_{^3\mathrm{He}} + m_\eta)^2\right]\left[s - (m_{^3\mathrm{He}} - m_\eta)^2\right]}}{2\sqrt{s}} \ . \tag{3.15}$$

Using the expression for the CM energy (see Equation 3.13) both quantities, Q and p_f, become functions of the beam momentum.

If a measurement could fix the reaction threshold, $Q(p_d) = 0$ or $p_f(p_d) = 0$, then the η mass can be directly determined from knowledge of the beam momentum at threshold p_d^{thr} according to Equations (3.13) and (3.14)

$$m_\eta = \sqrt{2m_p\sqrt{m_d^2 + {p_d^{\mathrm{thr}}}^2} + m_d^2 + m_p^2} - m_{^3\mathrm{He}} \ . \tag{3.16}$$

At threshold the precision for mass determination is enhanced because

$$dm_\eta/dp_d \approx 0.24/c \ . \tag{3.17}$$

Using the PDG η mass value in Equation (3.16), a threshold beam momentum of $p_d^{\mathrm{thr}} = (3141.603 \pm 0.100)$ MeV/c is associated therewith. The particle masses with uncertainties needed for this calculation are listed in Table 3.1. These values were taken from "The National Institute of Standards and Technology" (NIST) [MTN12] for the nuclei and from the PDG [N$^+$10] for the η meson. At this point it is important to note that the nucleus masses and not the atomic ones have to be used in simulations as well as calculations in order to obtain correct results.

Particle	Mass m / (MeV/c^2)
Deuteron d	1875.612859 ± 0.000041
Proton p	938.272046 ± 0.000021
Helion ^{3}He	2808.391482 ± 0.000062
Eta meson η	547.853 ± 0.024

Table 3.1.: The masses of the particles involved in the reaction $\mathrm{d\,p} \rightarrow {}^3\mathrm{He}\,\eta$ are listed as stated in [MTN12] for nuclei and in [N$^+$10] for the η meson.

Inserting the two "possible" η mass values into Equation (3.16), this points out that the beam momenta at threshold differ by about 2.5 MeV/c:

1. $m_\eta \approx 547.3\,\mathrm{MeV/c^2} \quad \leftrightarrow \quad p_d^{\mathrm{thr.}} \approx 3139.3\,\mathrm{MeV/c}$
2. $m_\eta \approx 547.9\,\mathrm{MeV/c^2} \quad \leftrightarrow \quad p_d^{\mathrm{thr.}} \approx 3141.8\,\mathrm{MeV/c} \quad .$

That means in a new mass measurement the beam momentum at threshold has to be determined with a precision much better than that. In order to achieve an accuracy comparable to the PDG value, i.e., $\approx 30\,\mathrm{keV/c^2}$ the threshold momentum must be measured with an error of $\approx 100\,\mathrm{keV/c}$.

A direct measurement of the beam momentum at threshold would be the simplest way to determine the η mass, because in this case all systematic effects linked to the analysis of the reaction would be cancelled out. That means just contributions of the beam momentum determination have to be taken into consideration. Since it is impossible to measure the reaction threshold in a real experiment directly, the value has to be fixed by extrapolation of measurable quantities.
The MAMI experiments [K$^+$95, Nik12] realised the determination of threshold by extrapolating total cross sections of the photoproduction as explained in detail in Section 2.4.2. This approach is strongly model dependent, because it relies on an accurate theoretical description of the excitation function close to threshold. It cannot be straightforward transferred to the $\mathrm{d\,p} \to {}^3\mathrm{He}\,\eta$ reaction. It is because of the unusual behaviour of its excitation function, that will be discussed in the following section.

By focusing on pure kinematic quantities like the final state and beam momentum the reaction threshold can be tagged in a much simpler and model independent manner when extrapolating several (p_d, p_f) data points. According to Equations (3.13) and (3.15) the final state momentum is a function of the beam momentum, the η mass, and other well-measured masses[1]

$$p_f = p_f(p_d, m_\eta) \ . \tag{3.18}$$

In Figure 3.2 this relation, i.e., the final state momentum and its square, is plotted against the laboratory beam momentum from threshold to an excess energy of $Q \approx 15\,\mathrm{MeV}$ for different η mass values. The figures indicates that the final state momentum rises similar to a root function with increasing beam momentum. It shows that the reaction threshold shifts to higher beam momenta for higher η mass values.
The method to measure the η mass at COSY-ANKE is based on the determination of the production threshold by investigating the increase of the final state momentum as function of the beam momentum. This requires to measure the two kinematic quantities at several different energies close to threshold.

The precision of such an η mass measurement is dependent on accuracy and position of the measured (p_d, p_f) data set. When selecting the energies and consequently the data points measured in the beam time, the total cross section and the acceptance of the ANKE detection system for the reaction of interest must be taken into consideration. Both quantities affect the statistics collected during the beam time and consequently the precision of the final state momentum.

[1] The values for the particle masses involved are listed in Table 3.1.

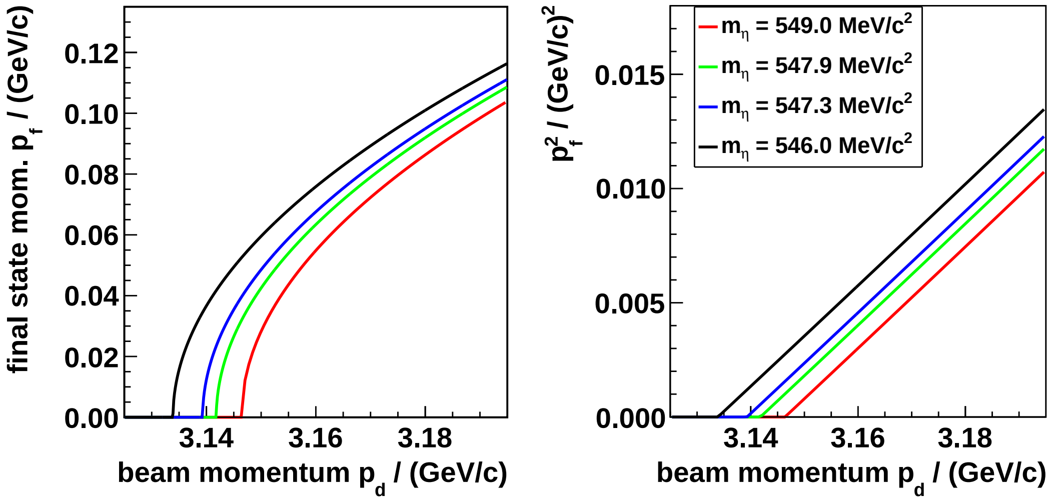

Figure 3.2.: The final state momentum p_f and its square p_f^2 are presented as function of the laboratory beam momentum p_d for four different η mass values.

3.2.1. Previous studies of the $\mathrm{d\,p} \to {}^3\mathrm{He}\,\eta$ reaction at COSY-ANKE

In two previous experiments[2] the reaction $\mathrm{d\,p} \to {}^3\mathrm{He}\,\eta$ was already subject of intense research at COSY-ANKE. Especially the energy region close to production threshold was examined aiming to investigate the $\eta\,{}^3$He nucleus interaction. By the use of a continuous beam momentum ramp from $Q \approx -5\,\mathrm{MeV}$ to $Q \approx 11\,\mathrm{MeV}$ with respect to the η reaction threshold total and differential cross sections were determined to highest precision [M$^+$07a, Mer07]. In addition data were recorded at fixed beam momenta at $Q = 20, 40,$ and $60\,\mathrm{MeV}$ in order to cover higher excess energies [R$^+$09, Rau09]. The analysis revealed that the ANKE spectrometer has full geometrical acceptance up to an excess energies of $Q < 15\,\mathrm{MeV}$ for the reaction of interest. The obtained total cross section close to threshold is depicted in Figure 3.3.

Assuming pure phase space behaviour and s-wave scattering the differential cross section $d\sigma/d\Omega$ for a two-body reaction close to threshold could be expressed as ratio of the final to initial state CM momenta p_f/p_i, multiplied by a constant production amplitude f

$$\frac{d\sigma}{d\Omega} = \frac{p_f}{p_i} \cdot |f|^2 \,. \tag{3.19}$$

[2] The 1st beam time was conducted in January 2005 with an unpolarised deuteron accelerator beam and the 2nd in October 2007 with a polarised deuteron beam. In the following the results of the January beam time will be discussed.

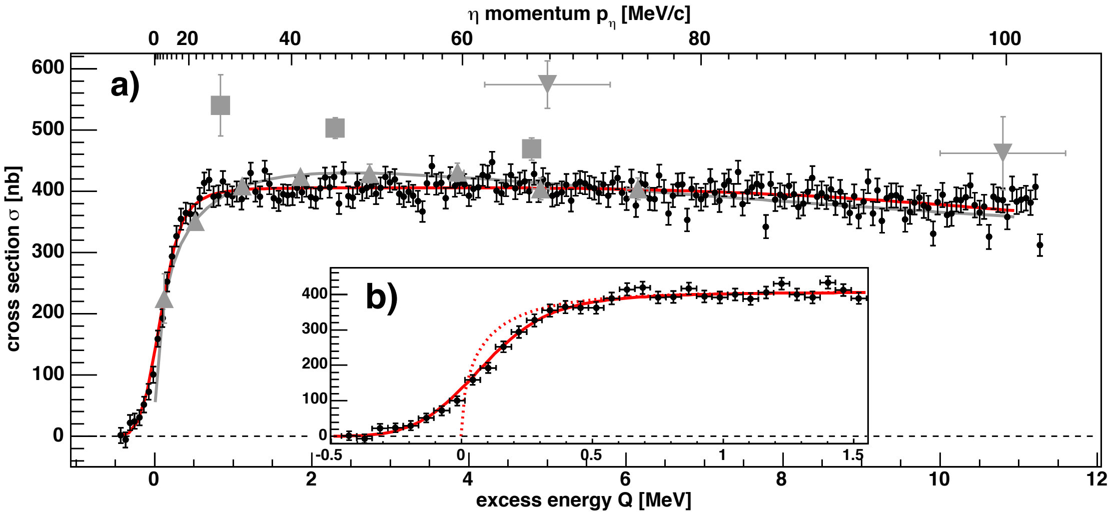

Figure 3.3.: **a)** Total cross section of the reaction $\mathrm{d\,p} \rightarrow {}^3\mathrm{He}\,\eta$ measured at COSY-ANKE (black circles) from threshold to $Q \approx 11\,\mathrm{MeV}$, described by a FSI ansatz (red curve).
b) The inset enlarges the near threshold data showing the influence of the beam momentum spread. The dotted curve presents the FSI description corrected for the beam momentum spread [M+07a].

In the threshold vicinity the final state momentum rises rapidly, whereas the initial one is nearly constant. For phase space behaviour the cross section is expected to increase with $\sqrt{Q}$, since the final state momentum is proportional to $\sqrt{Q}$ according to Equation (3.12).
The cross section of the ANKE measurement differs completely from phase space, rising steeply within the first MeV above threshold to its plateau value of $\approx 400\,\mathrm{nb}$. Then it remains nearly constant up to $Q = 100\,\mathrm{MeV}$. This behaviour is showing a very strong final state interaction (FSI) introduced by a separation ansatz of the production amplitude $|f|^2 = |f_c|^2 \cdot |f_{\mathrm{fsi}}|^2$ with a constant contribution f_c and an energy dependent FSI term f_{fsi}. The strength of the FSI is expressed by the values for the complex scattering length a and the effective range r_0 or alternatively by the two poles p_1 and p_2

$$f_{\mathrm{fsi}} = \frac{1}{1 - iap_f + 1/2 r_0 a p_f^2} = \frac{1}{(1 - p_f/p_1) \cdot (1 - p_f/p_2)} \,. \tag{3.20}$$

The fit to the data provides a large absolute value for the scattering length $|a|$ which implies a very strong FSI [M+07a]. This might lead to a possible formation of a quasi-bound or virtual $\eta\,{}^3\mathrm{He}$ state [W+07]. In order to verify the FSI interpretation, further analysis are going on of data taken with a polarised deuteron beam $\vec{d}p \to {}^3\mathrm{He}\,\eta$. The objective is to explore the non-s-wave contributions and the spin dependence of the entrance channel on the excitation function [K+06, Pap13].

Additional measurements were proposed to explore the $d\,n \to {}^3\mathrm{H}\,\eta$ and $p\,n \to d\,\eta$ reactions aiming to investigate the ${}^3\mathrm{H}\,\eta$ and $d\,\eta$ final state interaction [G+11, K+12, Sch13]. This will complete the studies of the η nucleus interaction program at COSY and it should help to clarify the question in which nuclei the η meson might be bound.

The data recorded with a continuously ramped beam allowed to tag the reaction threshold $Q = 0\,\mathrm{MeV}$. This was done by extrapolating the excess energy or final state momentum as a function of the time information of the linearly ramped beam. The production threshold was identified in the time ramp with an uncertainty of $\Delta t \approx 0.16\,\mathrm{s}$, that corresponds to an uncertainty of the excess energy at threshold of $\Delta Q_{\mathrm{thr}} = 9\,\mathrm{keV}$ [Kho07, Mer07]. According to Equation (3.16) this value would translate directly into the uncertainty of the η mass when knowing exactly the beam momentum. Due to the fact that the beam momentum measurement was performed with the conventional method in 2005, an accuracy of only $\Delta p_d/p_d = 10^{-3}$ could be achieved, i.e., $\Delta p_d \approx 3\,\mathrm{MeV/c}$ for momenta at $p_d = 3\,\mathrm{GeV/c}$. So the excellent threshold measurement could not be translated into an accurate value of the η mass. The large uncertainty of the beam momentum leads to an uncertainty in the mass of $\Delta m_\eta \approx 720\,\mathrm{keV/c^2}$.

In order to achieve a mass value at COSY-ANKE comparable in accuracy with results of recent experiments, i.e., $\Delta m_\eta \approx 50\,\mathrm{keV/c^2}$, it was necessary to increase the precision of the beam momentum determination by an order of magnitude to $\Delta p_d/p_d = 10^{-4}$.
This task was realised by using the so called resonant depolarisation technique or spin-resonance method exploiting the spin dynamics of a polarised beam. The technique is based on the resonant depolarisation of a polarised beam with an artificial spin resonance induced by a horizontal radio frequency magnetic field of a solenoid. It was applied for the first time at COSY to a vector polarised deuteron beam during an ordinary beam time. The COSY beam momentum determination will be described in detail in Chapter 5, starting with the explanation of the underlying physical principle in Section 5.1.

However, it is worth noting that this method is solely applicable to beams stored at a fixed energy in COSY. That is why it cannot be used for beams continuously ramped in momentum. Only the start and stop momenta of the ramp could be determined, so that momenta in between would have to be calculated. This requires information not easily accessible, e.g., the variation of the absolute orbit length during the momentum ramp. Using the beam positions monitors the absolute orbit length cannot be measured with sufficient precision. A much more detailed

discussion about advantages and disadvantages of measuring at fixed energies or with a momentum ramp can be found in [Gos08].
During the η mass beam time the reaction $\mathrm{d\,p} \to {}^3\mathrm{He}\,\eta$ was studied at several fixed energies. By that the beam momentum was measured individually for each data point using the resonant depolarisation technique.

The work of T. Mersmann [Mer07, M$^+$07a] showed that a high precision η mass measurement is in principle feasible at COSY-ANKE. But therefore new techniques and analysis methods that go beyond the conventional ones had to be implemented and developed. It initiated a lot of ideas and analysis methods, which were used for the mass measurement.
One approach was to use the simple kinematics of a two body reaction to verify and improve the detector calibration. This method was developed further and pursue consequently in the analysis of the η mass beam time in order to guarantee a correct final state momentum determination. It is discussed in detail in Chapter 6. The basic ideas and most crucial steps in the final state momentum analysis are introduced in Section 6.1.

3.2.2. Achievable precision of threshold extrapolation

Having discussed the method to measure the η mass at COSY-ANKE in the previous sections, it is clear that the precision and position of the measured data set (p_d, p_f) will specify the accuracy of the extrapolation to threshold and by that the accuracy of the obtained η mass value. The different data points were chosen in an excess energy range from $Q = 1 - 11\,\mathrm{MeV}$, because in this range ANKE has full geometrical acceptance. In addition the total cross section is well known and constant as shown in Figure 3.3. This allows to collect similar statistics, even very close to threshold, without expending excessive measuring time. Although it would increase the precision of the threshold determination, it would be pointless to take data even closer to threshold, i.e., below $Q = 1\,\mathrm{MeV}$, because here the total cross section shows very strong variations and the beam momentum spread must be taken into account. Small variations of the beam momentum could imply a shift below threshold, so no data of the reaction $\mathrm{d\,p} \to {}^3\mathrm{He}\,\eta$ would be recorded for this energy setting.

In order to achieve the best possible accuracy, the amount and positions of the individual beam momenta were optimised using Monte Carlo simulations. The simulations showed that a robust threshold determination is feasible by using twelve beam momenta, which are listed in Table 3.2. The two possible η mass values were reconstructed with nearly same precision [Gos08] by the threshold fit. The uncertainties for final state and beam momenta assumed in simulations are based on results of previous and preparatory measurements, which will be explained in the following.

Data Points	Beam momentum p_d / (MeV/c)	Q / (MeV) for $m_\eta = 547.3\,\mathrm{MeV/c^2}$	Q / (MeV) for $m_\eta = 547.9\,\mathrm{MeV/c^2}$
1	3146	1.6	1.0
2	3147	1.8	1.2
3	3148	2.1	1.5
4	3150	2.6	2.0
5	3152	3.0	2.4
6	3154	3.5	2.9
7	3158	4.5	3.9
8	3162	5.4	4.8
9	3167	6.6	6.0
10	3171	7.6	7.0
11	3176	8.8	8.2
12	3183	10.5	9.9

Table 3.2.: The chosen beam momenta for the η mass measurement at COSY-ANKE and the associated excess energies are listed for the two "possible" η mass values.

For the first feasibility test of beam-energy calibration using the resonant depolarisation technique [S$^+$07b, S$^+$07a], a deuteron beam was used at a nominal beam momentum of $p_d = 3118\,\mathrm{MeV/c}$ close below the $\mathrm{d\,p} \to {}^3\mathrm{He}\,\eta$ reaction threshold. It showed that the precision in momentum was increased by more than an order of magnitude to $\Delta p_d/p_d < 5 \times 10^{-5}$ in comparison to the conventional momentum determination[3]. The beam momentum was measured with an uncertainty of below 100 keV/c, i.e., $p_d = (3115.98 \pm 0.09)\,\mathrm{MeV/c}$. It deviated up to 2 MeV/c from the desired value. In Monte Carlo simulations a constant uncertainty for all twelve energy settings (see Table 3.2) was assumed. This is reasonable because it is not expected that the precision changes strongly in the narrow beam momentum range of $p_d = 3100 - 3200\,\mathrm{MeV/c}$. For a conservative estimation of the precision of the η mass determination, an uncertainty of

$$\Delta p_d = 150\,\mathrm{keV/c} \tag{3.21}$$

[3] Conventionally the beam momentum is calculated by the nominal orbit length and revolution frequency.

was used in Monte Carlo simulations. It is important to note that the first beam-energy calibration at COSY was carried out under optimised conditions, i.e., all influences on the beam during the cycle were reduced. Therefore, the ANKE cluster-jet target was switched off as well as all cavities after acceleration. By that an unbunched coasting beam was used for the first beam-energy calibration using the spin-resonance measurement.

The estimation of uncertainties for final state momenta is based on outcomes of the analysis of data recorded with the continuously ramped beam [Mer07]. During this beam time nearly 400000 $^3\mathrm{He}\,\eta$ events were collected from threshold to $Q \approx 11\,\mathrm{MeV}$ and subdivided into 200 bins. Each bin contains 2000 η events. As result of the high statistics and a precise calibration of the ANKE forward detector system, the final state momenta were reconstructed for each bin with an statistical uncertainty of below 400 keV/c. For the η mass beam time it was expected to record ten times more statistics, i.e., 20000 $^3\mathrm{He}\,\eta$ events for each of the twelve data points. This would lead to a decrease of the uncertainty to $\approx$ 130 keV/c. As for the beam momenta a more conservative value of

$$\Delta p_f = 150\,\mathrm{keV/c} \tag{3.22}$$

was used in Monte Carlo simulations.

Figure 3.4 presents the threshold extrapolation and thus the η mass determination for Monte Carlo simulated data. In this simulations the PDG η mass value was chosen and the twelve different beam momenta according to Table 3.2 were used. The final state momentum (black) and its square (red) are plotted against the deuteron laboratory beam momentum. The horizontal and vertical error bars, discussed above, are so small that they fall within the symbols. The extrapolation to threshold is performed with Equations (3.13) and (3.15) in which the η mass is chosen as free fit parameter. An additional scaling factor S is introduced by multiplying the right hand side of Equation (3.15) $p_f = p_f(p_d, m_\eta, S)$ in order to reduce the sensitivity of the method to systematic errors in the spectrometer calibration. The next subsection will give reasons for introducing the scaling parameter and its significance for the analysis will be motivated.
When using the "function minimisation and error analysis" package MINUIT of ROOT[4] the least square fit to the data reproduces the η mass assumed in simulations with an uncertainty of below 25 keV/c. The precision of the extracted mass

[4] ROOT is a framework programmed in C/C++ with all the functionality needed to analyse large amounts of data in a very efficient way. It is standard for analysis of nuclear and particle experiments. More informations at `http://root.cern.ch` .
The software framework for extracting physics at ANKE, the ROOTSORTER, is also based on ROOT. It was extended by an additional software package named "Reconstruction" for simplifying the event analysis [Pap13, Mie13].

is practically almost independent of the value used in simulations. The difference of 600 keV/c^2 referring to two "possible" mass values presented in Table 3.2 causes a change in uncertainty of 3 keV/c^2.

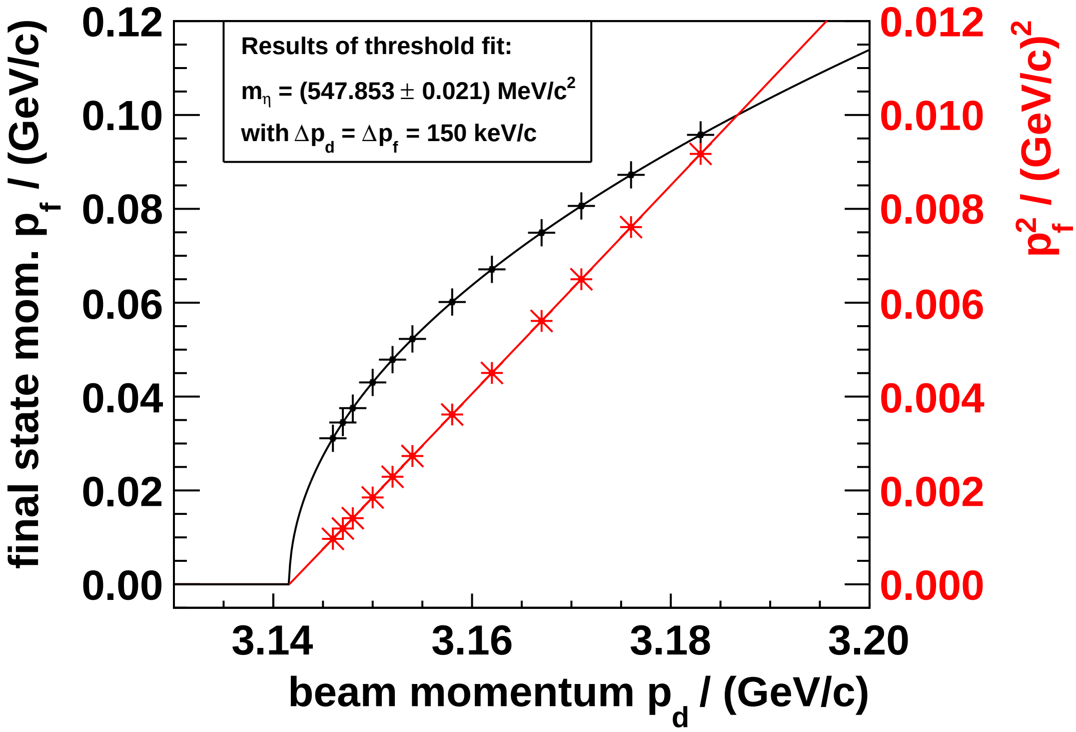

Figure 3.4.: Determination of the η mass through the identification of the $\mathrm{d\,p} \to {}^3\mathrm{He}\,\eta$ production threshold. The twelve Monte Carlo points are described with the correct relativistic Equations (3.13) and (3.15), $p_f = p_f(p_d, m_\eta, S)$ in black and $p_f^2 = p_f^2(p_d, m_\eta, S)$ in red, and the η mass is extracted. Assuming an uncertainty of 150 keV/c for the final state and beam momenta the mass can be determined with an precision below 25 keV/c^2. The error bars are too small to be shown on the figure.

It is important to mention that in first order the function $p_f^2 = p_f^2(p_d)$ depends linearly on p_d near threshold. Nevertheless, a linear fit to the data would result in a slightly shifted threshold momentum of about 50 keV/c, leading to an 11 keV/c^2 higher η mass value. By taking into account the quadratic term,

$$p_f^2 = p_f^2(p_d, a, b, c) = b\,(p_d - a) + c\,(p_d - a)^2 \;, \tag{3.23}$$

the fit results in the correct threshold momentum, represented by the fit parameter a. Due to the additional fit parameter the uncertainty of the threshold momentum as well as that of the η mass value increases nearly by a factor of two. Instead of using the linear approximation the measured data set was described by the relativistic correct Equations (3.15) and (3.13) to avoid such possible systematic errors.

In conclusion, Monte Carlo simulations clearly prove that the η mass can be determined at COSY-ANKE with a statistical uncertainty of below $25\,\mathrm{keV/c^2}$. This is competitive and comparable to results of recent experiments. However, finally it should be mentioned that in this estimation systematic errors of beam or final state momentum determination are not factored in.

3.2.3. Benefits of the threshold extrapolation approach

The previous section tried to explain why the COSY-ANKE method was the chosen approach for a new measurement. There are four important benefits:

1. Contrary to previous missing mass approaches [$\mathrm{P^+92}$, $\mathrm{AB^+05}$] the kinematic quantities are investigated for twelve different energies instead at a single one. This allows to study systematic effects in the spectrometer and beam momentum calibration.

2. In opposition to earlier missing mass experiments, in which only forward and backward scattered ^{3}He nuclei were detected, the ANKE spectrometer provides full geometrical acceptance for the reaction of interest close to threshold. This feature can be exploited to improve the spectrometer calibration, discussed in Chapter 6.

3. By using the resonant depolarisation technique the beam momenta were measured for the first time entirely independent of the spectrometer calibration in a missing mass experiment (see Chapter 5).

4. The most important benefit of the threshold determination method is that it does not require a perfectly absolute spectrometer calibration. This is illustrated in Figure 3.5.

Small imprecisions of the spectrometer's calibration parameters having effect on all twelve data points in a similar way. For example minor inaccuracies in the determination of the interaction vertex relative to the detection system can bring about a possible systematic energy dependence of the final state momentum and the missing mass. However, this effect disappears at reaction threshold. If it is not taken into account, such systematic errors would influence the threshold fit using

Equation (3.15), leading to a shift in the extracted η mass value. This effect must be taken into consideration and can be disentangled from the extracted η mass value by introducing an additional scaling factor S chosen as free fit parameter in the threshold extrapolation. Therefore, the right hand side of Equation (3.15) is multiplied by a scaling factor. It can be seen as additional calibration parameter, representing a further fine tuning of the spectrometer. In any case, it is crucial to note that its introduction does not affect the value obtained for the threshold momentum as well as the mass m_η.

An energy dependence of the final state momentum $p_f = \sqrt{p_x^2 + p_y^2 + p_z^2}$ can be provoked in Monte Carlo simulations by multiplying its individual components p_x, p_y and p_z using same or different scaling parameters. However, both cases, same or different scaling parameters, can be corrected by the threshold fit using $p_f = p_f(p_d, m_\eta, S)$.
Figure 3.5 illustrates as one example Monte Carlos simulations with a scaling of 20% of the transversal momentum component $p_\perp = \sqrt{p_x + p_y}$ in the laboratory system introducing a scaling in p_f. It is evident that a higher final state momentum (red crosses) implies a lower missing mass value, whereas a lower one (blue crosses) involves a higher value for the missing mass due to the mathematical definition. While the threshold extrapolation taking into account the scaling parameter $p_f = p_f(p_d, m_\eta, S)$ provides the correct threshold momentum as well as η mass value, the missing mass is not constant any more. Consequently, using the simple missing mass method for mass determination one would get a slightly different value at each of the twelve energies studied.

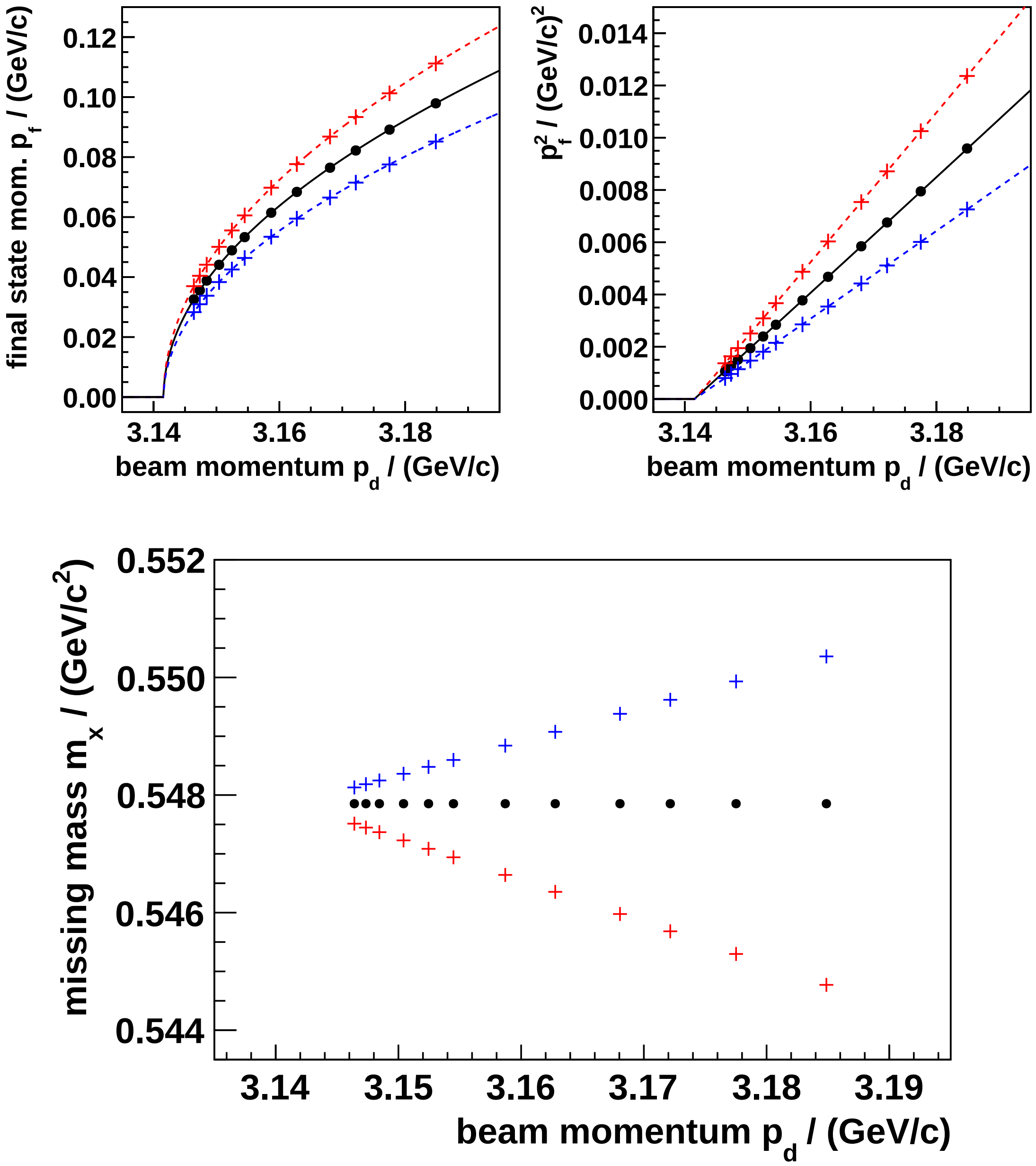

Figure 3.5.: The influence of a possible energy dependence on the measured ^{3}He momenta is shown for both, the threshold extrapolation (top) and the missing mass analysis (bottom). The scaling in p_f was introduced in Monte Carlo simulations by multiplying the transversal momentum component $p_\perp$ in the laboratory frame using an arbitrary constant $S = 0.8$ (blue crosses) and 1.2 (red crosses), respectively. While the threshold extrapolation provides the correct threshold momentum as well as m_η, the missing mass becomes energy dependent.

4. ANKE facility at COSY

Simulations, former and preparatory measurements demonstrated that the ANKE facility at COSY is very well suited for an η meson mass experiment. Such kind of a high precision measurements makes high demands on the experimental equipment used. On the one hand the beam momentum of the COSY accelerator has to be measured and controlled to highest accuracy. On the other hand, the reaction of interest has to be identified and the ^{3}He momenta have to be determined with ANKE.

This chapter is intended to provide an overview of the experimental devices used during the beam time. After having presented COSY in the first part, the devices for the beam momentum determination will be introduced: the EDDA detector and the radio frequency[1] solenoid. Afterwards, the ANKE setup will be discussed and finally the experimental conditions during the beam time will be summarised.

4.1. COSY - COoler SYnchrotron and its radio frequency cavity system

COSY, the COoler SYnchrotron of the Forschungszentrum Jülich, depicted in Figure 4.1, is an accelerator and storage ring for experiments in medium energy physics [Mai97]. The name is based on two cooling systems, the electron and stochastic cooling, installed in the ring to reduce the beam phase space. The main components of this facility are the ion sources, the injector isochronous cyclotron JULIC, the 100 m long injection beam line, and the cooler synchrotron, providing four internal experimental areas equipped with different detector setups ANKE, EDDA, WASA, and PAX. Furthermore, the beam can be extracted and used for the TOF experiment and two external areas serving for preparatory measurements of devices for the PANDA or CBM detector. In future these two detectors will be installed at the facility FAIR in Darmstadt.

[1] In the following radio frequency will be abbreviated with the acronym rf.

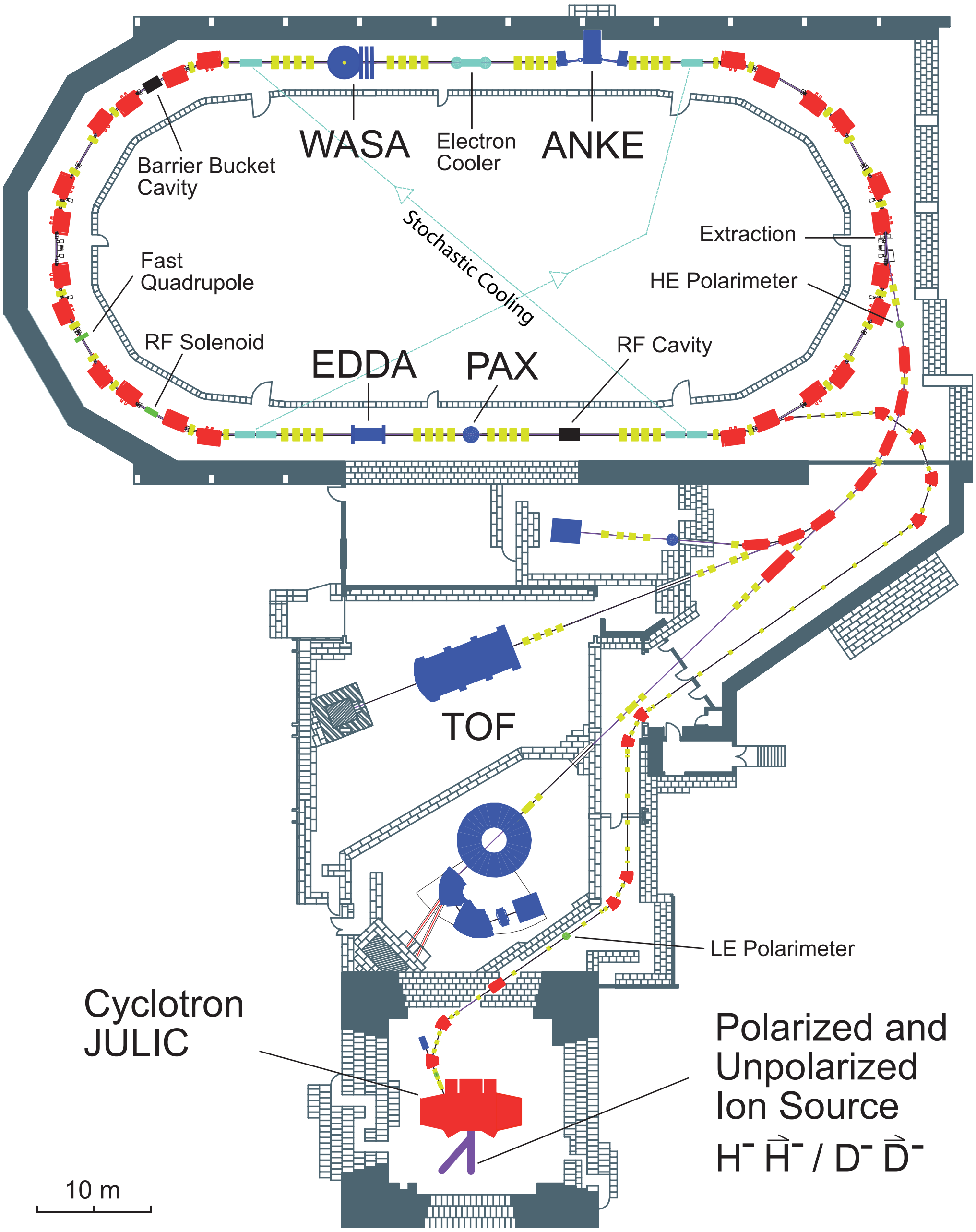

Figure 4.1.: The COSY accelerator facility. The cyclotron JULIC provides unpolarised or polarised proton and deuteron beams for injection into the COSY ring, where they are accelerated and stored. The position of the ANKE spectrometer with the internal cluster-jet target is shown, as are those of the radio frequency solenoid for depolarising the deuteron beam, the barrier bucket cavity for compensating beam-target energy losses, and the EDDA used as beam polarimeter.

The storage ring consists of 24 dipole magnets bending the beam onto two 52 m long arcs, as well as of 56 quadrupole magnets used for beam focussing. The internal target experiments are installed at the two straight sections, each of them 40 m long. So in total the ring has a circumference of 184 m. The different ion sources produce unpolarised as well as polarised negatively charged hydrogen or deuterium ions (H^-, D^-). This is done by hydrogen (or deuterium) scattering at caesium $H(D) + Cs \rightarrow H^-(D^-) + Cs^+$. The ions are injected in the cyclotron and pre-accelerated to an energy of 45 MeV for hydrogen and 90 MeV for deuterium, respectively. Afterwards, they are transferred into the storage ring via stripping injection by penetrating a charge exchanging carbon foil. The particles are accelerated with the rf cavity to the desired energy in the COSY momentum range from $0.3 - 3.7$ GeV/c, associated to revolution frequencies from $0.26 - 1.6$ MHz. COSY delivers proton or deuteron beams with up to 10^{11} unpolarised or 10^{10} polarised particles. The beam intensity for polarised beams is typically lower by one order of magnitude, due to the reduced ion current of the polarised source. The main features of the COSY accelerator can be found in Table 4.1.

Feature	Comment
Beams	p, d and $\vec{\mathrm{p}}$, $\vec{\mathrm{d}}$
Momentum range	$p_{\mathrm{beam}} = 0.3 - 3.7\,\mathrm{GeV/c}$
Cooling	electron cooling $p_{\mathrm{beam}} < 0.6\,\mathrm{GeV/c}$ stochastic cooling $p_{\mathrm{beam}} = 1.5 - 3.3\,\mathrm{GeV/c}$
Momentum spread	without cooling: $\partial p/p = 10^{-3}$ with cooling and cavity: $\partial p/p = 10^{-4}$
Number of particles stored	protons unpol.: 1.5×10^{11}, pol.: 1.0×10^{10} deuterons unpol.: 1.3×10^{11}, pol.: 6.0×10^{9}

Table 4.1.: Main features of the cooler synchrotron COSY.

The application of cooling systems and cavities allow to improve the beam quality, compensating the beam deterioration caused by intrabeam scattering and beam-target interaction. By that the beam momentum spread of typically $\partial p/p = 10^{-3}$ is reduced down to 10^{-4}, loosing a negligible amount of beam intensity only. The electron cooling system can be applied up to a momentum of 600 MeV/c and is complemented by a stochastic cooling, operating in the upper momentum range from $1.5 - 3.7$ GeV/c. In addition to the accelerating and decelerating rf cavity a broadband barrier bucket[2] cavity is installed at COSY since 2007 [S+08b]. Contrary to the rf cavity the signal of the bb cavity is generated by up to 20 harmonics. This allows to store a single board bunch filling $80 - 90\%$ of the ring comparable to a debunched beam [GAMM83]. The combination of bb cavity and stochastic cooling is well suited for compensating the intensity and mean energy losses provoked by the introduction of thick internal targets in the ring, e.g., the ANKE cluster-jet target or the WASA pellet target.

4.2. Equipment used for beam momentum measurement

During the beam time for the η mass measurement, the accelerator beam momenta were measured by the use of the so-called resonant depolarisation technique or spin resonance method[3]. It is based on the resonant depolarisation of a polarised beam with an artificial spin resonance induced by a horizontal radio frequency magnetic field of a solenoid. Therefore, the beam polarisation was measured with the EDDA detector (see Section 4.2.1) as function of the radio frequency of the longitudinal magnetic field produced by a solenoid (see Section 4.2.2).

The other important quantity necessary for the beam momentum determination is the revolution frequency of the circulating COSY beam. This one was measured by using the Schottky noise of the beam (see Section 5.2). The Schottky noise was recorded by means of the beam pickup and the standard "swept-type model HP 8595E" spectrum analyser of the stochastic cooling system of COSY.

4.2.1. EDDA detector as beam polarimeter

The internal target experiment EDDA [A+05][4] was designed to study proton-proton elastic scattering excitation functions in the COSY energy range. The detector is composed of two cylindrical detector shells made of scintillating material, which are mounted around the COSY beam pipe. Figure 4.2 illustrates a schematic drawing of the detector.

As result of the compact design EDDA covers almost 85% of the whole solid angle and 30° to 150° in ϑ_{CM} for elastic proton-proton scattering. The inner detector shell

[2] In the following barrier bucket will be abbreviated with the acronym bb.
[3] The underlaying physical principles and results of the spin-resonance method will be discussed in detail in Section 5.
[4] More detailed explanations are provided by the references therein.

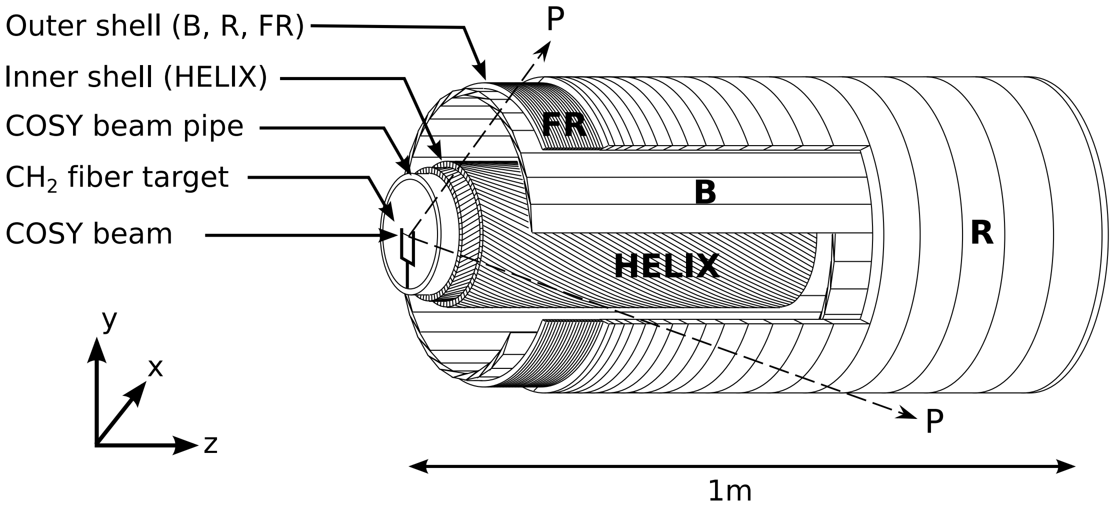

Figure 4.2.: Sketch of the EDDA detector, consisting of two cylindrical detector shells made of scintillating material, an inner shell HELIX and an outer shell (FR, B, R) [Sch99].

(HELIX) is made of four layers of scintillation fibres helically wound in opposite direction. The outer shell comprises scintillator bars (B) arranged parallel with the beam pipe, surrounded by semi-rings (R) and such once of scintillating fibres (FR). There are three different kinds of targets which can be used at EDDA: a polypropylene CH_2 fibre target, a pure carbon target, or a polarised hydrogen atomic gas beam target.

In the context of his PhD work V. Schwarz developed a technique for using the EDDA detector as fast internal beam polarimeter at COSY [Sch99]. This method was applied to determine the vector polarisation of the polarised deuteron beam during the spin-resonance measurements in the η mass beam time. In contrast to the case of a spin-half fermion such as an electron or proton, the deuteron is a spin-one boson. It can be placed in three magnetic substates $m = -1, 0, +1$ with respect to a quantisation axis. That is why the resulting polarisation phenomenology is more complex. Eight independent parameters are necessary to characterise a spin-one beam, three for the vector polarisation and five for the tensor [Ohl72]. However, the vector polarisation

$$P_V = (N_+ - N_-)/N \ , \tag{4.1}$$

was measured by EDDA solely, because this one can be determined to a higher precision than the tensor one. Here N_m is the number of particles in state m and $N = N_+ + N_- + N_0$ is the total amount of particles.

Due to the spin-orbit coupling, the scattering of a polarised beam at an unpolarised target generates an asymmetry ϵ in the azimuthal angle ϕ event distribution. The asymmetry is defined by the multiplication of the beam polarisation P with the corresponding analysing power A. For a perfectly vertically polarised beam with regard to the beam axis, i.e., in y direction, the following equation applies:

$$\epsilon = P_y \cdot A_y = \frac{N_R - N_L}{N_R + N_L} \,. \tag{4.2}$$

The asymmetry is manifested in the difference between the number of hits in the left N_L and right N_R hemisphere of the detector. It is determined by using the fast polarisation measurement method of EDDA. For obtaining absolute polarisation values, a calibration measurement of the EDDA detector at all twelve energies had to be required. However, for the beam momentum determination it is sufficient to consider a quantity merely proportional to the polarisation, e.g., the left-right asymmetry ϵ. By that one can omit a time- and money-consuming calibration measurement. That means that for all spin-resonance spectra in Section 5.3 relative polarisation is applied.

4.2.2. RF solenoid for inducing an artificial spin-resonance

Using the spin-resonance method for beam momentum determination an artificial spin-resonance is induced by a longitudinal rf magnetic field from a solenoid. It aims to affect the spin motion of the polarised beam particles stored in COSY. The rf solenoid, shown in Figure 4.3, is made of a single-layer water-cooled copper coil wound on semi-cylinder of Plexiglas. This one was installed around one of COSY's ceramic vacuum pipes in order to guarantee a good transmission of the longitudinal magnetic rf field on the accelerator beam. The solenoid generates magnetic fields within a frequency range of $0.5 - 1.5\,\mathrm{MHz}$. The integrated value of the maximum longitudinal rf magnetic field is $\int B_{\mathrm{rms}} dl = 0.67\,\mathrm{Tmm}$ at a rf voltage of $5.7\,\mathrm{kV}$ rms.

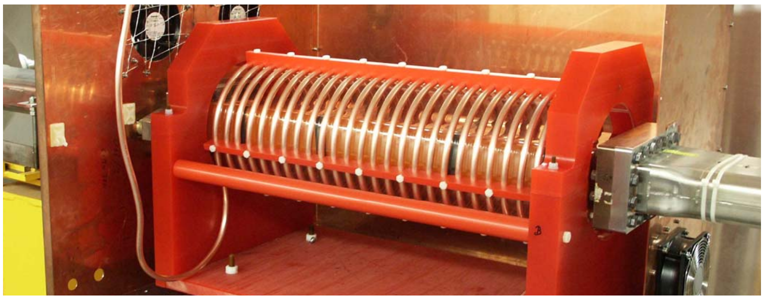

Figure 4.3.: The solenoid generates a longitudinal magnetic rf field to influence the spin dynamics of a polarised beam stored in COSY.

4.3. Magnetic spectrometer ANKE

The acronym ANKE stands for "**A**pparatus for Studies of **N**ucleon and **K**aon **E**jectiles" [B+01]. The detector is located at an internal target station of the storage ring, shown as a schematic drawing in Figure 4.4. The main components are three dipole magnets D1, D2, D3, internal target, and detection setup, composed of four elements: spectator detector, positive (Pd), negative (Nd) and forward (Fd) detection setup.

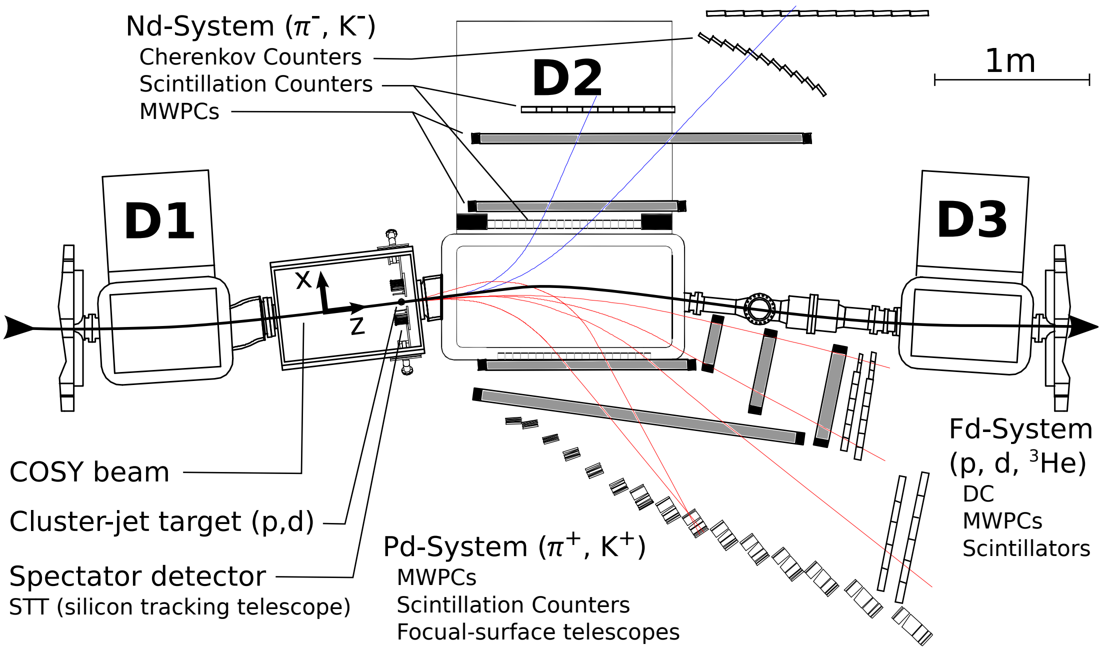

Figure 4.4.: Schematic drawing of the ANKE detector including its main components: three dipole magnets D1, D2, and D3, target, and four detection systems: spectator detector, positive (Pd), negative (Nd), and forward (Fd) detector. Negatively charged particle tracks are illustrated in blue and those with positive charge in red.

The Pd, Nd, and Fd system consist of various particle detectors like drift or multiwire proportional chambers, scintillation or cherenkov counters, and focal-surface telescopes. ANKE can be equipped with three different types of targets:

- an unpolarised strip target of carbon, polyethylene, or other solid materials,
- an unpolarised cluster-jet target of hydrogen, or deuterium,
- or a polarised storage-cell hydrogen gas target.

The cluster-jet target makes it possible to achieve luminosities of $10^{30}-10^{31}\,\mathrm{s}^{-1}\mathrm{cm}^{-2}$, corresponding to areal target densities of $10^{14}-10^{15}$ atoms/cm^{-2}. Double polarised experiments can be performed when using the polarised gas target reaching luminosities of $10^{28}-10^{29}\,\mathrm{s}^{-1}\mathrm{cm}^{-2}$.

The detector setup was designed for investigating reactions close to threshold at low excess energies. Therefore, at a fixed target experiment, it is of prime importance to detect the particles produced under small angles. They would normally escape in the beam pipe, because of their small transversal momenta and their large Lorentz boost. At ANKE this is realised by deflecting the COSY beam by using the three dipole magnets D1, D2, D3 through a chicane in the ring.
First D1 deflects the circulating beam by an angle α off its straight path onto the target; the spectrometer dipole magnet D2 separates the produced particles from the beam for momentum analysis; finally D3 leads the unscattered beam particles back onto the nominal orbit.
The spectrometer dipole magnet D2 having a gap of 200 mm separates the produced particles in terms of their rigidity, that means ratio of their momentum and charge. Negatively charged particles like π^- or K^- are deflected onto the negative detector placed on the left hand side of the beam; on the contrary, positively charged ones with low momenta onto the positive detector. Due to their high rigidity, positively charged particles with high longitudinal momenta in the LS frame as protons, deuterons, or ^{3}He nuclei are deflected only slightly by the D2 magnet. Consequently, they move on trajectories very close to the beam pipe and are detected by the forward detector system.
The design requires the D2 magnet and components of Pd, Nd, and Fd system to be placed in common on a platform movable in horizontal direction perpendicular to the beam. The deflection angle of the beam α, depends on the position of the platform. Angle ($0° \leq \alpha \leq 10.6°$), magnetic field strength of D2 ($\leq 1.57\,\mathrm{T}$), and beam momentum cannot be chosen independently of each other. By adjusting these three parameters it is possible to increase the geometrical acceptance for the reaction of interest.

The tracks of charged particles detected by the various ANKE detection systems can be traced back to the interaction point through the precisely known magnetic field. This leads to a momentum reconstruction for registered particles. In addition to the three parameters mentioned, i.e., magnetic field, deflection angle, and interaction point, the positions of the tracking detectors, the drift and wire chambers, have to be determined with high accuracy, too. This requires a precise calibration of the detection system. For the Fd system alignment and calibration the kinematics of a two-body reaction were used. This will be presented in Chapter 6.

In the next section the components of ANKE needed for the investigation of the reaction $\mathrm{d\,p} \to {}^3\mathrm{He}\,\eta$ will be presented in detail.

4.3.1. Münster type cluster-jet target

The cluster-jet target, built up in Münster [D+97, K+99], has become the most often used target for the ANKE experiment because it fulfils the particularly contrary demands of an internal target.
On the one hand, accelerator physicists prefer a very thin and closely localised bunch of matter as target. So the beam deterioration originated primarily by beam-target interaction can be compensated with coolings, cavities, and optics of the accelerator. On the other hand, physicists who study nuclear reactions and rare processes want high density targets to achieve high luminosities and high event rates.
From this point of view a windowless cluster-jet target is the optimal choice for an unpolarised internal target experiment, because solid state targets provide too high densities (10^{22} atoms/cm^2) and gas-jet targets too low ones (10^{12} atoms/cm^2).

Figure 4.5 depicts a schematic drawing of the cluster-jet target designed at the Westfälische Wilhelms-Universität Münster which is installed at the ANKE experiment at COSY. It is composed of three main components: cluster-jet source, scattering chamber, and cluster-jet beam dump. The target provides hydrogen as well as deuterium cluster-jets, produced when gas passes a so called Laval nozzle under high pressure and at low temperatures. The expansion of the pre-cooled gas in the nozzle leads to a further cooling due to the Joule-Thompson effect for real gases, that results in a condensation of the atoms forming a narrow supersonic beam of clusters.

The production process of clusters in a Laval nozzle is shown in Figure 4.6 and illustrated by the reduction of relative momenta of atoms building up clusters via three body collisions. The produced clusters comprise $10^3 - 10^6$ atoms depending on the experimental conditions. Size and velocity of the clusters as well as the density of the cluster-jet beam depend strongly on the shape of the trumpet part and the diameter of the Laval nozzle. In addition to that, there is a powerful dependence on pressure and temperature of the gas before entering the nozzle. The range from $10 - 100\,\mu$m represents typical values for the nozzle diameter; $1 - 20$ bar can be used for the gas pressure; and $20 - 50$ K for temperature. These operation parameters allows to adjust the target areal density in a range of $10^{12} - 10^{15}$ atoms/cm^2 in a distance of ≈ 0.5 m behind the nozzle.

Till today the cluster production process in a Laval nozzle still hides many secrets and is not entirely understood yet. Systematic measurements of the target areal density as function of pressure and temperature show a structure in the previously adopted homogenous cluster-jet beam [Köh10], depicted on the photography of the right hand side of Figure 4.6. This occurs when the target is driven at low temperatures and high pressures (> 10 bar), so that the hydrogen is in fluid phase.

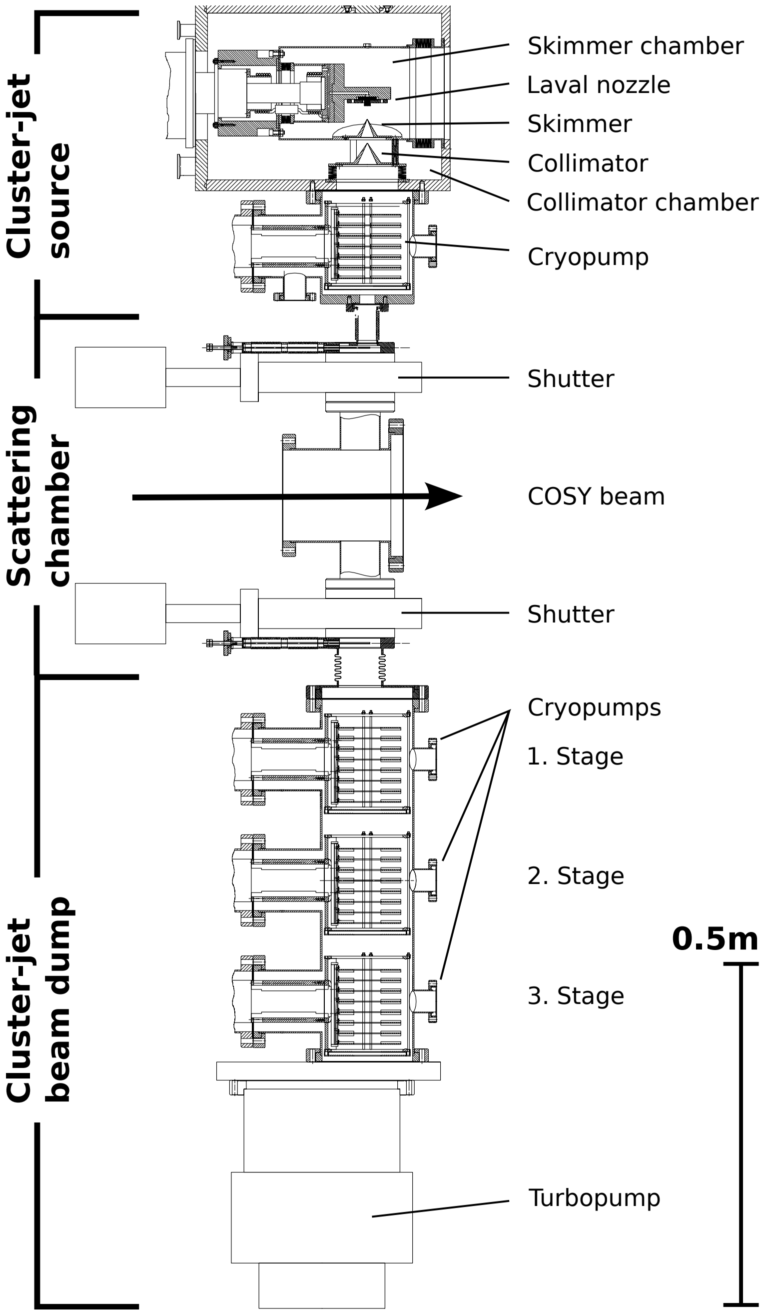

Figure 4.5.: The cluster-jet target installed at ANKE consists of three main parts: the cluster-jet source, the scattering chamber and the cluster-jet beam dump.

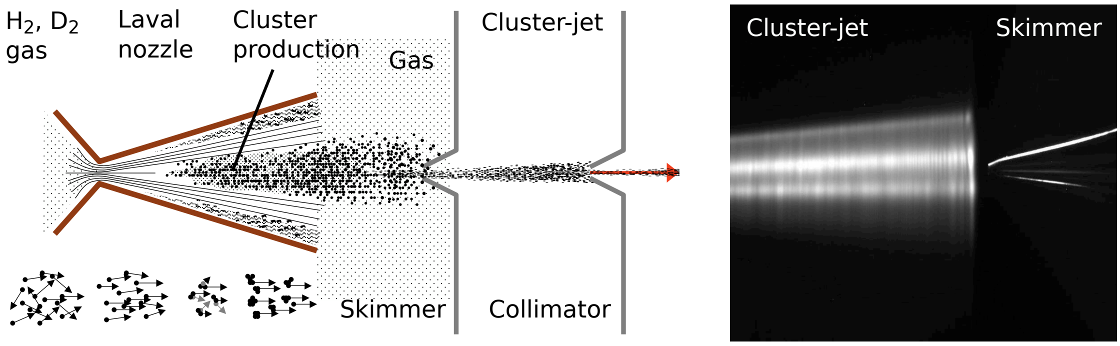

Figure 4.6.: Left: The cluster production process in a Laval nozzle and the extraction and shaping of the cluster-jet beam using a skimmer and collimator. Right: Photograph of the cluster-jet beam impinging on the skimmer [Köh13].

In contrast to other cluster-jet targets this is a special feature of the Münster-type one. By extraction the brightest part of the cluster-jet, the target density can be increased by at least one order of magnitude. Although the target areal density decreases with the distance squared from the source, it allows to provide a high dense target with areal densities of 10^{15} atoms/cm^2 even at larger distances. This is necessary for the future PANDA experiment at the FAIR facility in Darmstadt. Due to the detector geometry the PANDA target has to provide an areal density of 4×10^{15} atoms/cm^2 at a distance of 2.1 m. This aim will be achievable with the new cluster-jet target [oC12, T$^+$11, Täs12, Köh13], already designed and build up in near future in Münster.

When producing clusters only a very small part of gas condensates to the cluster-jet beam, which is separated from the enormous residual gas load by an conical orifice, the so-called skimmer with a diameter of 0.7 mm, installed closely behind the nozzle. A second orifice, the collimator, defines the shape of the cluster-jet beam in the scattering chamber (see Figure 4.5 and 4.6). During the transition of the cluster-jet beam into the COSY ring vacuum the residual gas has to be retained effectively because the pressure in the scattering chamber may not exceed a value of $10^{-6} - 10^{-7}$ mbar. By using a combination of roots and rotary vane pumps the pressure in the skimmer chamber can be reduced to 10^{-1} mbar. The collimator chamber is subdivided into two pumping stages, the first one with a turbo molecular pump decreasing the pressure up to 10^{-4} mbar and the second one with a self-constructed cryopump in order to bring the pressure into line with the vacuum conditions of the synchrotron ring.

The part of the cluster-jet beam, which does not interact with the COSY beam, is collected in the beam dump. It consists of three stages equipped with three self-constructed cryopumps and one turbo molecular pump mounted at the end.

The vast majority of the cluster-jet beam is removed by the turbo molecular pump. The residual gas load generated by the evaporation and blow out of the cluster-jet beam is retained by differential pumping with cryopumps. By that the pressure level is adapted to that of the ring.

4.3.2. Forward detection system

Although ANKE is equipped with a variety of detectors, it is only the Fd system that was used for the η mass measurement detecting the ^{3}He nuclei from the reaction $\mathrm{d\,p} \to {}^3\mathrm{He}\,\eta$. Nevertheless, the Pd and Nd systems[5] were also switched on for the investigation of the ABC-effect appearing in the two-pion production reaction $d\,p \to {}^3\mathrm{He}\,\pi^+\,\pi^-$ [ABC60, Mie13].

The ANKE Fd system is placed between the D2 and D3 magnet (see Figure 4.4), designed for identification of heavy particles as protons, deuterons, and helium nuclei with high momenta scattered in forward direction. It consists of a multiwire drift chamber, two multiwire proportional chambers (MWPC) and two layers of scintillation hodoscopes, shown in Figure 4.7. Optionally, the Fd system can be extended by Cherenkov radiation counters for proton-deuteron separation, or by an additional layer of plastic scintillators, typically the Pd sidewall. During the η mass beam time this device was used for additional energy loss measurements. The acceptance of the Fd system is limited by the 0.5 mm thin forward exit window with dimensions of $240\,\mathrm{mm} \times 224\,\mathrm{mm}$ made of aluminium. Using ANKEGeant4[6] Monte Carlo simulation of the $\mathrm{d\,p} \to {}^3\mathrm{He}\,\eta$ reaction the position of the Fd system was optimised. Figure 4.7 depicts such an ANKEGeant4 simulation for the reaction $\mathrm{d\,p} \to {}^3\mathrm{He}\,\eta$ at an excess energy of $\approx 10\,\mathrm{MeV}$. The blue tracks symbolise the ^{3}He nuclei impinging on the Fd system.

Drift and multiwire proportional chambers for tracking

Track and momentum reconstruction in the Fd system are realised by the use of one drift and two multiwire proportional chambers [PZ02, D$^+$04]. Because of their position very close to the beam pipe they have to handle high counting rates ($> 10^7\,\mathrm{s}^{-1}$).
The drift chamber is installed shortly behind the forward exit window, consisting of two modules, each with four sensitive wire planes forming drift cells with an

[5] This detector components are described in detail in [B$^+$01] and references therein.
[6] AnkeGeant4 is a software package for simulating particle reactions at the ANKE facility. It is based on Geant4 a toolkit for modelling the passage of particles through matter. More informations at `http://geant4.cern.ch` . In this framework "Pluto" was used as event generator (see `http://www-hades.gsi.de/?q=pluto`).

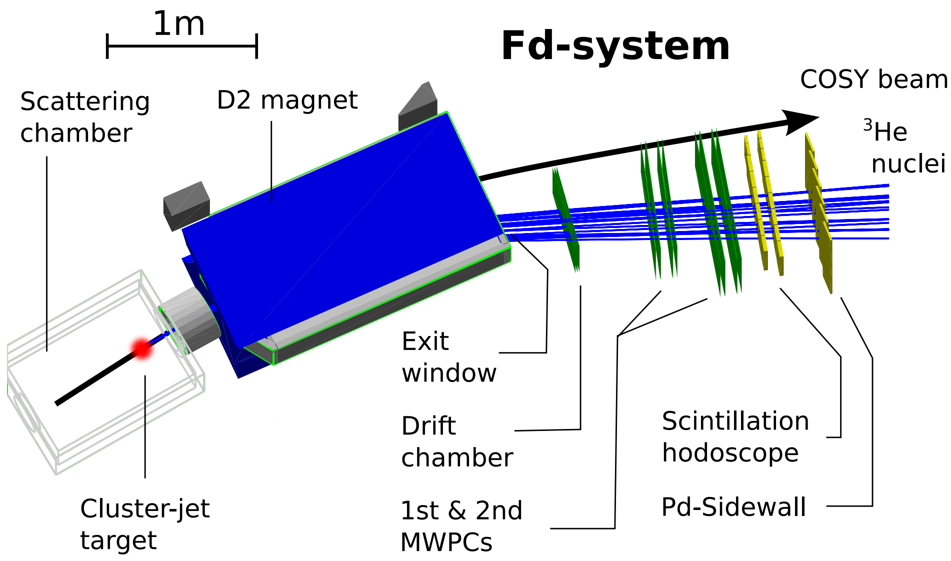

Figure 4.7.: The ANKE setup used for the determination of the η mass is presented by an ANKEGeant4 Monte Carlo simulation of the $\mathrm{d\,p} \to {}^3\mathrm{He}\,\eta$ reaction at an excess energy of $\approx 10\,\mathrm{MeV}$. The COSY deuteron beam (black arrow) hits the hydrogen cluster-jet target (red point) and the helium nuclei produced (blue lines) at small angles are separated by the D2 spectrometer magnet to be detected by the ANKE Fd system, consisting of one drift chamber, two multiwire proportional chambers (green), and the scintillation hodoscope (yellow).

area of $10\,\mathrm{mm} \times 10\,\mathrm{mm}$ [S$^+$08a]. Each module comprises two planes with vertically installed wires and two ones with wires rotated by $30°$, which allow to determine the hit positions in the xz-plane. The main purpose of this chamber is to increase the momentum resolution of the z-component. That one dominates the momentum in the LS frame at a fixed target experiment. The hit positions can be determined with an accuracy of $200\,\mu\mathrm{m}$ by using the drift times reconstructed.
Two MWPCs, technically identical except for their size, are installed behind the drift chamber. Each one is composed of one module with vertical wires in order to determine the x hit position, the other one with horizontal wires for the y position. The x and y modules contain two wire and one strip plane. The latter one is used as active cathode inclined by $18°$ with respect to the wire orientation. Every time a particle passes the wire chambers, the average number of wires fired in a plane is close to unity making a high spatial resolution of $1\,\mathrm{mm}$ possible.
The combination of drift and multiwire proportional chambers with its good spatial resolution provide a momentum resolution of $\approx 1\,\%\,(\sigma)$ for protons. Table 4.2 summarises the properties of the Fd multiwire chambers.

Feature	Drift chamber	MWPC1 and MWPC2
Gas filling	80% Ar + 20% C_2H_6	85% CF_4 + 15% C_2H_6
Number of x-planes	8	2
Number of y-planes	–	2
Wire spacing / mm	5	1
Dimensons / mm	330 × 320	428 × 458 and 548 × 535

Table 4.2.: Properties of Fd system chambers.

Scintillation hodoscope for energy loss and time of flight measurement

The Fd system scintillation hodoscope [C$^+$02] provides energy loss and time of flight measurement as well as trigger signals. It consists of two layers with 8 and 9 vertically orientated plastic scintillation counters, respectively. The layers are shifted with respect to each other by the half counter width to avoid gaps in-between. The scintillation light is read out via photomultipliers mounted on both ends of the counters providing the timing and amplitude signal. The dimensions for most of the counters are 360 mm × 80 mm × 20 mm (H×W×D), except for two counters of the first layer and three ones of the second one close to the beam pipe. The thickness is reduced to 15 mm, while the width decreases gradually to 40 mm, because of the higher count rates in this region. In the η mass beam time one scintillation layer of the Pd sidewall was placed behind the Fd hodoscope and used for an additional energy loss measurement. This allows a much more effective ^{3}He online trigger in order to reduce the dead time (see Section 4.3.3). The Pd sidewall layer is made of six equal scintillators with dimensions of 1000 mm × 100 mm × 10 mm.

4.3.3. Trigger used during the η mass beam time

The data acquisition system[7] at ANKE was designed for handling event rates of 10^3 Hz to 10^4 Hz. But for total trigger rates of $\geq 10^4$ Hz, approximately only 50% of the events are written on tape due to the increasing dead time [B$^+$01]. Since the Fd system is typically exposed to much higher event rates on the scale of $> 10^6$ Hz, it was conclusively necessary to select just the events of interest, reducing the dead time by an online trigger. The trigger system developed for ANKE permits to set up four independent hardware triggers. Two of them, T1 and T2, were used during the η mass beam time.

[7] In the following data acquisition system will abbreviated with the acronym DAQ

The amount of particles hitting the Fd system, is mainly dominated by protons and deuterons. It is because the cross sections for reactions where these particles are produced exceed those for helium production by far. The application of a dedicated energy loss trigger T1 suited for helium identification provides a satisfactory background suppression, i.e., proton and deuteron suppression.
For the first time this trigger was set up for studying the $^4\mathrm{He}\,\eta$ final state via the reaction $d\,d \to\ ^4\mathrm{He}\,\eta$ [W$^+$05]. Afterwards it was successfully applied during the beam time conducted for the investigation of the $^3\mathrm{He}\,\eta$ final state [Mer07, Pap13]. The online trigger uses signals of the plastic scintillation counters of the Fd hodoscope, which are directly proportional to the energy loss of the passing particles. The scintillation counters are read out from both sides. This requires special integrating modules providing summation and integration of two analogous signals. According to the Bethe formula, which describes the energy loss of charged particles moving through matter, the doubly charged helium nucleus gives rise to a larger energy loss than single charged proton or deuteron. The discrimination threshold for each counter was adjusted below the ΔE-p band of the ^{3}He nuclei. The helium trigger T1 required such high energy losses in coincidence in the first and second layer of the Fd hodoscope ($L1, L2$). In addition to that the Pd sidewall layer ($L3$) was incorporated into the trigger. To avoid gaps between its scintillator bars, they were mounted overlapping at their ends (see Figure 4.7). Finally the helium trigger T1 reduced the dead time to about 30% requiring high energy loss in each scintillation layer coincidently:

$$T1 = (L1 \wedge L2 \wedge L3) \ \text{ with High-Threshold} \ .$$

The second trigger T2 was set up to record events in the forward hodoscope for calibration and normalisation purposes. It focuses on reactions with protons and deuterons in the final state. The d p elastic scattering should be mentioned as one example. It serves for improving the chamber alignment as well as for determining the luminosity. The trigger T2 required a coincident signal of both, the first and the second layer of the Fd hodoscope at a lower threshold:

$$T2 = (L1 \wedge L2) \ \text{ with Low-Threshold} \ .$$

Because of the enormous cross section for processes where protons and deuterons are produced, the second trigger was imposed with a prescaling factor of 1024 in order to reduce the total trigger rate increasing the DAQ efficiency. As a result the trigger T2 contributed to the total trigger rate by only 10%.

At every beam time the Trigger T4 is used for reading out the scaler information with a 10 Hz rate. The scalar serves for online monitoring the experiment. By that the DAQ records COSY beam intensity, count rates of specific detectors components, and trigger rates.

4.4. Experimental conditions at the beam time

Such a high precision η mass measurement like at COSY-ANKE needs special experimental techniques, while taking data at the beam time. One of these methods is the compensation for the accelerator beam energy loss by the bb cavity. Another one is the possibility to drive the COSY accelerator in the so-called supercycle mode. The supercycle is a special cycle setting comprising up to seven different energies. The twelve accelerator beam energies presented in Table 3.2 were subdivided into two supercycles for the experiment. The measurement of the (p_d, p_f) data set followed the subsequent schema:

1$^{\text{st}}$ beam momentum measurement:
: Before starting the DAQ for recording data of the reaction $\mathrm{d\,p} \to {}^3\mathrm{He}\,\eta$ with ANKE using the COSY supercycle mode, each of the six beam momenta of one supercycle was measured by using the resonant depolarisation method. The measurement of one energy setting took $3-4$ hours roughly, so that in total nearly a whole day was needed when determining the six different energies of one supercycle.

Data taking of the reaction $\mathrm{d\,p} \to {}^3\mathrm{He}\,\eta$ with ANKE:
: After the first beam momentum measurement the six different energies were implemented in the supercycle. Then the ion source was switched from the polarised to the unpolarised one. Over a period of five days approximately COSY was running in the supercycle mode, while data being collected with ANKE.

2$^{\text{nd}}$ beam momentum measurement:
: After five days of data taking with ANKE the ion source was switched again from unpolarised to polarised. That was necessary for measuring the COSY beam momenta a second time in order to study systematic effects.

4.4.1. Energy loss compensations by barrier bucket cavity

For the high precision η mass experiment it was essential that the beam momentum remained stable throughout the whole accelerator cycle. In a typical cycle of a standard scattering experiment at ANKE, the beam is first injected into COSY and accelerated to the nominal momentum. The rf cavity is then switched off in order to provide a coasting beam filling the ring uniformly. This implies constant count rates, which minimise the dead time of the DAQ.
However, the momentum as well as the revolution frequency change, because of the energy losses through electromagnetic processes when the beam passes repeatedly through the target [S$^+$08c]. The revolution frequency would change by up to 103 Hz

over a 180 s long cycle when using a deuteron beam and a hydrogen cluster-jet target with a density of $\rho = 1 \times 10^{15}$ atoms/cm^2. This corresponds to a shift in beam momentum of 2.2 MeV/c over the whole cycle.
In order to compensate for this effect and to guarantee a constant beam momentum over the whole cycle, a second cavity, the bb cavity [S$^+$08b], was activated after having switched off the rf cavity. By this way a bunched beam was produced filling about 80% to 90% of the ring homogeneously leading to a reduction in the dead time of the DAQ. As mentioned in Section 4.1, the COSY beam energy loss, originated through the beam-target interaction, is compensated most effectively through the combination of bb cavity and stochastic cooling. However, the stochastic cooling was not used at the η mass beam time, because the COSY accelerator was driven in a so-called supercycle mode, the best way to measure a large number of energies.

4.4.2. The supercycle mode and its cycle timing

The twelve closely spaced energies studied near the η threshold (see Table 3.2) were divided alternately into two supercycles that can comprise up to seven different COSY machine settings. Each supercycle covered an excess energy range from $1 - 10$ MeV. In addition to six different energies above threshold one more energy was implemented into both supercycles below η threshold at $Q \approx -5$ MeV or $p_d = 3120$ MeV/c. It was implemented twice to collect sufficient data for a smooth background description (see Section 6.2.4). So the first and the second supercycle consist of seven different energies summing up to thirteen different momenta. The exact cycle timing of the two supercycles is presented in Figure 4.8. The different machine settings in the supercycles were imposed sequentially, after which the supercycle was repeated. Each supercycle was used for five days of data taking to collect sufficient statistics of the reaction $\mathrm{d\,p} \to {}^3\mathrm{He}\,\eta$ for a reliable final state momentum determination. In parallel Schottky data were recorded continuously to study the long term stability of the revolution frequency in COSY.

The reason for choosing supercycles instead of independent measurements at fixed energies was to guarantee the same experimental conditions for each of the beam energies in one supercycle. In this way the systematic uncertainties could be investigated in more detail, as will be discussed in Section 5.3.3 for the beam momentum and in Section 7 for the threshold extrapolation.

Before starting each one of the five day blocks, the individual beam momenta were measured using the spin resonance method. Therefore the spin-resonance spectrum for each energy was recorded by measuring the beam polarisation with EDDA as function of the frequency of the induced rf magnetic field from the solenoid. The timing structure of the 36 s accelerator cycle is described in Table 4.3. After the injection of the beam into COSY, the stored deuterons were accelerated by the

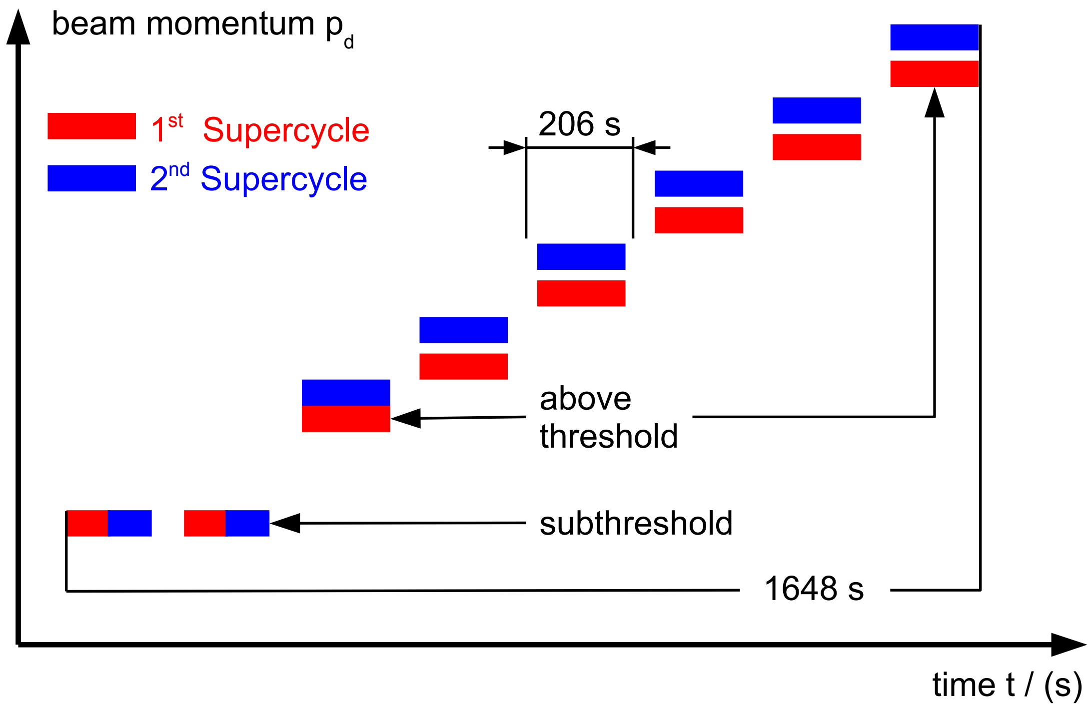

Figure 4.8.: Cycle timing of the supercycle. A cycle length of 206 s for one energy implies a total time for the supercycle of 1648 s or 27 minutes and 28 seconds, respectively.

regular COSY rf cavity to the first nominal beam energy of the supercycle. At $t = 3.7\,$s this cavity was switched off and at $t = 4\,$s the bb cavity was brought into operation to compensate for the beam energy losses. At $t = 20\,$s the amplitude of the depolarising rf solenoid was linearly ramped from 0 to 2.4 kV rms to produce a $\int B_{\rm rms} dl = 0.29\,$Tmm in 200 ms, remained constant for 5 s, and was then ramped down again in 200 ms. A five second long beam polarisation measurement followed using the EDDA detector [A$^+$05]. At $t = 36\,$s, the cycle was terminated. This procedure was repeated at the same beam energy but at different rf solenoid frequencies in order to obtain the complete spin-resonance spectrum. After having completed this first sub-measurement, the next beam energy of the supercycle was used and the corresponding spin-resonance spectrum measured until complete data was obtained at all the energies of the supercycle.

After having measured the spin-resonance spectrum, the supercycle was switched on for five days of data taking with ANKE to investigate the reaction $d\,p \to {}^3\mathrm{He}\,\eta$. In addition to that the revolution frequency was monitored continuously by the measurement of the Schottky noise to study long term stability of the COSY accelerator. During this data taking time the polarisation measurements were omitted and total cycle lengths of 206 s were used. Table 4.4 summarises the cycle timing. After the three steps of injection, acceleration and starting the bb cavity, the data taking with ANKE and the Schottky measurements were performed over a time interval of $t = 14 - 196$ s. The seven beam energies, with one doubled, so that their are really eight settings in one supercycle involved a total time of 1648 s. After that time the complete supercycle was repeated for five days of data taking. Then the system was reset to the first conditions shown in Table 4.3 in order to repeat the measurement of the spin-resonance spectrum to control systematic effects.

At the η mass beam time the polarised ion source delivered a beam intensity that was about one order of magnitude too low compared to that one required in the proposal. Therefore, it was decided to use this ion source exclusively for the beam energy measurement before and after the data taking with supercycles. As a consequenc COSY was switched to the unpolarised ion source for data taking, which allowed beam intensities up to $n_d \approx 1 \times 10^{10}$. It was very important to check carefully that the same COSY beam energies were obtained when using the polarised and the unpolarised ion sources. To ensure this, the complete settings of the cyclotron, the beam injection, as well as COSY itself, were fixed when switching from one ion source to the other one. The validity of switching the ion sources was proven (see Section 5.2.4) by monitoring the revolution frequency of the stored beam for the two different cases.

The high beam intensity of the unpolarised source made it possible to implement a third supercycle with additional energy settings for the last two days of the beam time [Gos08]. The main objective of the third supercycle was to collect data at a supplementary energy below threshold for verification and improvement of the background description. Besides that, also data at further energies above threshold, e.g., $Q \approx 15$ MeV, could be recorded. The lack of time allowed only one beam momentum measurement for each energy. Consequently it could not be considered for the η mass determination. However, it is intended to use the data for the determination of total and differential cross sections [Fri13].

Time t / (s)	Process
0	Start of cycle: injection
0 – 3.7	Acceleration of the beam with rf cavity
3.7	Switch off rf cavity
4	Switch on bb cavity
20 – 25	rf solenoid on
25 – 30	Polarisation measurement with EDDA
30	Schottky measurement
36	End of cycle

Table 4.3.: Cycle timing used to determine the spin-resonance frequency spectrum with the polarised beam.

Time t / (s)	Process
0	Start of cycle: injection
0 – 3.7	Acceleration of the beam with rf cavity
3.7	Switch off rf cavity
4	Switch on bb cavity
14 – 196	Data taking with ANKE
30 – 180	Schottky measurements every 30 s
206	End of cycle

Table 4.4.: Cycle timing used during data taking with ANKE with the unpolarised beam.

5. Beam momentum determination

Most of the analysis of the COSY beam momentum determination using the resonant depolarisation technique is already presented in a Diploma thesis [Gos08]. However, the analysis was finalised in context of this PhD thesis. The challenging demands of the high precision mass measurement required a lot of effort in order to extract the final beam momenta with highest accuracy. Afterwards the final results were published in the journal "Physical Review Special Topics - Accelerators and Beams" in 2010 [G$^+$10]. This following chapter will present the method in more detail and the main results will be summarised. One can find more specific aspects in the two publications mentioned above.

In general, the momentum of a beam stored in a ring like COSY is given by the velocity v of the beam particles. This quantity is determined typically by measuring the revolution frequency f_0 of the beam particles and their absolute orbit length s:

$$v = s \cdot f_0 \ . \tag{5.1}$$

The measurement of the orbit length by, e.g., beam position monitors, limits the achievable accuracy of this approach of typically $\Delta p/p \approx 10^{-3}$. It is nearly impossible to obtain the necessary increase in accuracy to $\Delta p/p \approx 10^{-4}$ needed for the η mass measurement by simply scaling up the number of beam pickup electrodes because of technical restriction of such a macroscopic device. Therefore, the beam momentum must be determined in some other way. A complete different approach to overcome this limitation for a high precision beam momentum determination is provided by the resonant depolarisation method focussing on spin dynamics of polarised beams.

The physical principles of this method will be explained in Section 5.1; the determination of the two important measuring variables, i.e., the revolution frequency f_0 and the spin resonance frequency f_r, will be discussed in Sections 5.2 and 5.3. At the end, Section 5.4 summarises the final outcomes.

5.1. Physical principles of the resonant depolarisation technique

The resonant depolarisation technique also named spin resonance method [S+76, D+80] was developed at the electron-positron collider VEPP of the BINP "Budker Institute of Nuclear Physics" at Novosibirsk in the end of the 1970s. It was applied very successfully for mass measurements of a wide variety of mesons from the ϕ [B+87] over the J/ψ [A+03] to the Υ [A+82][1] at the VEPP accelerator. The application was further developed at DORIS in Hamburg [B+84] and CESR in Cornell [M+84], as well as LEP at CERN [A+92]. Although, it was developed and applied to polarised electron or positron beams, there is in principle no reason why the resonant depolarisation approach should not be equally applicable to other beam particles with an intrinsic spin, such as protons or deuterons. Recently the effect was confirmed at the hadron machine COSY in studies of the spin manipulation of both polarised proton [L+04, M+04] and deuteron [M+05] beams. The resonant depolarisation technique is based on the spin dynamics of particles stored in polarised beams in a circular accelerator. The particle spin motion in an accelerator is described by the Thomas-BMT equation.

5.1.1. Spin in synchrotron: Thomas-BMT equation

The spin motion of a particle stored in a synchrotron is defined by the interaction between its magnetic moment and the magnetic structure of the ring. Every particle with an intrinsic spin $\vec{S}$ generates a "spin" magnetic moment $\vec{\mu}$:

$$\vec{\mu} = g\frac{q}{2m}\vec{S}. \tag{5.2}$$

The constant of proportionality includes the particle's charge q, mass m, and the gyromagnetic factor g. The Dirac equation, which is defined for point-like particles with half integer spin like the electron, predicts exactly a value of two for the g-factor. However, a value slightly larger was found experimentally. This is explained by QED through the interaction of the electron with virtual photons[2]. The deviation from the exact value of two is described by the anomalous magnetic moment or gyromagnetic anomaly G defined as:

$$G = \frac{g-2}{2}\ . \tag{5.3}$$

[1] In addition the masses of neutral and charged kaons have been measured. More detailed information can be found in the literature referenced therein.

[2] The electron g-factor is one of the most precisely measured quantity in physics confirming the predictions of QED.

For different composite particles, like proton and neutron, the g-factor and so the gyromagnetic anomaly varies in a wide range due to their inner structure of various elementary particles. The gyromagnetic anomaly for deuterons is,

$$G_d = -0.142\,987\,272\,5 \pm 0.000\,000\,007\,3 \ , \tag{5.4}$$

and can be calculated from the ratios of the magnetic moments and masses of proton and deuteron (see [Gos08] page 103 or [G$^+$10] reference [19]).

The interaction between a magnetic moment and an external magnetic field $\vec{B}$ results in a torque $\vec{\tau}$, aligning the spin vector (to the magnetic field vector):

$$\vec{\tau} = \frac{d\vec{S}}{dt} = \vec{\mu} \times \vec{B} \ . \tag{5.5}$$

The equation of motion of the spin vector is given by

$$\frac{d\vec{S}}{dt} = g\frac{e}{2m}\vec{S} \times \vec{B} \ . \tag{5.6}$$

when inserting Equation (5.2) with elementary charge e into Equation (5.5). This equation defines the spin motion in the rest frame of the particle in the presence of a magnetic field. In order to describe the spin motion of a particle in a synchrotron the well-known magnetic field structure of the accelerator in the laboratory system has to be transformed into the rest frame of the particle, which results in the Thomas-Bargmann-Michel-Telegdi equation[3] [Tho27, BMT59]:

$$\frac{d\vec{S}}{dt} = \frac{e}{\gamma m}\vec{S} \times \left[(1+\gamma G)\,\vec{B}_\perp + (1+G)\,\vec{B}_\parallel + \left(G\gamma + \frac{\gamma}{\gamma+1} \right) \frac{\vec{E} \times \vec{\beta}}{c} \right] \ . \tag{5.7}$$

$\vec{E}$ is the electric field, $\vec{B}_\perp$ and $\vec{B}_\parallel$ are the transverse and longitudinal components of the magnetic field of the accelerator in the laboratory frame with respect to the particle's direction of movement, which is represented by the particle's velocity vector $\vec{\beta}c$, in terms of which $\gamma = 1/\sqrt{1-\beta^2}$.

The last two terms are negligible in first approximation in an ideal synchrotron, in which the beam particles circulate exclusively on the nominal or closed orbit. Moving on the nominal orbit the particles are affected only by the vertical beam bending dipole magnetic fields, which are perpendicular to the particles' motion $\vec{B}_\perp$, whereas all other magnetic multipoles of higher order with $\vec{B}_\parallel$ generated by quadruple or sextuple magnets vanish. The cross product $\vec{E} \times \vec{\beta}$ is also equal zero because the electric field of the rf cavity in an accelerator is always parallel to the

[3] Abbreviated in following as Thomas-BMT equation.

moving direction of the beam particles. Consequently, the spin motion depends solely on the first term of the Thomas-BMT equation becoming a function of the transverse magnetic fields $\vec{B}_\perp$ of the accelerator. This leads to a spin precession around the vertical fields of the guiding dipole magnets of the synchrotron. The polarisation of the beam is merely preserved in this vertical y-axis of a curvilinear coordinate system[4] denoted as spin stable direction or quantisation axis. According to Equation (5.7) the number of spin precessions during one single circuit in the machine, the so-called spin tune ν_s, is given by

$$\nu_s = G\gamma \tag{5.8}$$

in the coordinate basis of the moving particle. The spin tune frequency becomes $\nu_s = 1 + G\gamma$ in the laboratory frame when taking into account the extra rotation associated with the one single circuit of the beam particles. The correlation between spin tune and the particle's Lorentz factor γ and hence the momentum or energy can be exploited for a high precision beam momentum determination.

5.1.2. Imperfection and intrinsic depolarising resonances

In a real synchrotron the motion of beam particles is much more complex than described by the closed orbit. Due to unavoidable field errors, misalignments of magnets, and the focussing and defocussing magnetic fields of the quadrupoles, the particles are exposed higher order magnetic fields with $\vec{B}_\parallel \neq 0$ disturbing the spin precession around the spin stable direction. Each "perturbation field" induces a deflection of the spin vector with respect to the x-axis of the curvilinear coordinate system. If the frequency of a perturbation field coincides with that spin-precession ν_s, the beam will depolarise. Such depolarising resonances occur only at fixed beam momenta since the spin tune frequency is a function of the relativistic γ factor. This important fact has to be taken into account for acceleration of polarised beams. A detailed description of the spin dynamics in a synchrotron as well as methods to preserve the polarisation during acceleration can be found in [Lee97].

Imperfection resonances

One kind of first-order resonance is the "imperfection resonance". It is caused by the vertical closed-orbit errors due to field errors and misalignments of the magnets.

[4] A curvilinear coordinate system $(\hat{x}, \hat{y}, \hat{s})$ is chosen for particle motion in synchrotrons with respect to the reference orbit $\vec{r_0}(s)$. The point in space for a particle is completely defined via (x, y, s), whereas s represents the distance passed, $x = x(s)$ horizontal, and $y = y(s)$ the vertical deviation of the reference or closed orbit. A more detailed description is given in [Hin08, Lee07].

If the spin tune is an integer $\gamma G \in \mathbb{Z}$, then the horizontal imperfection fields of the synchrotron can interact resonantly with the particle spin, building up effects coherently turn by turn. The positions in momentum of the depolarising imperfection resonances depend on the gyromagnetic anomaly of the particle. In case of protons ($G_p = 1.792847$) five resonances appear in the COSY momentum range; the first one at a momentum of 464 MeV/c. For deuterons ($G_d = -0.142987$) the first resonance occurs at ≈ 13 GeV/c, which is well outside the COSY momentum range. For the beam momenta used in the beam time (see Table 3.2) the spin tune remains in the region of $\nu_s = 0.2775 - 0.2818$.

Intrinsic resonances

Another kind of first-order resonance is the "intrinsic resonance" caused by horizontal fields of the vertical focussing. In a real synchrotron most particles do not circulate on the closed orbit, but rather on a trajectory distributed around it. Such a motion is denoted as betatron motion and results in a transverse oscillation of the circulating particles around the closed orbit. Because of the betatron oscillation frequency of the circulating beam, the particles encounter fields of the focusing quadrupole magnets in resonance with the spin tune leading to a depolarisation. The position in momentum of intrinsic resonances depends on the vertical betatron tune ν_y and the superperiodicity P of COSY, which is given by the number of identical periods of the accelerator's magnetic structure. At COSY the superperiodicity can be chosen to be $P = 2$ or $P = 6$ and the resonance condition is described by

$$\gamma G = kP \pm (\nu_y - 2) \ , \tag{5.9}$$

where k is an integer. For a deuteron beam the intrinsic resonances occur also for energies that are far beyond the COSY momentum range [Leh97, L$^+$03].

5.1.3. Artificially induced depolarising resonance for beam momentum determination

An artificially induced depolarising resonance can be generated by introducing a local horizontal magnetic rf field from either a solenoid or dipole in the synchrotron. Depending on the form of the field, this resonance can be used to depolarise the beam, to measure the spin tune, or even to flip the spin direction of the beam particles. The spin-resonance frequency f_r for a planar accelerator without horizontal magnetic fields is given by [D$^+$80]

$$f_r = (k + \gamma G) f_0 \ , \tag{5.10}$$

where f_0 is the revolution frequency of the beam, γG is the spin tune, and k is an integer. If the rf frequency of this perturbation is close to the spin-resonance frequency, the spin motion and consequently the beam polarisation will be maximally influenced leading to a beam depolarisation. The magnitude of the depolarisation depends on the resonance strength ϵ

$$\epsilon = \frac{1}{\sqrt{2}\pi} \frac{e(1+\gamma G)}{p} \int B_{\text{rms}} dl \ . \tag{5.11}$$

In this equation is p the beam momentum and $\int B_{\text{rms}} dl$ the solenoid's rms magnetic field integral [M+04]. The intrinsic width w (FWHM) of the resonance is defined by

$$w = 2\,\epsilon\, f_r \tag{5.12}$$

and can be estimated from the resonance strength ϵ and frequency f_r [M+04].

During the η mass beam time the resonance with $k = 1$ was used for the deuteron beam momentum determination because it matches the frequency range of the rf solenoid installed at COSY (see Section 4.2.2). The particles' kinematic γ factor can be determined purely by measuring both, the revolution and spin resonance frequency according to Equation (5.10)

$$\gamma = \frac{1}{G_d} \left(\frac{f_r}{f_0} - 1 \right) \ . \tag{5.13}$$

Consequently, the deuteron beam momentum p_d can be calculated

$$p_d = m_d\, \beta\, \gamma = m_d \sqrt{\gamma^2 - 1}\ , \tag{5.14}$$

using the relation $\beta\gamma = \sqrt{\gamma^2 - 1}$. It is important to note that horizontal magnetic fields in the accelerator lead to modifications of the spin tune, i.e., Equations (5.8) and (5.10). In order to avoid such complications in the beam momentum determination, all solenoidal and toroidal magnets in the COSY ring were switched off during the beam time. Residual shifts in the resonance frequency arising from field errors and vertical orbit distortions were estimated and found to be negligibly small. These effects are discussed in more detail in Section 5.3.3.

According to Equations (5.13) and (5.14) a high precision beam momentum determination can be realised by measuring the revolution frequency f_0 (see Section 5.2) and the corresponding spin resonance frequency f_r (see Section 5.3) of a polarised beam.

5.2. Revolution frequency

The radio frequency signal of the accelerating cavity predetermines the revolution frequency of the stored beam in a circular accelerator. The radio frequencies of the bb cavity for the thirteen different energies[5] used in the η mass beam time are listed in Table 5.1.

Data Points	Beam momentum p_d / (MeV/c)	bb cavity frequency f_0 / (Hz)
0	3120	1400771
1	3146	1403831
2	3147	1403947
3	3148	1404064
4	3150	1404296
5	3152	1404529
6	3154	1404761
7	3158	1405224
8	3162	1405686
9	3167	1406261
10	3171	1406720
11	3176	1407292
12	3183	1408089

Table 5.1.: Frequencies of the bb cavity measured with an oscilloscope for the thirteen different energy settings.

The deuteron beam momenta in a range of $3100 - 3200\,\mathrm{MeV/c}$ correspond to bb cavity frequencies of $1.401 - 1.408\,\mathrm{MHz}$. These quantities do not represent the true revolution frequency because the bb cavity signal was measured by an oscilloscope with a large measurement uncertainty. Additionally, possible orbit variations in time have to be taken into account. The measurement of the Schottky noise of the beam provides a much more precise technique for determining the orbital frequency.

[5] The subthreshold data at $Q \approx -5\,\mathrm{MeV}$ and $Q \approx -4\,\mathrm{MeV}$ below η production is marked in all further tables as "data point 0".

5.2.1. Schottky Noise of the circulating beam

In the beginning of the 20th century Walter Schottky discovered that a current created by a finite number of charge carriers always has some statistical fluctuations, denoted as "Schottky noise" [Sch18]. A beam stored in a circular accelerator represents such a current consisting of a finite number of charged particles. These are distributed statistically in the beam leading to such random current fluctuations. If the beam passes a beam pickup electrode in the ring the fluctuations will induce a voltage signal. The Fourier transform of this voltage-to-time signal by a spectrum analyser delivers the frequency distribution around the harmonics of the revolution frequency of the beam. As mentioned in Section 4.2, the beam pickup and spectrum analyser of the stochastic cooling system of COSY were used for the measurement of the Schottky noise. The analyser measures primarily the Schottky noise current, which is proportional to the square root of the number of the particles in the beam. Therefore, the amplitudes of the measured distribution needed to be squared to get the Schottky power spectrum representing the momentum distribution of the beam [Bou87]. The spectrum analyser was operated in the range of the thousandth harmonic, i.e., at about 1.4 GHz, but, because of the twelve different energies and hence revolution frequencies (see Table 5.1), harmonics from 997 to 1004 were also measured.

5.2.2. Method for determining revolution frequencies

The Schottky noise spectra were recorded every 30 s throughout the whole beam time so that altogether nearly 16 000 distributions were collected, sorted, and assigned to an energy. More than 99 % of them were used for the further analysis [Gos08], i.e., roughly thousand spectra for each energy. Only one spectrum was recorded in each cycle during the 36 s long cycles of the spin resonance measurements. Conversely, six spectra were measured during the 206 s long cycle used for the ANKE data taking (see Tables 4.3 and 4.4). The large amount of Schottky spectra allows to study the long term stability of the revolution frequency, which will be discussed in Section 5.2.4.

Figure 5.1 shows one example for such a spectrum, normalised to the first harmonic, for the first beam momentum above threshold ($p_d = 3146\,\mathrm{MeV/c}$) of the first supercycle. Due to the short Schottky measuring time the frequency distribution is not really smooth and the data points show strong fluctuations. However, the large amount of spectra provides good statistics allowing for a precise determination of the revolution frequency.

In context of the Diploma thesis [Gos08] two different methods were used to calculate a mean orbital frequency for each energy.

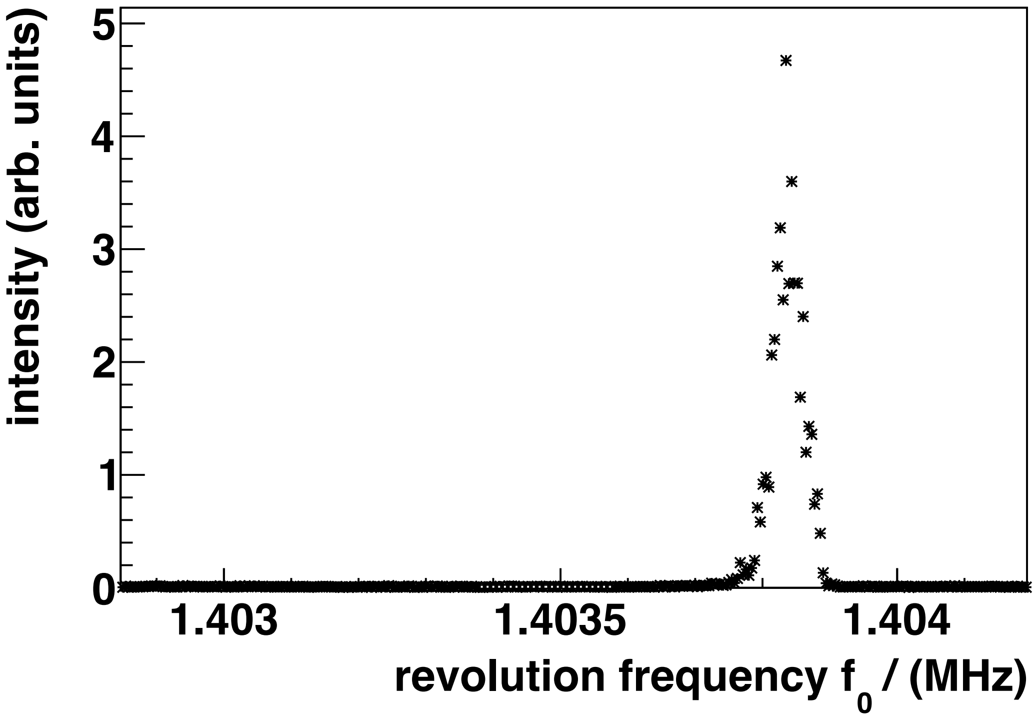

Figure 5.1.: Single Schottky power spectrum, recorded at $t = 30\,\mathrm{s}$, for the first energy above threshold of the first supercycle, normalised to the first harmonic.

In the first case the weighted arithmetic mean frequency was calculated for each single Schottky spectrum. The average of all these mean frequencies for all the Schottky spectra at one particular energy represents the mean revolution frequency for this accelerator setting.
Another way for the determination of the revolution frequency is given by calculating a mean Schottky spectrum from all the spectra recorded under the same conditions at a particular energy. Therefore, an intensity mean value was calculated from all spectra for each frequency value on the abscissa. Figure 5.2 depicts such a mean Schottky power spectrum extracted from the Schottky measurements over the five days of data taking.

The full width of half maximum is in the region of 40 Hz to 50 Hz for all energies. The position of the mean distribution of the circulation frequency is stable for the whole cycle time, but within the cycle, a small tail is seen at lower frequencies. This corresponds to beam particles that escaped the influence of the bb cavity, e.g., because of beam-target interaction, but still circulated in COSY. By calculating the weighted arithmetic mean of the orbital frequency distribution, an average revolution frequency was estimated. The results for the mean revolution frequency of both

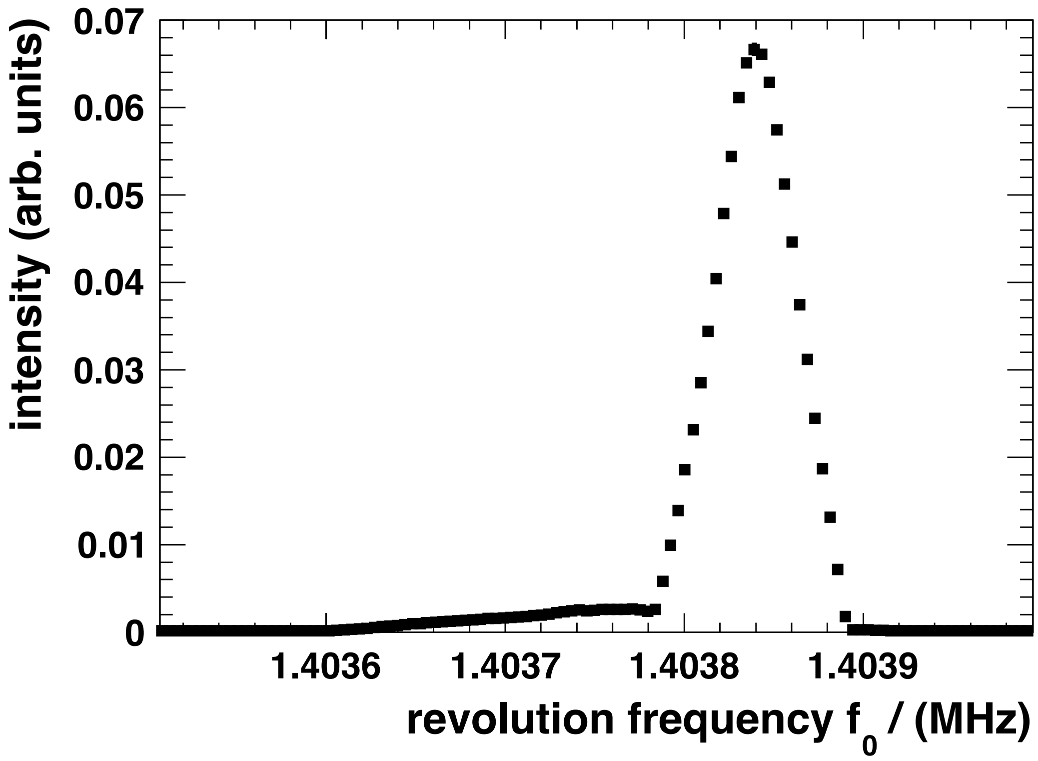

Figure 5.2.: Mean Schottky power spectrum extracted from measurements over the five day of data taking at a beam momentum of 3146 MeV/c. The statistical error bars lie within the data points. An average revolution frequency of $f_0 = 1\,403\,831.75 \pm 0.12\,\mathrm{Hz}$ was deduced by calculating the weighted arithmetic mean.

methods agree within their statistical uncertainties, which are below $\pm 0.2\,\mathrm{Hz}$. The statistical uncertainty depends on both the number of measured Schottky spectra and on the distribution variations.

5.2.3. Results of the revolution frequency analysis

By the use of the two methods described in the previous section the behaviour of the revolution frequency in COSY was studied in detail [Gos08]. In the following the most important results will be summarised exclusively. First the long term stability of the circulating frequency will be discussed. Afterwards the extracted mean revolution frequencies of the spin resonance measurements with the polarised source are compared with those ones for the data taking time with ANKE using the unpolarised source.

Long term stability of the revolution frequency in COSY

The large number of Schottky measurements allow to investigate the long term stability and to identify the magnitude of the variations of the revolution frequency in COSY. For this purpose only spectra were used which were recorded during the five days of data taking with ANKE in the supercycle mode.
In the first step the mean revolution frequencies for each energy over the five days were extracted from the mean Schottky spectrum. In the second one the revolution frequencies for these data were calculated for each of the five days to study the daily variation of the circulation frequency. The differences between the daily mean revolution frequency and the average frequency for all the five days of data taking are presented in the left part of Figure 5.3 for the first energy of the first supercycle exemplarily.
In order to investigate the variations of the revolution frequency over one day, the same procedure was carried out for Schottky data measured every four hours. The differences between the mean revolution frequency for every four hours and the mean frequency of the whole day are presented in the right part of Figure 5.3. The horizontal bars represent the time intervals for which the revolution frequency was evaluated. As it can be seen from Figure 5.3 the analysis points out that the revolution frequency over one day and also over five days is very stable at COSY. The variations are very small being in the order of 1 Hz at circulation frequency of $f_0 \approx 1.4\,\text{MHz}$ for all energies.

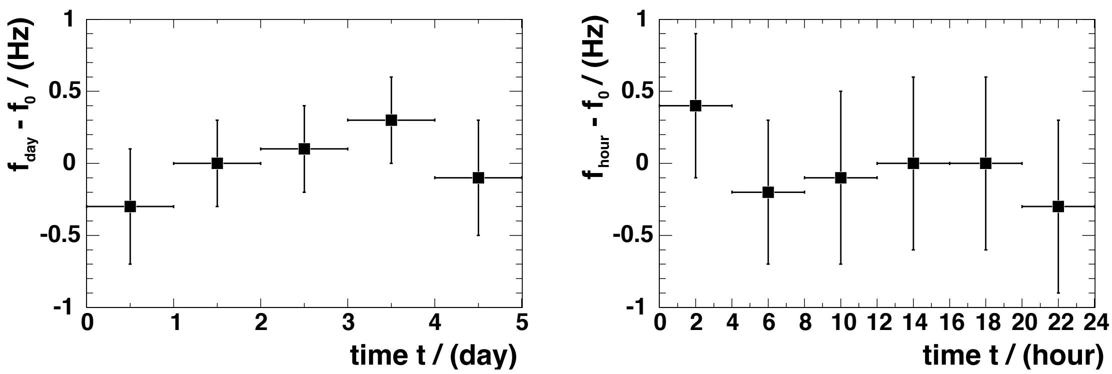

Figure 5.3.: Stability of the revolution frequency f_0. In the left panel the differences between the mean revolution frequencies for each single day and the average one for five days of Schottky data taking are shown. In the right panel the differences between the mean revolution frequencies of four hour time periods and the average one for this single day are shown. From these plots it is clear that the orbital frequency at COSY is very stable, with variations below 1 Hz at a circulation frequency of $f_0 \approx 1.4\,\text{MHz}$.

Additionally, a brief COSY switch off during the beam time allowed to verify the reproducibility of the revolution frequency at COSY. The analysis of the Schottky mean power spectra before and after the COSY shutdown shows that the extracted circulation frequencies are consistent within their uncertainties.

Comparison of the mean revolution frequencies for the polarised and unpolarised source mode

As pointed out in Section 4.4.2 the polarised beam was used exclusively for the spin resonance measurements, whereas the unpolarised one was used for data taking with ANKE in order to reach the required luminosity. Due to the fact that all COSY settings are identical for these two situations the beam momentum must be equal [PS08]. A comparison of the circulating frequencies for these two cases, i.e., for polarised and unpolarised source, allows to prove this statement. Therefore, the different timing cycle lengths have to be taken into account (see Tables 4.3 and 4.4). While during the spin-resonance measurements using a polarised beam the Schottky spectra were recorded at $t = 30\,\mathrm{s}$ in the $t = 36\,\mathrm{s}$ long cycle, with unpolarised beam a spectrum was measured every 30 s in the $t = 206\,\mathrm{s}$ long cycle. Due to beam-target interactions beam particles can escape the influence of the bb cavity and circulate then with lower frequencies in COSY. This is represented by a tail at 1.4036-1.4038 MHz in Figure 5.2. The amount of particles in the tail increases and the lowest frequency of the tail decreases within the cycle leading to a reduction of the mean revolution frequency of about 6 Hz within the cycle period of 206 s [Gos08].

By considering only the spectra measured at $t = 30\,\mathrm{s}$ during the 206 s long cycle for the calculation of the mean Schottky power spectrum the revolution frequencies with polarised source and with unpolarised source can be directly compared. Because in this case the two revolution frequency distributions represent the same situation of the beam in COSY. The comparison revealed for the first and second supercycle deviations from $-3\,\mathrm{Hz}$ to $5\,\mathrm{Hz}$, but showed for the third supercycle that the revolution frequencies agree within their uncertainties [Gos08].
One reason for the variations of the circulation frequencies may be the switching from one ion source (polarised) to the other one (unpolarised). Another possibility for the variations is given by the preparation of the Schottky spectrum analyser. While for the third supercycle the frequency range of the spectrum analyser was the same polarised and unpolarised source, it was changed for the first and second supercycle to optimise the resolution.

In addition it was observed that through the adjustment of the frequency range of the spectrum analyser the measured revolution frequency deviated randomly by up to ±6 Hz from measurement to measurement [Gos08]. This justifies the assumption that the extracted mean revolution frequencies are distributed in an interval of ±6 Hz in an uniform probability distribution. This systematic uncertainty of the spectrum analyser can be regarded as statistical one because of the random variations of the extracted revolution frequency. For an uniform probability distribution the rms uncertainty of the mean value is calculated by dividing the interval width by $\sqrt{12}$ leading to an uncertainty of $\Delta f_0 = \pm 3.5\,\mathrm{Hz}$. The total statistical uncertainty is combined from the error of the spectrum analyser ±3.5 Hz and those one when extracting the mean revolution frequency from the average spectrum $\approx \pm 0.2\,\mathrm{Hz}$. Consequently, it is entirely dominated by the first one whereas the second one is negligible.

5.2.4. Revolution frequencies for beam momentum determination

The comparison of the mean revolution frequencies between the beam momentum measurement and data taking with ANKE points out that the beam situation in COSY do not change by switching from polarised to unpolarised ion source and vice versa. The frequencies agree within the intrinsic uncertainty limits of the Schottky spectrum analyser. The total statistical uncertainty is dominated by this intrinsic one of ±3.5 Hz.
Table 5.2 lists the mean revolution frequencies used for beam momentum determination for all thirteen energy settings[6]. These values were determined from the average Schottky power spectra. Additionally, it is worth noting that the deviation to those ones the bb cavity was operated with is in the range of ±6 Hz, the experimental resolution of the Schottky spectrum analyser.

[6] The subthreshold data, marked in the table as "data point 0", were measured at $Q \approx -5\,\mathrm{MeV}$ and $Q \approx -4\,\mathrm{MeV}$ below threshold corresponding to two different revolution frequencies.

Data Points	Beam momentum p_d / (MeV/c)	Mean revolution frequency f_0 / (Hz)	Uncertainty Δf_0 / (Hz)
0	3120	1400771.1 / 1400767.1	3.5
1	3146	1403831.8	3.5
2	3147	1403945.8	3.5
3	3148	1404066.7	3.5
4	3150	1404298.2	3.5
5	3152	1404524.2	3.5
6	3154	1404755.9	3.5
7	3158	1405225.2	3.5
8	3162	1405688.2	3.5
9	3167	1406260.3	3.5
10	3171	1406719.3	3.5
11	3176	1407288.2	3.5
12	3183	1408088.2	3.5

Table 5.2.: Revolution frequencies of the twelve energy settings used for the beam momentum determination.

5.3. Spin resonance frequency

In order to determine the spin resonance frequency f_r for each of the 13 energies the spin resonance spectra were recorded twice, once before and once after the five days of data taking with ANKE as described in Section 4.4. For this purpose the polarisation of the polarised deuteron beam was measured as function of the radio frequency of the induced artificially magnetic field form the solenoid. Therefore, the angular asymmetry was detected with EDDA when scattering the polarised beam on a carbon target [Sch99]. For the beam momentum determination an absolute calibration of EDDA was not required and a quantity merely proportional to the polarisation such as the left-right asymmetry was sufficient.
Figure 5.4 shows one example of a spin-resonance spectrum for the first energy above the η production threshold ($p_{\mathrm{nominal}} = 3146\,\mathrm{MeV/c}$) of the first supercylce. The non-normalised polarisation ("relative polarisation") is plotted as function of the radio frequency of the induced horizontal magnetic field generated by the solenoid.

The resonance condition given by Equation (5.10) is not fulfilled for magnetic fields with frequencies of 1.0116 MHz and 1.0120 MHz resulting in a high beam polarisation. In contrast the particles' spin was maximally influenced and the beam depolarised when the frequency of the solenoid coincided with that one of spin-precession. For all energies a full width at half maximum in the region of $80-100$ Hz was found. Unlike the earlier spin-resonance test measurement with a coasting beam, i.e., no cavities and no internal target [S+07b, S+07a], the spin-resonance spectra are not smooth. They do not have a pure Gaussian shape as those one in [S+07b, S+07a]. The structures, especially the double peak in the centre, are caused by the interaction of the deuteron beam with the bb cavity. However, by comparing the spin-resonance spectra measured for an unbunched and a bunched beam with the standard accelerating rf cavity or even with the bb cavity, it was found that the centres of gravity of the spectra were the same [Gos08].

5.3.1. Method for determining spin resonance frequencies

In order to extract the correct spin-resonance frequency from the spectra, the shapes, especially the structures in the centre had to be studied in more detail. Therefore all 26 distributions were fitted with Gaussians and then shifted along the abscissa so that the mean value of each individual spectrum becomes zero. In addition, each spectrum was shifted along the ordinate so that the off-resonance polarisation vanished. Finally, the data was scaled to a uniform height and displayed together in a single plot to allow a comparison of all spectra. The resulting

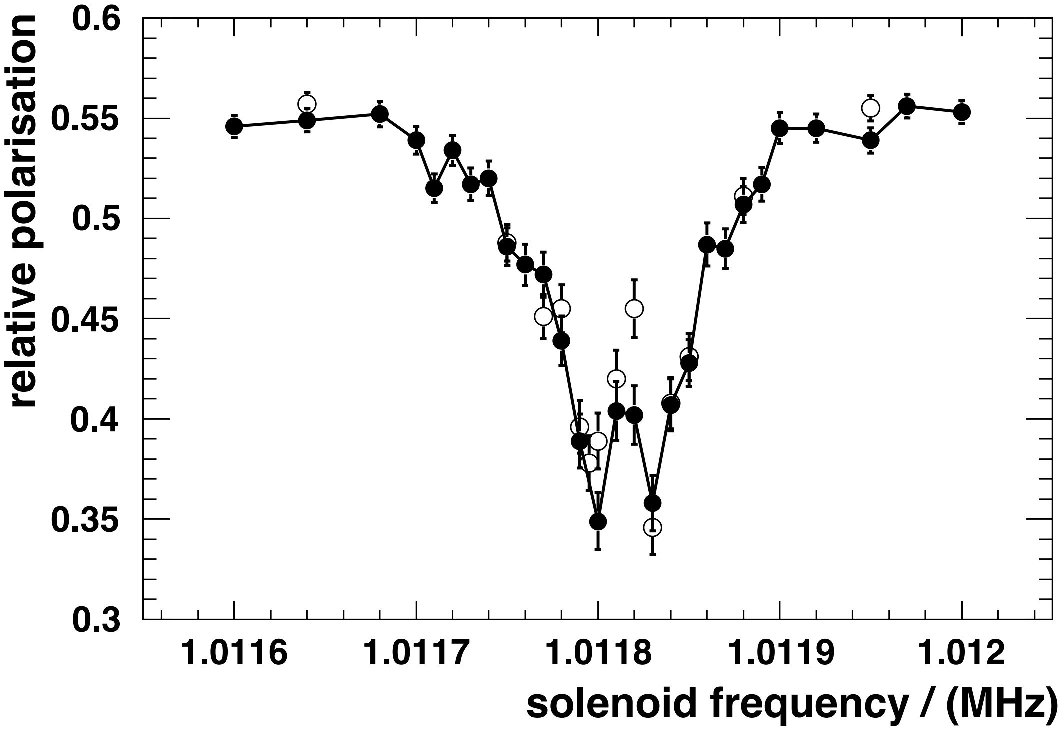

Figure 5.4.: Spin-resonance spectrum (closed circles) at a nominal beam momentum of $p_d = 3146\,\text{MeV/c}$ measured with the cycle timing described in Table 4.3. The open symbols represent results obtained for an extended cycle time, where the perturbing solenoid was switched on after 178 s.

global spin-resonance spectrum, shown in the top part of Figure 5.5, is symmetric around zero and smooth, except for the structure at the centre. This region is shown in greater detail in the inset. In order to improve the visibility of the structures close to the minimum, the size of the frequency bins was increased and the results displayed in the bottom part.

A structure with a symmetric double peak and a narrow oscillation appears in the centre of the spin resonance, clearly visible in the global spectrum, whereas indicated weakly only in the individual spectra. Consequently the spin resonance spectrum is a superposition of a Gaussian function and this pattern. However, it is important to note that the Gaussian mean value, i.e., the spin-resonance frequency, can be disentangled and is not influenced by this structure. This was checked by making fits to the global spectrum as well as to each single one, where the data points at the centre were excluded. Within the uncertainty limits the extracted spin-resonance frequencies agree with those extracted by a fit to the spectra with

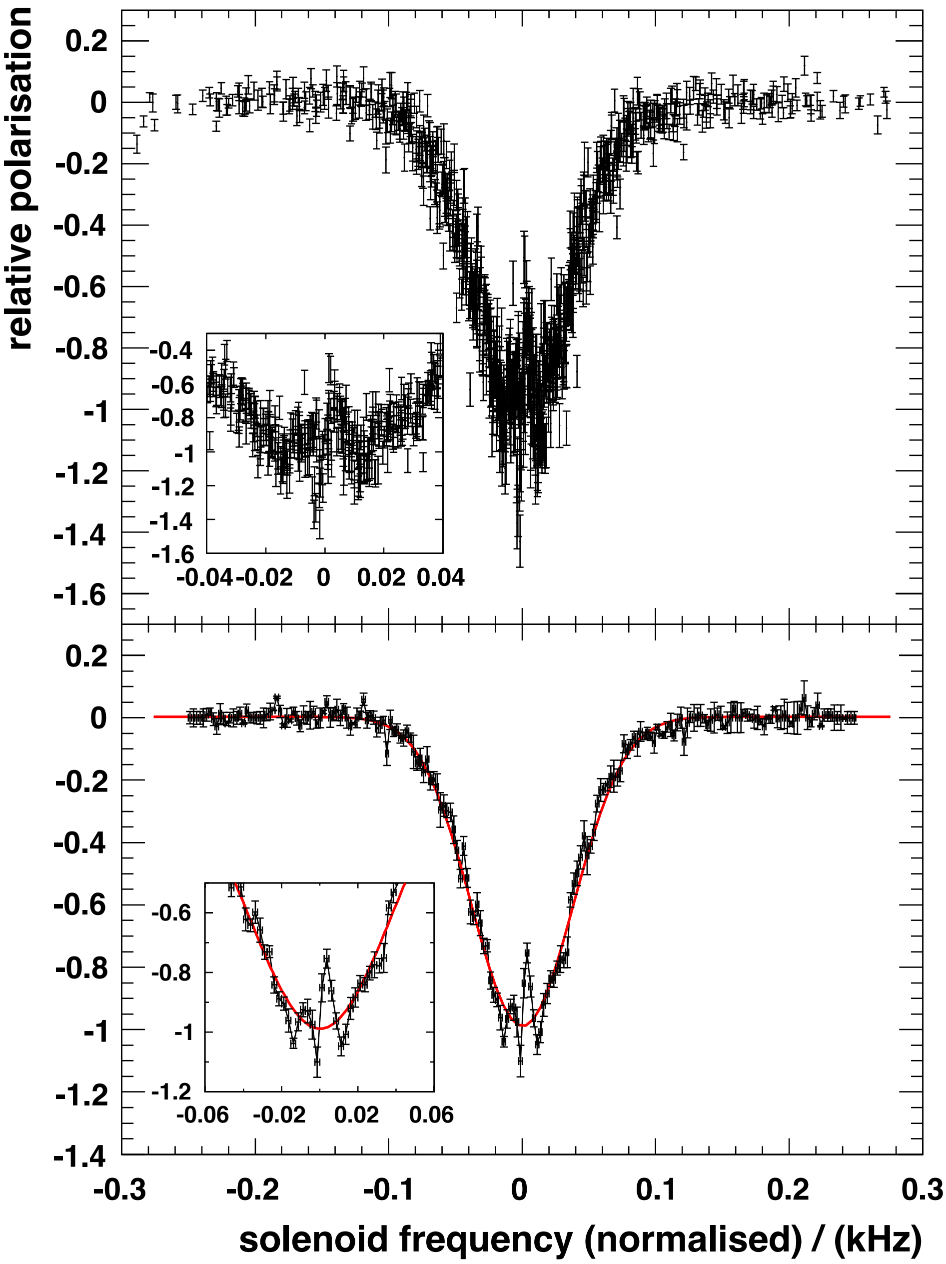

Figure 5.5.: Top: The spin-resonance spectra normalised by a Gaussian. **Bottom:** The same but with larger bins on the abscissa. The spin-resonance shape is symmetric about zero and smooth except in the centre, where a double peak structure is seen. The structures, especially the double peak, are caused by the interaction of the deuteron beam with the bb cavity. The insets show the resonance valley in greater detail.

all data points. By this, the validity of extracting the spin-resonance frequency f_r by making a Gaussian fit to the spin-resonance spectrum have been verified. The description with a Gaussian gave a χ^2/NDF in the region of $2-3$ for all 13 energies. The statistical uncertainties of the spin-resonance frequencies are in the order of $0.9 - 1.4\,\mathrm{Hz}$ at $f_r \approx 1.01\,\mathrm{MHz}$.

5.3.2. Results of the spin resonance frequency analysis

For the interpretation of the spin-resonance measurements it is important to know to what extent the position of the observed spin-resonance frequencies are stable over the finite accelerator cycle in the presence of a thick internal target. Therefore, various measurements were conducted at the beginning of the beam time in order to investigate the influence of different effects on the spin resonance frequency [Gos08].

Influences on f_r from cycle timing and cluster-jet target

The cycle timing for the resonant depolarisation measurements, listed in Table 4.3, has to be chosen in a way to guarantee that the beam is first accelerated to the constant beam momentum and afterwards influenced by the induced magnetic field of the solenoid. If the solenoid is switched on too early the measured spin-resonance spectrum will reflect a situation of beam acceleration. To find the point in time, at which the beam momentum remains constant for the whole cycle, the timing of the switch-on of the solenoid was changed and the spin resonance spectrum was measured. Four different measurements were conducted with the switch-on at 4, 8, 12, 20 s. While the values for the extracted spin resonance frequencies for the measurements at 8, 12, 20 s agree within their uncertainties, the frequency measured with the switch-on after 4 s deviates by about 20 Hz [Gos08]. In this case the spin resonance spectrum is still influenced by the beam acceleration. Due to this fact all further resonant depolarisation measurements were carried out using the setting listed in Table 4.3 with switching on the magnets after 20 s for ensuring a stable beam situation in COSY.

In contrast to the first test measurement [S^+07b, S^+07a], the spin resonances were measured in the presence of a thick internal cluster-jet target during the η mass beam time to guarantee the same conditions for the beam for the two different cycle modes (see Tables 4.3 and 4.4). The impact of the cluster-jet target on f_r was investigated by an additional measurement of the spin resonance spectrum using the cycle timing listed in Table 4.3 with and without target [Gos08]. Thereby no significant effect was observed. In a special much more time-consuming measurement the switch-on of the rf solenoid was delayed from 20 s to 178 s in order to investigate the position of the spin-resonance frequency close to the end of the long cycle (see Table 4.4). The observed data, depicted as open symbols in Figure 5.4 showed a resonance position which agreed with those at the beginning of the cycle to within 2 Hz [Gos08].

Shifts between first and second spin-resonance measurement

The stability of the position of the spin-resonance frequencies could be investigated in detail by comparing the resonant depolarisation measurements before and after the five days of data taking with ANKE. Both supercycles show collective shifts of the spin resonance frequencies in the range of 4 Hz up to 18 Hz, which probably originated from changes in the orbit length in COSY of about 3 mm. Figure 5.6 illustrates the shifts between the first and second resonant depolarisation measurements as red triangles for all 13 energies.

The frequencies in the first supercycle decrease between $4-10$ Hz for all energy settings corresponding to a decrease in the beam momentum of $40-100$ keV/c. For the second supercylce they increase in the range of $12-18$ Hz and hence $130-190$ keV/c in the beam momentum. Due to the fact that the revolution frequency was found to be stable as described in Section 5.2.4, the change could only be attributed to a shift in the orbit length s.

The velocity v of the particle is given as product of the revolution frequency f_0 and the orbit length s according to Equation (5.1), so that the relativistic γ factor can be written as

$$\gamma = \frac{1}{\sqrt{1 - s^2 f_0^2/c^2}} \ . \tag{5.15}$$

When inserting this expression Equation (5.13), the orbit length can be calculated from the revolution and the spin-resonance frequency:

$$s = c \left[\frac{1}{f_0^2} - \left(\frac{G_d}{f_r - f_0} \right)^2 \right]^{1/2} \ . \tag{5.16}$$

This allows an extraction of the absolute orbit lengths with a precision better than 0.3 mm for each of the 13 energies[7] resulting in a relative accuracy of $\Delta s/s \leq 2 \times 10^{-6}$. The shift in the spin-resonance frequency corresponds to a change in the orbit length of up to 3 mm, which is presented for all energy settings in Figure 5.6 as blue circles. The shifts of the spin-resonance frequencies suggest an increase in

[7] A more detailed discussion and the calculated values can be found in [Gos08].

the orbit length in the range of $0.7 - 1.6$ mm for the first supercycle and a decrease of $2.0 - 2.8$ mm for the second one.

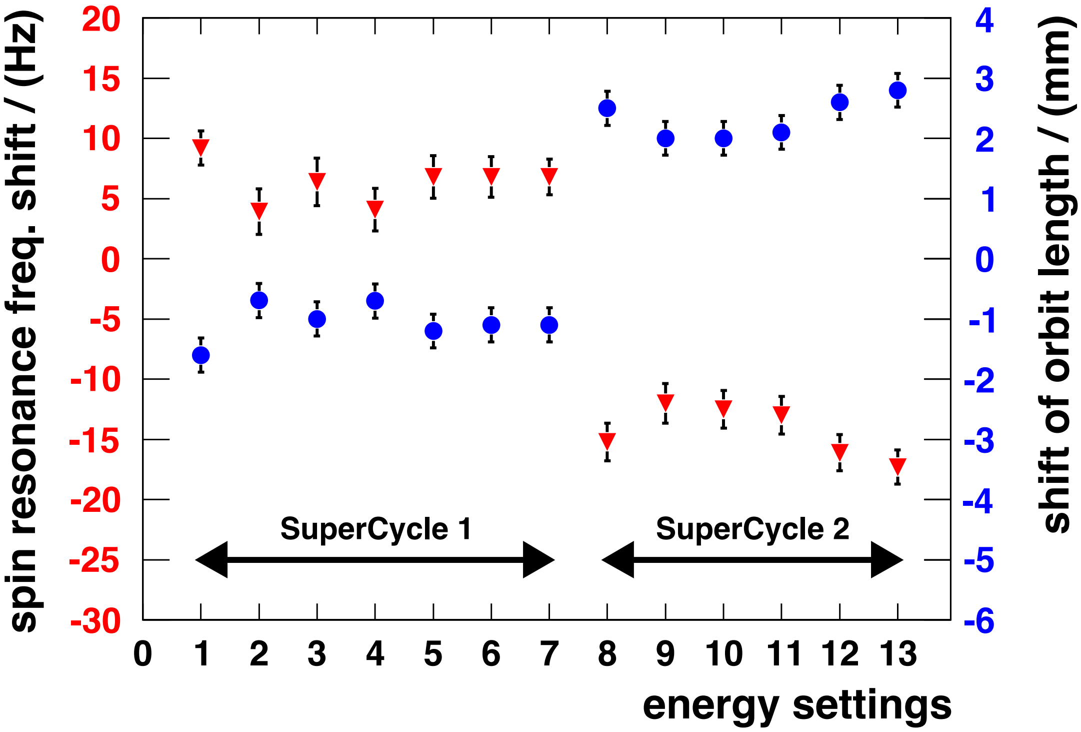

Figure 5.6.: The spin-resonance frequencies were measured twice, once before and once after the five days of data taking. The red triangles represent the shift of the spin-resonance frequency f_r from the first to the second measurement. These shifts correspond to changes in the orbit length, which are shown as blue circles. For the first supercylce, the spin-resonance frequencies decrease between the two measurements in a range of $4 - 10$ Hz, which corresponds to an increase in the orbit length in the range of $0.7 - 1.6$ mm. For the second supercylce an increase of the spin resonance in the range of $12 - 18$ Hz was observed, i.e., a decrease in the orbit length of about $2.0 - 2.8$ mm.

The shift in f_r, which implies a shift of the beam momentum, had to be factor in the threshold extrapolation. It defines the dominate systematic uncertainty of the determined beam momentum and as will be shown later also the systematic error of the obtained η mass value (see Section 7).

5.3.3. Spin resonance frequencies for beam momentum determination

Average values of the two spin resonance frequencies, measured before and after data taking, are calculated for each of the twelve energy settings for precise beam momentum determination according to Equations (5.13) and (5.14). These average values are listed in Table 5.3.

Data Points	Beam mom. p_d / (MeV/c)	Spin resonance frequency f_r / (Hz)	Stat. error $\Delta f_r^{\text{stat.}}$ / (Hz)	Syst. error $\Delta f_r^{\text{syst.}}$ / (Hz)
0	3120	1012008.6	0.7	8.7
1	3146	1011810.0	1.0	8.7
2	3147	1011805.4	0.8	8.7
3	3148	1011791.8	1.0	8.7
4	3150	1011777.6	0.8	8.7
5	3152	1011753.0	0.9	8.7
6	3154	1011732.9	0.7	8.7
7	3158	1011682.3	0.9	8.7
8	3162	1011640.2	0.8	8.7
9	3167	1011565.4	0.8	8.7
10	3171	1011517.3	0.7	8.7
11	3176	1011431.1	0.7	8.7
12	3183	1011325.6	0.6	8.7

Table 5.3.: Spin resonance frequencies of the twelve energy settings used for the beam momentum determination

While the statistical uncertainty is given by Gaussian error propagation, the systematic uncertainty was estimated from the collective shifts in f_r as described in the following. The average values differ by up to 10 Hz from the two single spin-resonance measurements for each energy. Nevertheless, the maximum uncertainty for these mean values was conservatively extended to 15 Hz in order to consider the collective shifts of 4 Hz to 18 Hz. This corresponds to a maximum shift of

$\pm 164\,\mathrm{keV/c}$ in the beam momentum. The origin for the collective shifts is likely to be caused by steady tiny changes in the deuteron orbit inside the synchrotron over the measuring period of five days. That means the orbit changed linearly in time and it is reasonable to assume that the true spin-resonance frequencies or beam momenta give a uniform probability distribution over this interval. The systematic uncertainty of the averaged spin-resonance frequencies is therefore estimated to be $\Delta f_r = 8.7\,\mathrm{Hz}$[8], resulting in a systemic beam momentum uncertainty of $p_{d,\,\mathrm{syst.}} = 95\,\mathrm{keV/c}$. Evidence in favour of the approach adopted here was found by comparing the η mass results obtained for the individual supercycles, which is discussed in Section 7.

For the sake of completeness all other possible systematic effects, which may affect the spin tune, and their contributions to the accuracy of the spin resonance frequency were evaluated and presented in the following. The evaluation showed that their contributions to the systemic error are smaller by several orders of magnitude compared to the collective shifts in f_r, so that they are completely negligible.
According to Equation (5.10), one obvious limitation on the spin-resonance method is given by the uncertainty in the deuteron gyromagnetic anomaly G_d (see Equation (5.4)). This contribution can be safely neglected, because it leads to a contribution in the beam momentum of $\Delta p/p = 5 \times 10^{-8}$, which is three orders of magnitude lower than that of the spin-resonance frequency.
As mentioned above the first-order uncertainties in the momentum measurement depend on the accuracies to which the spin resonance and revolution frequencies are determined. As described in Section 5.2.4 and listed in Table 5.2 and 5.3, these are $8.7\,\mathrm{Hz}/1.01\,\mathrm{MHz} = 8.6 \times 10^{-6}$ and $3.5\,\mathrm{Hz}/1.40\,\mathrm{MHz} = 2.5 \times 10^{-6}$, respectively. The error therefore arises primarily from the measurement of the spin-resonance frequency.

Another limit on the achievable accuracy may be imposed by the intrinsic width of the spin-resonance. In this experiment, the integrated value of the solenoid's maximum longitudinal rf magnetic field of 0.29 Tmm gives, according to Equation (5.11), a resonance strength of about $\epsilon \approx 4.5 \times 10^{-6}$, which leads to a spin resonance with a FWHM of $\approx 9\,\mathrm{Hz}$ (see Equation (5.12)). This is much smaller than the observed width of $80 - 100\,\mathrm{Hz}$, which is therefore dominated by the momentum spread of the beam. Higher order contributions bring about an additional spread in the spin frequencies caused by nonlinear synchrotron and betatron motion [LPS86]. It should be stressed that these higher order effects, which are negligible compared to the calculated resonance width, do not contribute to a shift of the resonance frequency.

[8] The true spin-resonance frequencies are assumed to be distributed in a uniform interval of 30 Hz. The uncertainty of the average value is given by the deviation of the interval width with $\sqrt{12}$, leading to $\Delta f_r = 30\,\mathrm{Hz}/\sqrt{12} = 8.7\,\mathrm{Hz}$

Systematic shifts of the spin-resonance frequency may be caused by deviations from idealised conditions in a real accelerator like COSY. The possible effects and their contribution to the accuracy of the resonance frequency determination were estimated and are summarised in Table 5.4.
Radial and longitudinal fields in the accelerator may lead to a modification of Equation (5.10) [Lee97], i.e., to a systematic shift of the resonance frequency. Even though all solenoidal and toroidal fields, which may act as partial Siberian Snakes, were turned off for this experiment, field errors and vertical orbit distortions could generate some net radial or longitudinal fields [B+87, A+92]. These effects were estimated for the experimental conditions and found to be negligible small. The typical field errors of the main magnets, $\Delta B/B \approx 2 \times 10^{-4}$, would induce a shift in the spin-resonance frequency of $\Delta f_r/f_r < 1.4 \times 10^{-9}$. Similarly, the observed vertical orbit displacement of $\Delta y_{\text{rms}} < 1.8\,\text{mm}$ give rise to a shift of $\Delta f_r/f_r < 6.0 \times 10^{-9}$.
However, the largest input to a systematic shift of the resonance frequency could come from the vertical closed orbit deviations in the quadrupole magnets of the ring. This contribution of $\Delta f_r/f_r < 4 \times 10^{-8}$ is comparable to the in-principle limiting of the method arising from the knowledge of the deuteron G factor. In summary, all discussed contributions are over two orders of magnitude below the accuracy achieved in the experiment and therefore entirely negligible.

Source	$\Delta f_r/f_r$
Resonance accuracy from depolarisation spectra	8.6×10^{-6}
Spin tune shifts from longitudinal fields (field errors)	1.4×10^{-9}
Spin tune shifts from radial fields (field errors, vertical correctors)	6.0×10^{-9}
Spin tune shifts from radial fields (vertical orbit in quadrupoles)	4.1×10^{-8}

Table 5.4.: Accuracy and possible systematic shifts of the spin-resonance frequency f_r.

5.4. Determination of the deuteron beam momenta

The kinematic γ factors and beam momenta were calculated according to Equations (5.13) and (5.14) from knowledge of revolution and spin-resonance frequencies (see Tables 5.2 and 5.3). The accuracies to which both frequencies are determined are dominated by systematic effects. Nevertheless, both systematic errors have to be treated in different ways.
The systematic error of the revolution frequency, caused by the preparation of the Schottky spectrum analyser, can be handled in the error propagation as statistical

one, due to the fact that the measured frequencies are randomly distributed around the true value. The revolution frequencies are subject to an uniform distribution. The beam momentum's statistical uncertainty is given by the revolution and spin-resonance frequencies through error propagation. It is entirely dominated by that of the revolution frequency of $\Delta f_0 = \pm 3.5\,\mathrm{Hz}$, which corresponds to a statistical uncertainty in the beam momentum of $\Delta p_d^{\mathrm{stat.}} = 29\,\mathrm{keV/c}$. An example of the reconstructed beam properties with statistical uncertainties is presented in Table 5.5 for the lowest and highest energy setting above the η production threshold.

Nominal beam mom.	3150.5 MeV/c	3187.5 MeV/c
Revolution freq.	(1403831.8 ± 3.5) Hz	(1408088.2 ± 3.5) Hz
Spin-resonance freq.	(1011810.0 ± 1.0) Hz	(1011325.6 ± 0.6) Hz
Orbit length	(183.4341 ± 0.0002) m	(183.4579 ± 0.0002) m
Relativistic γ factor	1.9530 ± 0.0001	1.9706 ± 0.0001
Spin tune ν_s	0.27925 ± 0.00001	0.28177 ± 0.00001
Beam momentum	(3146.409 ± 0.029) MeV/c	(3184.874 ± 0.028) MeV/c

Table 5.5.: Results of import beam features are shown only with statistical uncertainties for the lowest and highest energy above the η production threshold, exemplarily.

An important fact, which was discovered at the beginning of the beam time by a fast analysis of the first spin-resonance measurements, was that the measured beam momenta differed by about 4.5 MeV/c from the nominal requested ones. By that the excess energy values (see Table 3.2) would be lowered by about 1.1 MeV. Therefore, all COSY energy settings were increased by 4.5 MeV/c in order to correct for this deviation.

The main uncertainty of the beam momentum is caused by the systematic and collective shifts of the spin-resonance frequencies. The maximum shift of the average were estimated conservatively to be $\Delta f_r = \pm 15\,\mathrm{Hz}$ corresponding to a shift in the beam momentum of $\pm 164\,\mathrm{keV/c}$. As discussed in Section 5.3.3 it is reasonable to assume that the beam momentum changed linearly in time to give a uniform probability distribution of the momenta over this interval. The systematic uncertainty of the averaged beam momentum values is therefore estimated to be $\Delta p_d^{\mathrm{syst.}} = 95\,\mathrm{keV/c}$ (rms). A confirmation of the assumed approach for the uncertainty determination is given by the comparison of the individual η mass results obtained for each of the two supercycles, which is discussed in Section 7. In total, the twelve beam momenta in the range of $3100 - 3200\,\mathrm{MeV/c}$ were measured with an overall accuracy of $\Delta p_d/p_d = 3 \times 10^{-5}$. This is over an order of magnitude better than ever reached before for a standard experiment in the COSY ring and it is sufficient to satisfy the needs of a competitive η mass measurement. The quantities are listed with their statistical and systematic uncertainties in Table 5.6.

Data Points	Desired mom. p_d / (MeV/c)	Determined mom. p_d / (MeV/c)	Stat. error $\Delta p_d^{\text{stat.}}$ / (MeV/c)	Syst. error $\Delta p_d^{\text{syst.}}$ / (MeV/c)
0	3120	3120.166	0.028	0.095
1	3146	3146.409	0.029	0.095
2	3147	3147.353	0.028	0.095
3	3148	3148.449	0.029	0.095
4	3150	3150.417	0.028	0.095
5	3152	3152.454	0.029	0.095
6	3154	3154.485	0.028	0.095
7	3158	3158.705	0.029	0.095
8	3162	3162.779	0.028	0.095
9	3167	3168.055	0.029	0.095
10	3171	3172.153	0.028	0.095
11	3176	3177.515	0.029	0.095
12	3183	3184.874	0.028	0.095

Table 5.6.: Precise determined beam momenta for the twelve energy settings used for the threshold extrapolation.

According to Equations (5.10) and (5.15) two further quantities, the beam momentum smearing $\partial p/p$ and the smearing of the orbit length distribution $\partial s/s$, can be extracted from the spin-resonance spectra. As discussed in Section 5.3, the measured spin-resonance width of $80-100$ Hz are dominated by the momentum spread. Assuming a Gaussian distribution in the revolution frequency with a FWHM $\approx$ 50 Hz (see Section 5.2.2), and neglecting other effects, then the width of the spin-resonance distribution requires a momentum spread of $(\partial p/p)_{\text{rms}} \approx 2 \times 10^{-4}$. This upper limit on the beam momentum width corresponds to a smearing of the orbit length of $(\partial s/s)_{\text{rms}} \approx 4 \times 10^{-5}$. For a verification of these quantities the momentum spread was checked from the frequency slip factor η, which was measured at each energy. Using the equation

$$\frac{\partial p}{p} = \frac{1}{\eta} \frac{\partial f_0}{f_0} \,, \tag{5.17}$$

this leads, for example, at $p_d = 3158.705$ MeV/c to $(\partial p/p)_{\text{rms}} = 1.4 \times 10^{-4}$, which is consistent with the limit obtained from the resonance distribution.

6. Final state momentum determination

The η mass evaluation at COSY-ANKE relies on the identification of the production threshold referring to the reaction $\mathrm{d\,p} \rightarrow {}^3\mathrm{He}\,\eta$ by investigating the increase of the final state momentum as function of the beam momentum, as described in Section 3.2. Corresponding to the twelve fixed beam momenta, it is essential to gain an accurate knowledge of the associated CM momenta of the ${}^3\mathrm{He}\,\eta$ final state. The final state momentum determination as well as the final η mass value are already published in [G+12]. This publication briefly explains the p_f analysis focusing on the most important steps, exclusively. That is why a more detailed discussion will be presented in this thesis. Naturally some of the following text passages, i.e., ideas and contributions, will be very similar, partly identical with its predecessor. So in this case, there will be very few text references with the exception of contributions or ideas made by other authors.

An accurate ${}^3\mathrm{He}\,\eta$ final state momentum determination depends on a precise momentum reconstruction for registered particles in the forward system. This in turn relies on a careful calibration of the ANKE spectrometer, achieved in a two step procedure.
The standard Fd system calibration, based on the investigation of different reference reactions explained in Section 6.2.1, was verified and improved by a so called fine tuning of calibration parameters. This technique, discussed in Section 6.3, takes advantage of the simple two-body kinematics of the reaction of interest $\mathrm{d\,p} \rightarrow {}^3\mathrm{He}\,\eta$. Such procedure is only possible because ANKE has full geometrical acceptance for the reaction in the energy range considered. The initial idea for this kind of fine tuning was initiated by T. Mersmann shortly outlined in [Mer07] and further developed in the presented analysis. The main ideas and their crucial points will be discussed at the beginning of Section 6.1 by using Monte Carlo simulations.

The analysis followed three main objectives in order to tune the calibration parameters and determine precise final state momenta:

1. The reaction $\mathrm{d\,p} \rightarrow {}^3\mathrm{He}\,\eta$ had to be separated clearly and accurately from background reactions. Therefore, the ${}^3\mathrm{He}$ particles were identified and the raw background was suppressed in the event selection. It mainly consists

of deuterons and protons from the d p elastic scattering and protons from deuteron breakup. Their contributions were suppressed by cuts on the energy loss and path length of charged particles in the Fd system. The remaining background, originating primarily from some residual deuteron breakup and multi pion productions, was described and subtracted by the use of data taken below η threshold at an excess energy of $Q \approx -5\,\mathrm{MeV}$ (see Section 6.2).

2. In the second step it was indispensable to study and to verify the pure $^3\mathrm{He}\,\eta$ signal in greater detail. The reconstructed momenta can be shifted in comparison to the true ones caused by resolution or smearing effects always present in any real detector. These effects will be explained in detail in Section 6.1. A careful study of the momentum reconstruction of the Fd system of ANKE was mostly necessary for understanding and compensation for such resolution effects. After having calibrated the spectrometer by measuring a variety of other nuclear reactions in the scope of the standard Fd system calibration method, the requisite precision was achieved by using the so called refined calibration tuning. Thereby it is demanded that the magnitude of the true $^3\mathrm{He}$ momentum from the $\mathrm{d\,p} \to {}^3\mathrm{He}\,\eta$ reaction should be identical in every direction in the CM frame. This check was only possible because of the 100% angular acceptance of ANKE for the reaction of interest (see Section 6.3).

3. Finally, in the third step, the influence of smearing effects on the final state momentum were described and quantified by implementing them into Monte Carlo simulations (see Section 6.4). These simulations allow for calculating correction parameters for the measured final state momenta in order to extract the true values. Final results and estimated uncertainties are presented in Section 6.4.3.

6.1. Main ideas and their crucial points

As previously mentioned, kinematics of the $\mathrm{d\,p} \to {}^3\mathrm{He}\,\eta$ reaction provide one option for fine tuning of calibration parameters. The central idea is based on the fact that the final state momenta of a two-body reaction at a fixed centre-of-mass energy are distributed on a perfectly symmetric momentum sphere in the p_x, p_y and p_z space, i.e., on an infinitely thin surface. The constant radius represents the final state momentum p_f

$$\vec{p_f} = (p_x,\, p_y,\, p_z) = |p_f| \cdot (\cos\phi \sin\vartheta,\, \sin\phi \sin\vartheta,\, \cos\vartheta) \tag{6.1}$$

$$p_f = \sqrt{p_x^2 + p_y^2 + p_z^2} = \sqrt{p_\perp^2 + p_z^2} \tag{6.2}$$

as indicated in Figure 3.1 and discussed in Section 3.1.2. The amount of the final state momentum vector is given by Equation (3.15). By this it should be isotropic and independent of its direction. The basic concept for the fine tuning is the requirement for symmetry and isotropy of the momentum sphere according to pure "mathematical" kinematics.

It was necessary to study carefully the reconstructed momentum p_f of reconstructed events in all directions, i.e., as a function of the polar and azimuthal angle ϑ and ϕ, in order to verify if the symmetry condition is fulfilled by the ANKE standard calibration. This examination was only successful because of four reasons:

- Full geometrical acceptance of the ANKE spectrometer for $\mathrm{d\,p} \to {}^3\mathrm{He}\,\eta$
- High statistics collected during the beam time
- Effective event selection (Section 6.2.3)
- Background description and subtraction (Section 6.2.4).

In purely kinematic terms the p_f distribution can be approximated by a delta Dirac function with vanishing width. The p_f signal measured in an experiment has a shape similar to a Gaussian-like distribution with a certain width. It differs from pure kinematics because of the measuring process, i.e., the influences of smearing and resolution effects.
That means the detector response in a real experiment, composed of smearing and resolution effects and the track- and momentum reconstruction algorithms, can affect and change the isotropic momentum sphere. It was clearly indispensable to explore these influences on the reconstructed ^{3}He momentum and the missing mass distribution for the $\mathrm{d\,p} \to {}^3\mathrm{He}\,\eta$ reaction in order to improve calibration parameters and extract correctly the final state momenta.

The next section will emphasise the impact of resolution and smearing parameters on the reconstructed final state momentum signal, i.e., on the momentum sphere.

6.1.1. Influence of momentum resolution on reconstructed final state momentum

The impact of momentum resolution on the reconstructed final state momentum was studied by the use of Monte Carlo simulations, which is explained and illustrated by the two-dimensional ($p_\perp$, p_z) sketch shown in Figure 6.1.
The momentum sphere can be visualised in a simplified manner by plotting the magnitude of the transverse momentum, $p_\perp = \sqrt{p_x^2 + p_y^2}$, versus the longitudinal momentum p_z. Such a depiction means a transformation of the three-dimensional momentum sphere in p_x, p_y, and p_z into a two-dimensional semi-circle by merging

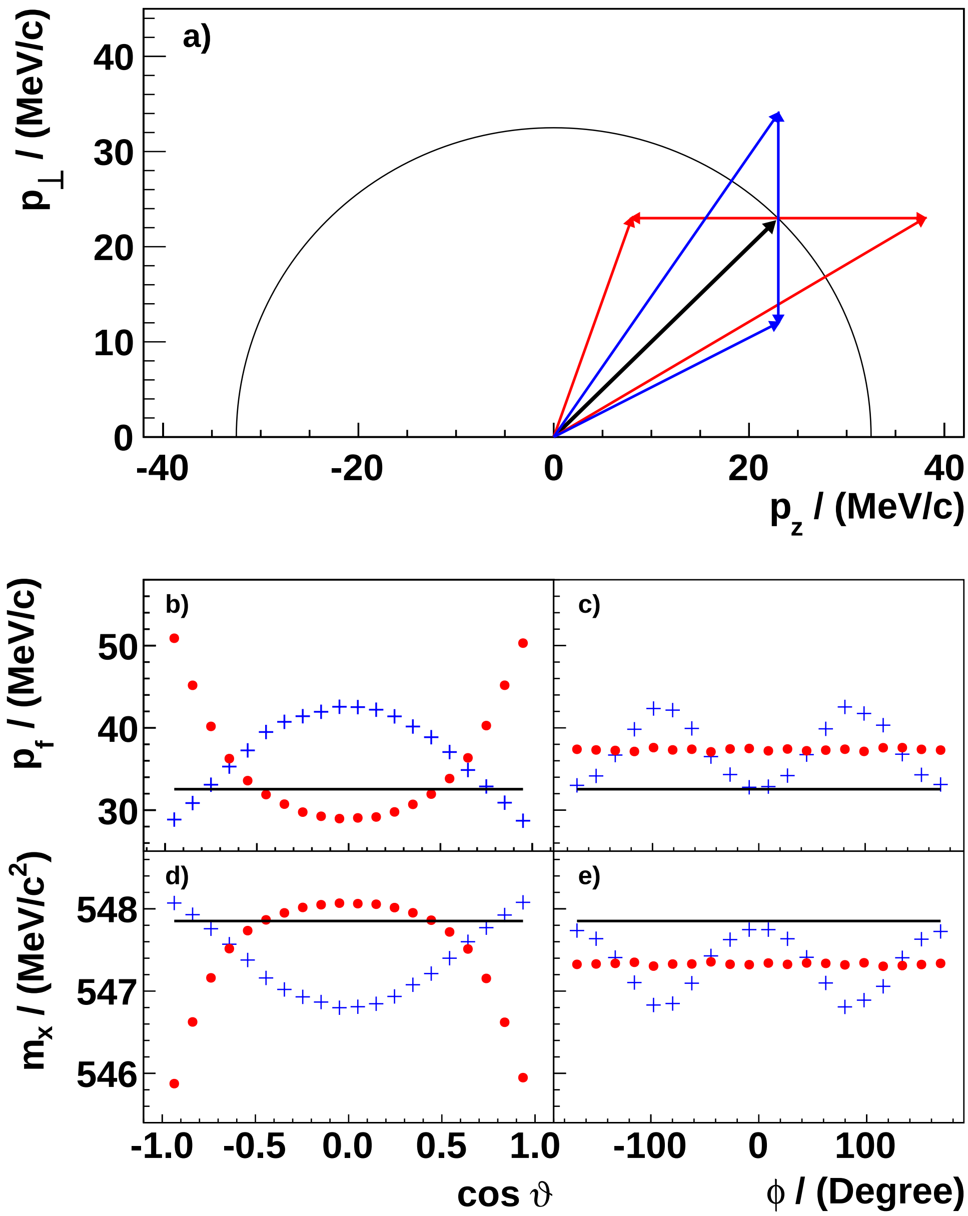

Figure 6.1.: Influence of resolution on the determination of the final state momentum. The ideal p_f sphere of panel (a) (black) is changed by finite resolution in the longitudinal (z) direction along the horizontal (red) arrow. Resolution effects in the transverse direction are indicated by the vertical (blue) arrow. Panels (b) – (e) show the possible distortions at $Q = 1.0\,\mathrm{MeV}$, evaluated in Monte Carlo simulation. The mean values for individual $\cos\vartheta$ and ϕ bins are shown without (black line) and with momentum smearing in the z-direction (red circles) and transversely (blue crosses) for both the final state momentum and the missing mass distribution.

the p_x and p_y component to the transverse momentum $p_\perp$[1].
As usual in particle physics the z-direction of the coordinate system was chosen to lie along that one of the accelerator beam, y was defined by the upward normal to the flat ring, and $\hat{x} = \hat{y} \times \hat{z}$ points to the outwards of the accelerator ring[2].
The upper part of Figure 6.1 shows the semi-circle for the reaction $\mathrm{d\,p} \to {}^3\mathrm{He}\,\eta$ for an excess energy of about $Q \approx 1\,\mathrm{MeV}$ assuming the PDG η mass value. One single event of the investigated reaction is characterised as a single point on this semi-circle with its own final state momentum vector. The angle between the $\vec{p_f}$ vector and p_z axis defines the polar angle ϑ. Whereas the azimuthal angle is located between $\vec{p_f}$ and the p_x axis.

In the ideal case of a measurement with perfect resolution, the final state momenta of the reaction events are distributed on a sphere with constant radius p_f as indicated by the black line. In this case the p_f distribution can be described by a Dirac delta function with vanishing width. Then, both the missing mass and final state momentum are isotropic, i.e., independent of $\cos\vartheta$ and ϕ as illustrated by the black horizontal line in Figures 6.1(b)-(e).

In a real experiment, however, the momenta reconstructed in the laboratory frame are smeared by the finite resolution for the individual components p_x, p_y, and p_z associated with the detector setup and reconstruction algorithms. By that an angle dependent displacement of p_f is introduced, resulting in a deformation of the perfect sphere. The final state momentum peak becomes similar to a Gaussian shape distribution with a finite width, dominated by these resolution effects. Dependent on the individual smearing for each component, the peak structure does not even have to be symmetric. If the p_f signal is studied for various angle bins in ϑ and ϕ, the displacement and width will vary according to the different resolutions in p_x, p_y, and p_z.

Assuming in Monte Carlo simulation that exclusively the z component of the momentum in the laboratory frame was smeared with a Gaussian width of say $\sigma_z = 30\,\mathrm{MeV/c}$, an event on the momentum sphere, indicated by the black arrow in Figure 6.1(a) representing p_f, could be shifted along the red horizontal arrows. It is important to note that it is just for $p_f^{\mathrm{rec}} < p_f^{\mathrm{true}}$ that events are shifted toward lower $|\cos\vartheta|$, whereas the reverse is true for $p_f^{\mathrm{rec}} > p_f^{\mathrm{true}}$. By extracting the mean values of the smeared p_f distributions for the various angle bins it becomes clear that this effect leads to a p_f dependence on $\cos\vartheta$ (see Figure 6.1(b), red circles). The momentum sphere is stretched for large longitudinal momenta and compressed for high

[1] The relation of $p_\perp$ versus p_z shows a momentum ellipsoid in the laboratory system. The ellipsoid changes into a circle when transforming the frame of reference into the CM one by Lorentz transformation. This is why the transformation affects the p_z component only as shown in Section 3.1.1. In greater detail in [BK73], page 37 et seqq. and in [Hag63], page 53 et seqq. .
[2] The coordinate system is illustrated in Figure 4.4.

transverse ones. For simple kinematic reasons, the missing mass shows the inverse behaviour (see Figure 6.1(d)). The smearing was assumed to be independent of p_x and p_y in this simulation, and hence ϕ. It is the constancy of the reconstructed momentum or missing mass that reflects this aspect in the Figures 6.1(c) and (d) as red points. However, the measured quantities differ from the true values; the final state momentum value is higher, whereas the missing mass is lower than the true one, p_f^{true} and m_x^{true}.

If only the transverse momenta are smeared, but with different Gaussian widths, e.g., $(\sigma_x, \sigma_y, \sigma_z) = (10, 20, 0)\,\mathrm{MeV/c}$, the reconstructed momentum will have the opposite dependence on $\cos\vartheta$. This is indicated by blue arrows in Figure 6.1(a) as smearing of the transverse momentum and shown by the blue crosses in Figure 6.1(b). The final state momentum p_f decreases for $\cos\vartheta \approx \pm1$ and increases for $\cos\vartheta \approx 0$. Additionally, different resolutions in p_x and p_y introduce a dependence on ϕ, too, leading to oscillations[3] in both, the reconstructed final state momentum p_f^{rec} and the missing mass m_x^{rec} in the plots of Figures 6.1(c) and (e). The amplitude and the phase of these oscillations depend on the ratio σ_x/σ_y.

In reality, all three momentum components are reconstructed with finite and generally different resolutions so the effects described above will be superimposed. The outcome will be dominated by the component having the worst resolution, typically p_z for fixed target experiments. Casually speaking, the perfect isotropic sphere transforms into the shape of an oval "American Football" in p_z with an oscillation in p_x and p_y. However, it is still symmetric in $\cos\vartheta$ and ϕ, i.e., in p_x, p_y, and p_z. The COSY-ANKE analysis takes advantage of this symmetry requirement for verifying as well as improving the momentum calibration discussed in Section 6.3.

These kinematic resolution effects have to be taken into account for determination of the η meson mass. If not, the value extracted for m_η will depend on the production angle. The analysis of the current ANKE experiment showed differences in m_η of up to $0.5\,\mathrm{MeV/c^2}$ between $\cos\vartheta = \pm1$ and $\cos\vartheta = 0$ without correction. The angular distribution of the $\mathrm{d\,p} \to {}^3\mathrm{He}\,\eta$ reaction could slightly modify the effects of the resolution. But even this is of little consequence for the determination of m_η, because the angular distribution is linear in $\cos\vartheta$ all over the Q-range studied [M$^+$07a, Mer07]. The linearity does not influence the symmetry in $\cos\vartheta$ shown in Figure 6.1(b).

Nevertheless, the angular distribution was implemented in Monte Carlo simulations in order to avoid an additional systematic uncertainty. It was seen in the analysis that the impact on the final η mass value is completely negligible, i.e., below $1\,\mathrm{keV/c^2}$, in contrast to other contributions.

[3] This can be illustrated by plotting the p_y versus p_x component for small $|\cos\vartheta|$, e.g., $|\cos\vartheta| < 0.1$, considering different resolutions for both.

6.1.2. Deviation of reconstructed final state momentum

For η mass determination it is important to take into account that the average of the reconstructed final state momentum over all $\cos\vartheta$ and ϕ is shifted to a higher value compared to the true one. As explained above and indicated in Figure 6.1 this is a result of resolution effects. The black horizontal line in Figure 6.1(c) stands for the kinematically correct value, whereas the measured p_f one is calculated as average of all red points or blue cross. According, to the mathematical construction, the missing mass is shifted to a lower value (see Figure 6.1(e)).
So a precise determination of the resolutions in (p_x, p_y, p_z) is absolutely essential for correcting the measured kinematic variables by Monte Carlo simulations. The resolution quantities were fixed by making use of the $p_f = p_f(\cos\vartheta)$ and the $p_f = p_f(\phi)$ structures shown in Figure 6.1(b-c), because they are a direct consequence of these.

The momentum smearing was implemented into Monte Carlo simulations by smearing the three momentum components in the laboratory system by Gaussian distributions with different width $(\sigma_x, \sigma_y, \sigma_z)$. The individual momentum spreads were determined for each of the twelve energies, separately. The explicit method for their determination will be discussed in more detail in Section 6.4.1.
However, an average momentum resolution was calculated for ANKE from all twelve energies above threshold. But this is just valid for ^{3}He nuclei with laboratory momentum in the range from $2.63 - 2.68\,\mathrm{GeV/c}$. The mean momentum spreads in the laboratory frame were found to be $(\sigma_x, \sigma_y, \sigma_z) = (2.8, 7.9, 16.4)\,\mathrm{MeV/c}$. As expected for a fixed target experiment, the absolute resolution in p_z is the poorest by far. Furthermore, the p_x resolution is better than that for p_y because of the particular construction of the wire chambers and the fact that the spectrometer works in the xz-plane, exclusively.

Figure 6.2 shows the deviation, i.e., the required correction, of the measured momentum from the original one, when implementing the average smearing in Monte Carlo simulations. A beam momentum binning of $1\,\mathrm{MeV/c}$ and the PDG estimation for the η mass were used in this simulation.
It should be noted that the η mass value assumed in simulation has only very small impact on the correction parameters. Consequently, the final outcome of the COSY-ANKE experiment is nearly independent of the mass used in simulations. The systematic uncertainty introduced by this is negligible in comparison to other contributions (see Section 7).

The deviation is plotted versus the kinematically correct value. It is about $2.5\,\mathrm{MeV/c}$ for the lowest excess energy of $Q \approx 1\,\mathrm{MeV}$, decreasing with p_f to $0.7\,\mathrm{MeV/c}$ for the highest one of $Q \approx 10\,\mathrm{MeV}$ steadily. If the resolution factors σ_i are mainly independent of the beam momentum, the correction will vary like $\sim 1/p_f$. Such a

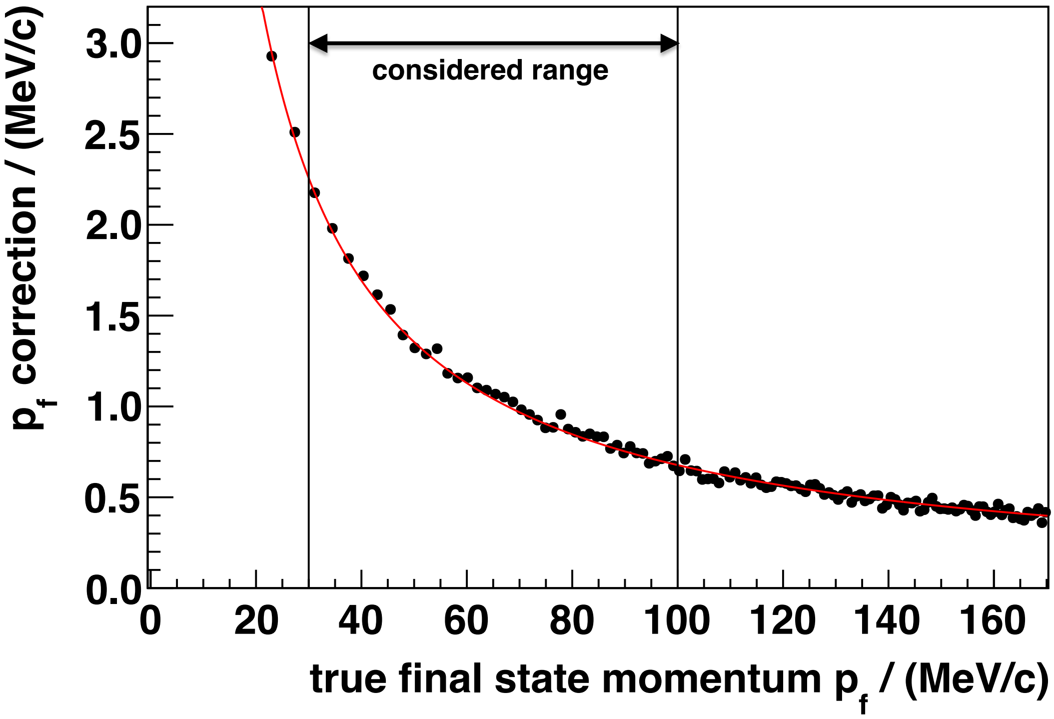

Figure 6.2.: Deviation of the reconstructed final state momentum from the true one due to resolution effects. The deviation was evaluated by Monte Carlo simulations using the average resolution of ANKE for ^{3}He nuclei in a laboratory momentum range from $2.63 - 2.68$ GeV/c. The resolution was implemented by smearing the three components with Gaussian distributions with different width $(\sigma_x, \sigma_y, \sigma_z) = (2.8, 7.9, 16.4)$ MeV/c. The deviation is shown for an 1 MeV/c beam momentum binning using the PDG estimation for η mass.

behaviour arises for this correction because it depends on the ratio of the ANKE momentum resolution to the size of the momentum sphere. Confirmation of such a dependence is offered by the red curve, which is a $1/p_f$ fit to the data.

It is essential for an accurate determination of final state momenta and consequently for the production threshold to compensate for the resolution effects at the ANKE detector. Without this correction the p_f values would be adopted too high, so that the resulting value for the η mass would be reduced, consequently (see Section 3.2). This would lead to a lower η mass value by about 150 keV/c^2 for the presented COSY-ANKE data set - a certainly wrong result.

6.2. Identification of the reaction $\mathrm{d\,p} \to {}^3\mathrm{He}\,\eta$

The kind and amount of particles produced in $d\,p$ scattering experiments depend on luminosity, total CM energy, and cross sections of the possible various reactions. So, the $\mathrm{d\,p} \to {}^3\mathrm{He}\,\eta$ reaction would be completely overshadowed by the proton background without a powerful event selection[4] because cross sections for mostly simple processes where deuterons, protons, and neutrons are produced[5] exceed those ones for fusion to helium.

The first step in the event selection was the usage of a dedicated online hardware trigger for $^3\mathrm{He}$ nuclei via the energy loss during the beam time as described in Section 4.3.3. Although the trigger reduces the proton and deuteron background as well as the dead time effectively, the background reactions cover the signal of $\mathrm{d\,p} \to {}^3\mathrm{He}\,\eta$ in almost all spectra completely. It is neither in the missing mass, nor in the final state momentum spectrum that a $^3\mathrm{He}\,\eta$ signal is visible.

The background was reduced even further by using cuts on the two-dimensional energy loss versus momentum spectra ($\Delta E/p$) and by cuts on those for path length in the offline analysis, explained in Section 6.2.3. Therefore a precise momentum reconstruction is necessary for registered particles. It is clear that this requires a careful momentum calibration of the ANKE detector, accomplished in a two step process. The standard Fd system calibration, presented in the next Section 6.2.1, was verified and improved by a following fine calibration parameter tuning. The next two sections will emphasises the momentum reconstruction at ANKE and the standard Fd system momentum calibration.

6.2.1. Methods for momentum reconstruction at ANKE

The track and momentum reconstruction phases are separated in the ANKE software. Firstly, straight tracks are formed by the hit positions of particles impinging on the tracking detectors, i.e., the drift chamber and the two MWPCs. Secondly, with the knowledge of the magnetic field of the D2 spectrometer magnet in addition, their three-momenta are reconstructed at the vertex production point.

The ANKE software provides three different methods for momentum reconstruction of the Fd system [Dym01, D$^+$04]:

---

[4] For example: There are more than 10^4 protons produced from the $\mathrm{d\,p}$ elastic scattering at each $^3\mathrm{He}$ nuclei from the $\mathrm{d\,p} \to {}^3\mathrm{He}\,\eta$ reaction, because the total cross section of the $\mathrm{d\,p} \to {}^3\mathrm{He}\,\eta$ reaction amounts to $\sigma \approx 400\,\mathrm{nb}$ [M$^+$07a], as discussed in Section 3.2.1, whereas that one for the $d\,p$ elastic scattering is $\sigma \approx 10\,\mathrm{mb}$ [KSTY85] at a deuteron beam momentum range from $2.0 - 3.7\,\mathrm{GeV/c}$.

[5] For example: The $\mathrm{d\,p}$ elastic scattering or the deuteron breakup.

1. "Box field" method [Mer03]
2. "Polynomial approximation" by transforming straight line track parameters on the D2 forward exit window into the three-momentum at the interaction point
3. "Runge-Kutta-Nyström tracing" by fitting the experimental hits

All three methods make use of the same track finding algorithm. It reconstructs a straight track between the drift, the wire chambers, and the hodoscope layers from the hits in the tracking detectors.

The box-field approach is the fastest reconstruction method but the obtained results for the momenta show larger deviations in comparison to the other two methods. This is why this specific method was not used in the analysis and will not be discussed in the following. The polynomial approximation method is faster than the Runge-Kutta-Nyström tracing, but not as accurate, because it depends on a larger number of parameters. These ones have to be generated by simulations introducing potential sources for inaccuracies. The Runge-Kutta-Nyström tracing has the advantage of not being dependent on simulations, that is why it was used for the standard Fd system calibration as well as for the fine tuning of the calibration parameters exploiting the kinematics of the $\mathrm{d\,p} \to {}^{3}\mathrm{He}\,\eta$ reaction. The Runge-Kutta-Nyström tracing will be presented in the following, whereas that one for the polynomial approximation method is summarised in the appendix in Section A.2.

Particle trajectories are commonly characterised by a finite number of track parameters. One example for such a parameter is the three-momentum vector. The track parameter propagation is the process of transporting back track parameters through the magnetic field and material of the detector to the initial production point. It is a basic part of any track- and momentum reconstruction algorithm for physical quantities. In particle physics experiments the Runge-Kutta-Nyström method is the most favourite one [MB79, BM81]. It was developed to solve second-order differential equations, such as the equation of motion of a particle with mass m, charge q, velocity $\vec{v}$, and momentum $\vec{p}$ in a magnetic field $\vec{B}$:

$$\frac{\partial \vec{p}}{\partial t} = q\,\vec{v} \times \vec{B}\ . \tag{6.3}$$

The basic ansatz of the Runge-Kutta-Nyström method relies on dividing the integration interval into steps and by solving the equation of motion in an iterative procedure at these different points. This is realised at ANKE by subdividing the three-dimensional magnetic field map of D2 into small cubes with constant magnetic field strength. The hit positions of a particle in the wire chambers are traced back through the magnetic field to the vertex position. This allows to determie the ratio of charge and momentum. The Runge-Kutta-Nyström method is the slowest one, but it provides the best precision for momentum reconstruction. That is why it was used for the calibration of the detector as well as for the final data analysis.

At this point it is important to note that the final η mass outcome is independent of the reconstruction method used in the analysis. This was verified by opposing the result of the polynomial approximation method to that one of the Runge-Kutta-Nyström one. The η mass values agree within their uncertainty limits as expected.

However, both methods need an accurate knowledge of the D2 magnetic field. The three-dimensional magnetic field maps for different field strengths were calculated by using the MAFIA code, which has turned out to be the most appropriate tool [SKBK01]. The theoretical calculations were experimentally verified. For this a field-mapping machine from GSI was in use. Thus, the combination of theoretical calculations and experimental measurements provides accurate three-dimensional magnetic field maps of the spectrometric D2 magnet, which allow a precise momentum reconstruction. The results obtained by the floating wire technique gave the necessary confidence in the correctness of the momentum reconstruction procedure [SKBK01].

6.2.2. Standard momentum calibration of the forward detector

A precise momentum reconstruction of detected particles at ANKE depends equally on various parameters due to its moveable construction as indicated in Section 4.3. These are magnetic field strength of the spectrometric D2 magnet, deflection angle of the beam, position of the interaction point, and locations of the tracking detectors, i.e., the drift and wire chambers.

The standard momentum calibration procedure [Dym09] was developed and carried out by S. Dymov. The positions of drift and wire chambers on the moveable platform are aligned at first by using data taken at the beginning of the beam time at a deflection angle of 0° and no magnetic field in D2. Doing this the ejectiles move on straight tracks starting from the nominal interaction point in the overlap region of the COSY beam and the cluster-jet target. An analysis of these tracks makes it possible to determine the positions of the Fd chambers relative to the D2 magnet as well as the target position. These parameters are well known by direct measurement, but it is by this analysis, one can increase their precision.

After having made this first alignment the global positions of drift and wire chambers are defined by their location on the moveable Fd system platform. Although the positions of the platform and interaction vertex are already known by direct measurements, a much more precise determination of their values was possible by investigating a series of reference reactions at all the twelve energies. These reactions are:

1. Small angle $\mathrm{d\,p} \to \mathrm{d\,p}$ elastic scattering with the fast forward deuteron being detected
2. Large angle $\mathrm{d\,p} \to \mathrm{d\,p}$ elastic scattering with both final state particles being detected
3. $\mathrm{d\,p} \to \mathrm{p\,p\,n}$ charge-exchange with two fast protons being detected
4. $\mathrm{d\,p} \to {}^3\mathrm{He}\,\pi^0$ with the ${}^3\mathrm{He}$ nucleus being detected

In a first iteration the analysis examined an event sample of about 1000 events for each energy. This was increased to 10000 for the second iteration in order to confirm the obtained results for vertex and Fd system platform positions. Deuteron-proton elastic scattering in the backward hemisphere allows to verify energy momentum conservation in the reconstructed four momenta. For the other reactions, the minimisation of the deviation of the missing mass from the expected PDG value was used to adjust the positions of the interaction vertex and the Fd system platform.

Figure 6.3 shows the missing mass deviation from the PDG neutron mass estimation at a beam momentum of $p_d = 3146\,\mathrm{MeV/c}$ as one specific example. The missing mass was calculated for two detected protons from deuteron breakup. In this case the signal is almost background free because of the clear signature of the two protons in the Fd system.
A Gaussian with a straight line background was used in order to describe the missing mass signal for all four reactions. The Gaussian mean values defines the deviation from the expected value. Thereby the missing mass deviates by $(0.9 \pm 0.2)\,\mathrm{MeV/c^2}$ only from the PDG neutron mass for this energy, but the discrepancy increases up to $3\,\mathrm{MeV/c^2}$ for higher energies.

The missing masses for all four channels were reconstructed to an accuracy of $\approx 3\,\mathrm{MeV/c^2}$ when using the determined calibration parameters after optimisation. Although reaching a good quality, it is manifestly insufficient for a competitive determination of the η mass. Therefore, a more refined technique was needed for fine tuning calibration parameters, explained in Sections 6.1 and discussed in 6.3.

The classical calibration method, i.e., the study of kinematic variables in measured reactions with known masses, is standard for magnetic spectrometers. That is why it was used at the other η missing mass experiments [P+92, AB+05] in such a similar manner to such an extent. In contrast to those experiments having forward and backward acceptance, only, the ANKE facility has full geometrical acceptance for the $\mathrm{d\,p} \to {}^3\mathrm{He}\,\eta$ reaction up to an excess energy $Q \approx 15\,\mathrm{MeV}$. For this case the standard calibration could be improved significantly by studying the dependence

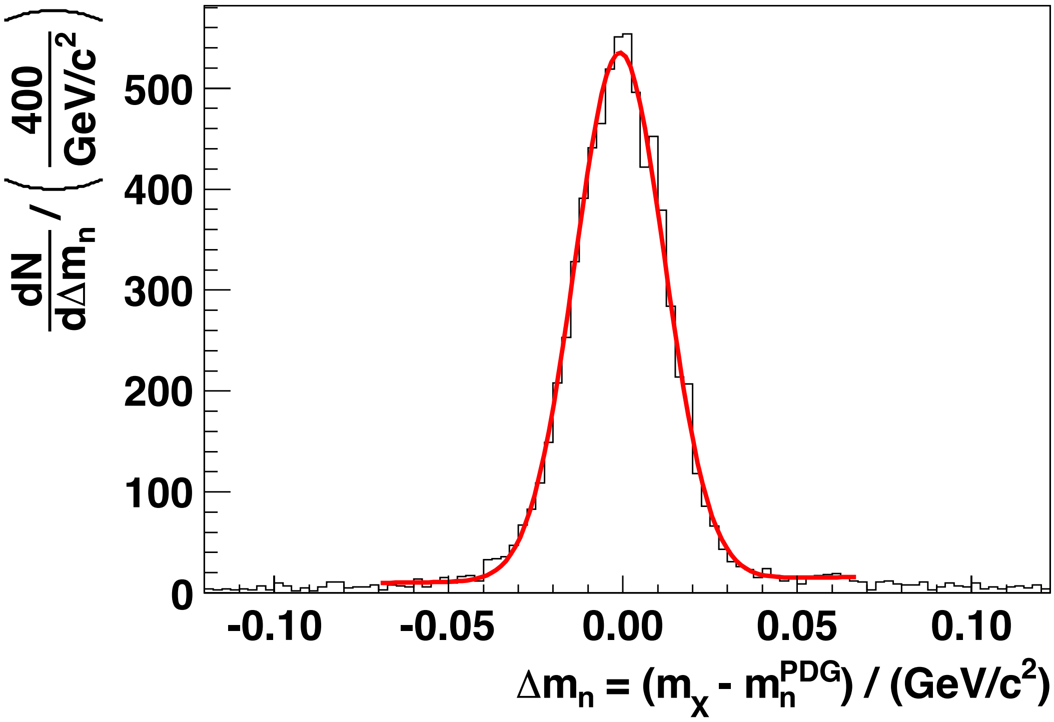

Figure 6.3.: Deviation from the PDG neutron mass for the missing mass of two detected protons in the Fd system. Data for a beam momentum of $p_d = 3146\,\mathrm{MeV/c}$ is shown.

of the final state momentum on the ${}^3\mathrm{He}$ CM angles. The calibration fine tuning requires a clean separation of the ${}^3\mathrm{He}\,\eta$ signal from the background and this was the first step of the analysis, discussed in the next section.

6.2.3. Event selection

The identification of the $\mathrm{d\,p} \to {}^3\mathrm{He}\,\eta$ reaction was achieved by a two step event selection, consisting of an online part during the beam time and an offline part when analysing the data afterwards.
In the first step, the online hardware trigger adjusted for ${}^3\mathrm{He}$ particle selection cut back the largest amount of proton and deuteron events during the process of data taking. It is explained in detail in Section 4.3.3.
In the second step, that means in the offline analysis, the raw background was suppressed even further by cuts on the energy loss and path length of charged particles in the Fd system. The raw background consists mainly of protons from deuteron breakup.

Energy loss versus momentum cut

The signals of the Fd system scintillation hodoscope allow for separating the different particle species because they are directly proportional to the particle energy loss in a medium. The Fd hodoscope needed to be calibrated in order to calculate the correct energy loss from the voltage signals of the photomultipliers, which are caused by the scintillation light of the counters. It is because of the technical realisation, e.g., different amplification, discriminator thresholds and other parameters, that the voltage signals differ from counter to counter. The Fd system hodoscope was calibrated in the scope of a Bachelor thesis by comparing the counter voltage signals to the output of Geant4 simulations [Fri11].

When moving through matter or an absorber, relativistic charged heavy particles loss primarily energy by ionisation. The energy loss per distance travelled $-dE/dx$ is well-described by the Bethe-Bloch equation (see for example [N^{+}10]) :

$$-\frac{dE}{dx} = K\frac{z^2}{\beta^2}\frac{Z}{A}\left(\frac{1}{2}\ln\frac{2m_ec^2\beta^2\gamma^2T_{\max}}{I^2} - \beta^2 - \frac{\delta(\beta\gamma)}{2}\right) \, . \tag{6.4}$$

The contribution of the absorber material to the energy loss is specified by the ratio of proton and nucleon number Z/A, the mean excitation energy I, the density effect correction δ, and the constant factor $K = 4\pi N_A r_e^2 m_e c^2$ with Avogardo constant N_A. It is of great importance for particle separation, that the energy loss of the penetrating particle is directly proportional to the square of the charge z and inversely proportional to the square of its relativistic velocity $\beta = v/c$:

$$-\frac{dE}{dx} \sim \frac{z^2}{\beta^2} \, . \tag{6.5}$$

The mass of the penetrating particle is also taken into account by the maximum kinetic energy $T_{\max}$ which can be transferred in a single collision to a free electron. According to Equation (6.5) the energy loss ΔE is high for low particle momenta, i.e., velocities, decreasing with growing momentum up to the region of minimal ionising particles. That is why each particle species populates its characteristic band in the $\Delta E/p$ spectrum, depending to the first order on the particle's charge and secondly on its mass. In contrast to single charged protons and deuterons the double charged ^{3}He particles deposit more energy in the scintillation counters, travelling through them.

Figure 6.4 shows the two-dimensional distributions of energy loss in the forward scintillation hodoscope versus the particle laboratory momentum for simulations of the reaction $\mathrm{d\,p} \to {}^3\mathrm{He}\,\eta$ (left row) and data (right row). The upper column stands for one typical counter of the 1$^{\text{st}}$ layer (6$^{\text{th}}$ counter) and the lower column for one of the 3rd layer (4th counter). The energy loss of ^{3}He particles in the 1st layer ($\approx$ 27 MeV) is a factor of two higher in comparison to that one in the 3rd layer ($\approx$ 14 MeV). It is because the counter thickness in the 1st layer is twice the thickness from the 3rd one. When simulating solely the two body reaction $\mathrm{d\,p} \rightarrow {}^3\mathrm{He}\,\eta$, then the ^{3}He nuclei populate only a narrow momentum range from $2.5 - 2.8$ GeV/c in the $\Delta E/p$ spectrum. Analysing data shows a clear ^{3}He nuclei band with an inhomogenous event distribution. The appearing structures there can be assigned to various contributions from the π^0, $(\pi\pi)^0$, and η production. The three pion production contributes to the band, too, but can not be clearly identified because of its low cross section and small geometrical acceptance at ANKE.

A cut on the ^{3}He nuclei was already applied in the $\Delta E/p$ spectra. It was adjusted on the basis of the $\Delta E \times \beta^2/p$ spectrum, depicted on the left hand side in Figure 6.5. The decreasing $\Delta E/p$ band was transformed into a nearly constant line over a wide momentum range by multiplying the energy loss with the square of the particle's velocity β. A projection of this two-dimensional distribution onto the ordinate gives a clear peak with a low background, shown in the right hand side of Figure 6.5. A very loose cut at a $6\,\sigma$ level was used in the analysis, but changing this to $3\,\sigma$ has only a tiny effect on the value obtained for the η mass as will be discussed in Section 7.

Path length cut

A further reduction of the background was achieved by exploiting timing signals of the Fd scintillation hodoscope to determine the time of flight and also path length of the tracks reconstructed with the ANKE Software. Therefore, only events were taken into account with exactly three hits in the scintillation hodoscope, i.e., exactly one hit in each layer. Most of these hits were caused by ^{3}He nuclei of η, single, or multi pion production and a track and momentum was reconstructed. Nevertheless, background events from proton and deuteron reactions pass the hardware trigger as well as the three hit restriction, too, contributing to the background.

The validity of a track can be verified by its path length, calculated from the time of flight signal. Therefore, the time of flight difference t_{diff} between the hit in the 3rd layer and an average timing value of hits in the 1st and 2nd layer was calculated for each event. The average timing value was used in order to increase the resolution of the timing signals, which was possible because of the short distance between 1st and 2nd layer. It is important to note that the timing signals of the 1st and 2nd layers are reconstructed by track information, whereas the timing of the 3rd one is not assigned to a track.
The path length $s = \beta t_{\mathrm{diff}}$ was determined for hits of each counter in the 3rd layer, by multiplying the particle's relativistic velocity with the timing difference. The

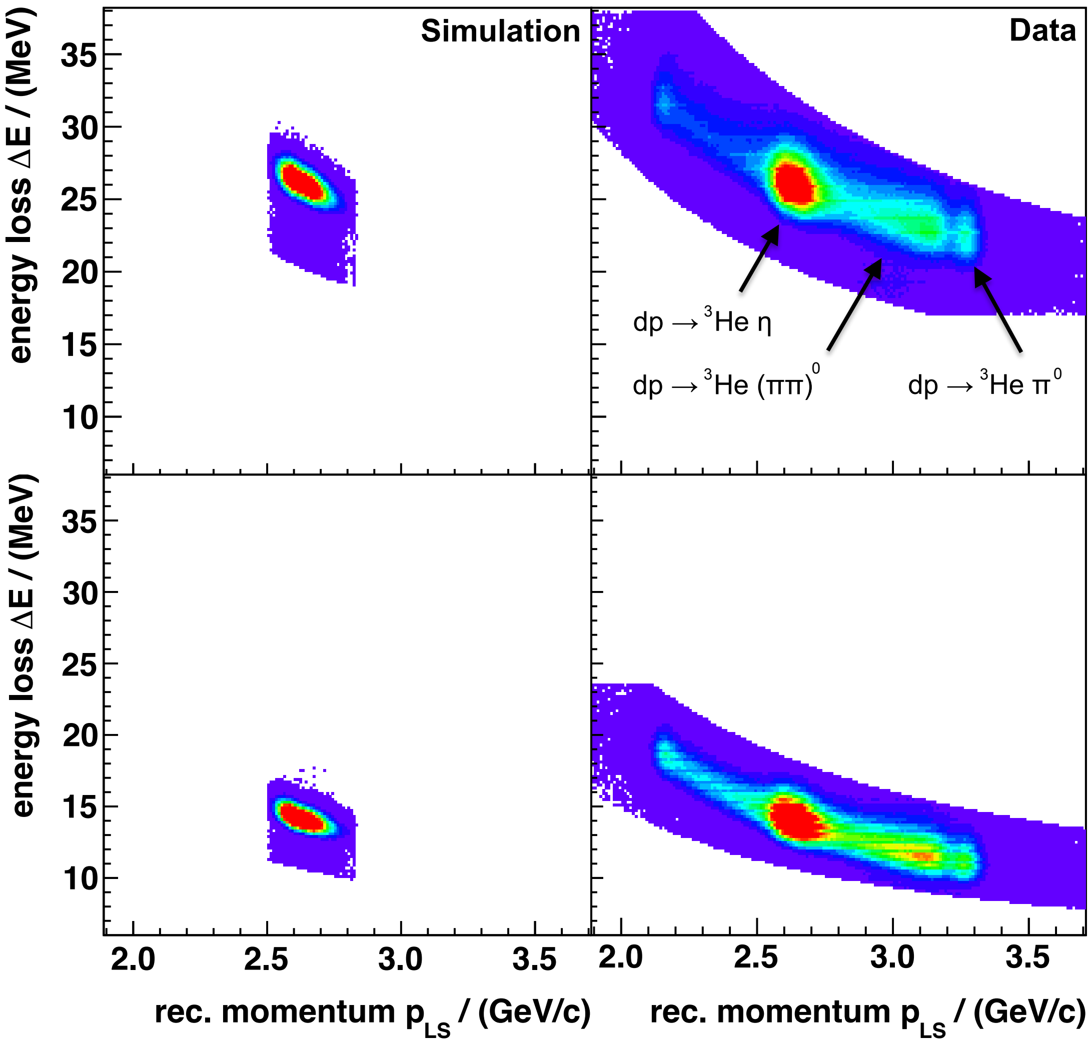

Figure 6.4.: The two-dimensional distributions of energy loss in the forward scintillation hodoscope versus the particles' laboratory momentum is depicted for simulations of the reaction $\mathrm{d\,p} \to {}^3\mathrm{He}\,\eta$ (left row) and data (right row). While the upper column displays the $\Delta E/p$ spectra for event hits in the 6^{th} counter of the 1^{st} layer, the lower one shows the spectra for the 4^{th} counter of the 3^{rd} layer (Pd sidewall), in which for both a $3\,\sigma$ cut is applied on the ^{3}He signal in the $\Delta E \times \beta^2$ spectra (see text). In data a clear ^{3}He band becomes visible consisting of the single-, two-pion, and η production.

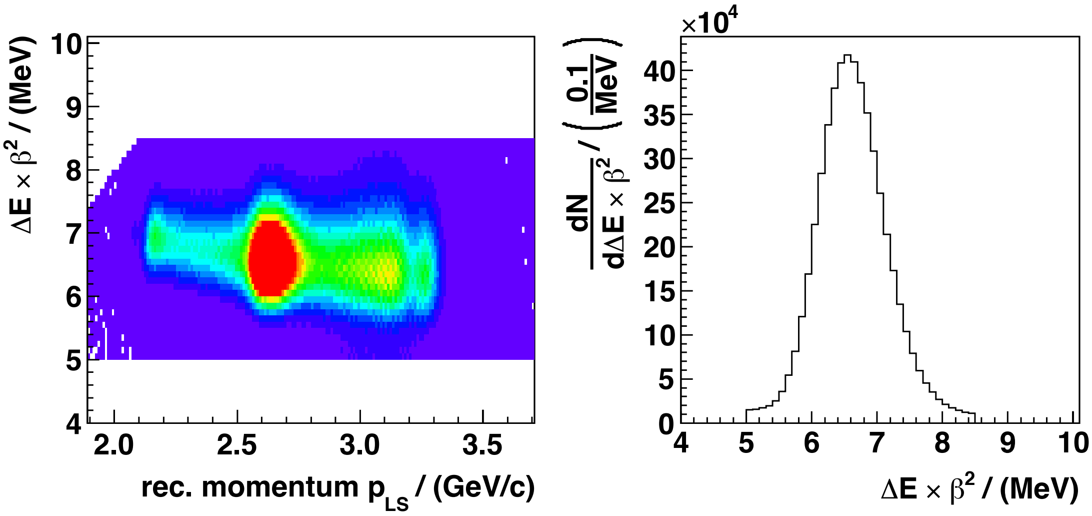

Figure 6.5.: Two-dimensional distribution of energy loss times the square of the particle velocity versus its laboratory momentum (left-hand side). The energy loss cut on ^{3}He was adjusted by projecting this distribution onto the y-axis giving a peak with little background (right hand side). Data within a $\pm 6\,\sigma$ cut were retained for further analysis.

particle's relativistic velocity was calculated by energy and momentum $\beta = p/E$ of the reconstructed track, assuming the mass and charge of ^{3}He nuclei. The path length distribution determined for the 4$^{\text{th}}$ counter of the 3$^{\text{rd}}$ layer is shown in Figure 6.6 as one typical example. The path length has arbitrary units because the timing signals of the Fd scintillation hodoscope were not calibrated.

However, a two peak structure is visible in the path length spectrum consisting of a narrow peak at short path lengths and a much broader one at larger ones. The peak at small flight length belongs mostly to ^{3}He particles, whereas the distribution at larger path length is caused by events, for that the 3$^{\text{rd}}$ layer's counter timing is not connected with the reconstructed track. This distribution appears in a similar manner for all six counters of the 3$^{\text{rd}}$ layer. The population of the large path length peak increases for counters close to beam pipe, because they are exposed to a much larger particle flux building up such background events[6]. Exclusively, events within a $3\,\sigma$ level were taken into account for the final analysis in order to reduce the background further. The influence of this cut on the final η mass outcome was estimated by varying the σ range as will be discussed in Section 7. A reduction to $2\,\sigma$ showed in comparison to other contributions a negligible impact, only.

[6] The particle flux impinging on the Fd system increases close to the beam pipe because of protons from the deuteron breakup.

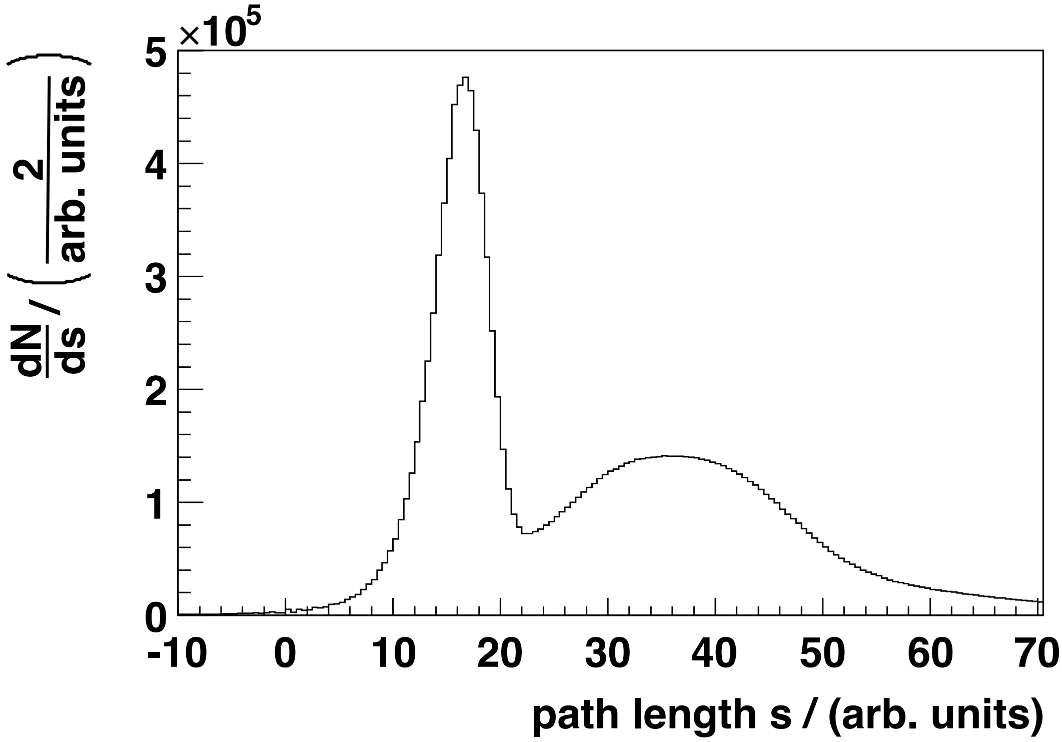

Figure 6.6.: The path length spectrum shows a peak at small path length belonging mostly to ^{3}He particles, whereas the distribution at larger path length is caused by events where the 3rd layer's counter timing is not connected to the reconstructed track. By taking only events within a $3\,\sigma$ level into account, the background is reduced.

Signal of the reaction $\mathrm{d\,p} \to {}^3\mathrm{He}\,\eta$

The background, consisting mainly of protons and deuterons was strongly reduced by the application of the two-stage event selection, i.e., the online hardware trigger as well as energy loss and path length cuts in the offline analysis. The same event selection cuts were applied for all thirteen energies measured during the beam time. The events from the $\mathrm{d\,p} \to {}^3\mathrm{He}\,X$ reactions pass the cut conditions, so the signal of the η production is not overshadowed anymore in most spectra. It becomes visible as a clear peak in the missing mass and final state momentum depicted in Figure 6.7 for two different excess energies, the lowest and highest one ($Q \approx 1\,\mathrm{MeV}, 10\,\mathrm{MeV}$), according to Table 3.2. The spectra show exclusively a narrow range for missing mass as well as final state momentum for focussing on the η production. The single and two pion production signals become visible, too, when increasing the axis range. This is already indicated in the $\Delta E/p$ spectra (see Figure 6.4) and shown more clearly in the appendix by the final state momentum histogram A.1.

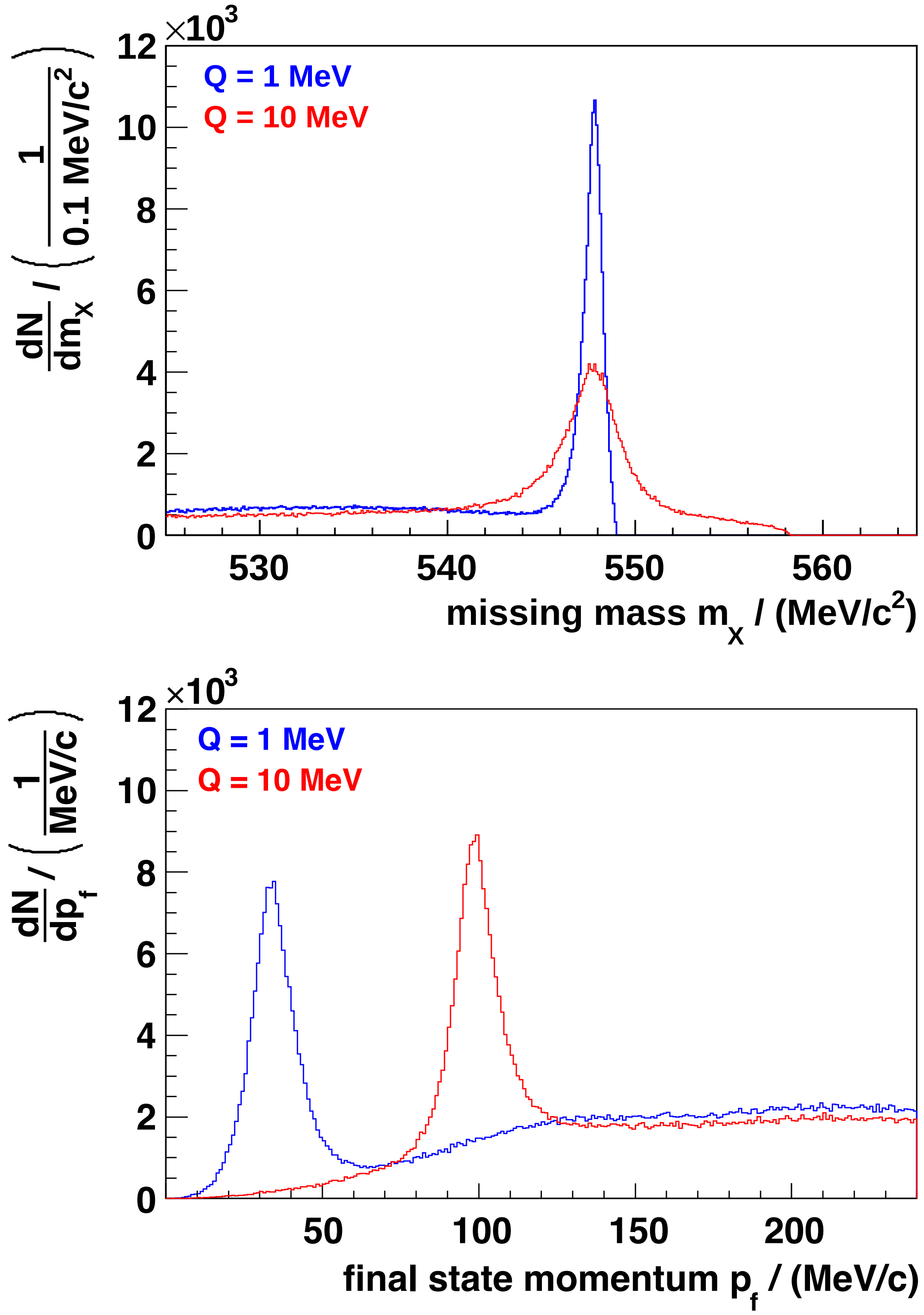

Figure 6.7.: Missing mass (upper panel) and final state momentum distributions (lower panel) of events passing the event selections cuts for data taken at the lowest (blue, $Q = 1\,\mathrm{MeV}$) and highest (red, $Q = 10\,\mathrm{MeV}$) excess energy. A clear peak of the $d\,p \to {}^3He\,\eta$ reaction is visible in both spectra, respectively. Although the measuring time and cross sections for the two energy settings are almost the same, there is a difference in the hight of the background because of luminosity fluctuations.

For data taken at $Q = 1\,\mathrm{MeV}$ excess energy a narrow peak occurs at a missing mass of $\approx 548\,\mathrm{MeV/c^2}$ due to η production. On the right hand side of the peak there is no background signal, because the kinematical limit is at about $549\,\mathrm{MeV/c^2}$, defined by the total CM energy and adjustable by the beam momentum. The kinematical limit grows on in the missing mass when increasing excess energy. The amount of measured η mesons is nearly the same for the two energies because of an almost constant luminosity and cross section for each energy.
The final state momentum spectrum shows the rising of the η production peak to higher values when increasing the beam momentum or excess energy, respectively. The width is dominated by the momentum resolution of ANKE and remains constant.

The remaining physical background below the η peak originates mainly from some residual deuteron breakup and multi pion production in the $\mathrm{d\,p} \to {}^3\mathrm{He}\,X$ reaction, where $X = (\pi\pi)^0, (\pi\pi\pi)^0$, or even $X = (\pi\pi\pi\pi)^0$. At the lowest excess energy, the signal to background ratio is around 11 but this decreases with rising excess energy to ≈ 1.8 at $Q \approx 10\,\mathrm{MeV}$. The difference in the height of the background for $Q \approx 1\,\mathrm{MeV}$ and $Q \approx 10\,\mathrm{MeV}$ is caused by small luminosity fluctuations in the almost same measuring time for each energy. The shape of the multi pion background under the η peak stays nearly constant and exhibits no significant variation in the narrow excess energy range up to $10\,\mathrm{MeV}$. The background description takes advantage of this fact discussed in following Section 6.2.4.

6.2.4. Background description

The remaining physical background had to be described and subtracted in order to determine precise final state momenta of the ${}^3\mathrm{He}\,\eta$ production and to gain a deeper understanding of the peak's shape. This is feasible using different methods.
One kind is given by modelling the background spectrum by phase space Monte Carlo simulations. In this process all contributing reactions have to be taken into consideration. These are the two-, three-, and four pion production, plus a component arising from the misidentified protons from the intense deuteron breakup reaction. This method was applied at a previous analysis, investigating the total and differential cross sections of the reaction $\mathrm{d\,p} \to {}^3\mathrm{He}\,\eta$ at excess energies of $Q = 20, 40, 60\,\mathrm{MeV}$ [R$^+$09, Rau09]. The accurateness of this ansatz depends on a precise implementation of the ANKE detector in simulations for estimating its geometrical acceptance of the different reactions. A lot of simulation parameters have to be under control and might influence the quality of the background description when applying this approach.
Another way for characterising and subtracting the background is provided by exploiting data taken below the production threshold of the reaction of interest. This

subthreshold data needs to be kinematically transformed to positive excess energies for comparison with results obtained above threshold[7]. And it must be corrected for luminosity, too.

The main idea is based on the assumption that the shape of physical background remains practically unchanged in the narrow excess energy range. Therefore two requirements must be fulfilled:

1. The geometrical acceptance of the detection system needs to be almost constant for the various background reaction in the energy region examined.
2. The cross sections as well as the kinematical phase space behaviour of the background reactions should show negligible modifications only, so that the shape of the physical background do not change. This is fulfilled as long as no new dominant background reaction channel opens when increasing the CM energy. Depending on its cross section it might influence the background's shape.

The four pion production $dp \rightarrow^{3} \mathrm{He}(\pi\pi\pi\pi)^{0}$ is such a candidate in the energy range chosen in the η mass measurement. Due to the difference in the masses for charged and uncharged pions, the neutral four pion production is already present in the subthreshold data at an excess energy of $Q_{4\pi^0} \approx 3\,\mathrm{MeV}$, while the channels with two or four charged pions occur at higher energies. However, previous studies figured out that the contribution of the four pion production is negligible up to an excess energy of $Q_{\eta} = 20\,\mathrm{MeV}$ for describing background of the $\mathrm{d\,p} \rightarrow {}^{3}\mathrm{He}\,\eta$ reaction [Mer07, Rau09]. One reason therefore might be a very small cross section close to the η production threshold.

The subthreshold data was scaled according to the available phase space and luminosity ratio in order to subtract the background in final state momentum or missing mass spectra. The kinematical transformation was achieved on an event by event basis by scaling up the reconstructed subthreshold momentum in the laboratory system $\vec{p}\,^{\text{subth.}}_{\text{LS}}$ with the ratio of desired and subthreshold beam momentum $p\,^{\text{desired}}_{\text{beam}}/p\,^{\text{subth.}}_{\text{beam}}$. In this way the kinematically correct momentum $\vec{p}\,^{\text{desired}}_{\text{LS}}$ was calculated for the desired excess energy above threshold in the laboratory system:

$$\vec{p}\,^{\text{desired}}_{\text{LS}} = \frac{p\,^{\text{desired}}_{\text{beam}}}{p\,^{\text{subth.}}_{\text{beam}}} \cdot \vec{p}\,^{\text{subth.}}_{\text{beam}} \ . \tag{6.6}$$

A SATRUNE-SPES III experiment has done pioneering work by applying this background-subtraction technique in order to investigate the near ω threshold production in proton-proton collisions ($p\,p \rightarrow p\,p\,\omega$) [H+99]. For the first time this

[7] The energy, the subthreshold data should be transformed to, is denoted in the following as "desired" momentum or excess energy, when explaining Equation (6.6).

method was used at ANKE for determination of the cross section of the reaction $d\,d \to {}^4\mathrm{He}\,\eta$ by A. Wronska [W+05]. The analysis technique was used in both experiments for missing mass spectra only. T. Mersmann showed in his PhD thesis, researching the reaction $\mathrm{d\,p} \to {}^3\mathrm{He}\,\eta$, that it is equally applicable to final state momentum spectra [M+07a, Mer07].

During the η mass beam time subthreshold data were collected at an excess energy of $Q = -5.1\,\mathrm{MeV}$ in the 1st and 2nd supercycle. In addition, a measurement was also undertaken at $Q = -4.0\,\mathrm{MeV}$ in the 3rd supercycle in order to provide further systematic test of the background changes with beam momentum (see Section 4.4.2). The final state momentum distributions are shown all together in Figure 6.8. According to Equation (6.6) data was transformed kinematically from the 3rd supercycle to the excess energy value of the 1st and 2nd one for comparison. The 2nd and 3rd supercyle were corrected for luminosity and adopted to the 1st one. The three distributions, shown in red, blue and black, coincide perfectly. Their difference is consistent with zero, which is exemplarily shown in grey for the 1st and 3rd supercycle. The same perfect matches were found even when investigating the polar and azimuthal angle dependence of the background signal by subdividing it for twenty bins, each in $\cos\vartheta$ and ϕ. Due to the fact that all subthreshold data from different supercycles resulted in the same distribution, that is why it was jointly considered in the analysis, increasing the statistics by about a factor of three and providing a much smoother background description.

Figure 6.9 illustrates the background description and subtraction for the final state momentum distribution measured at a beam momentum of $p_d = 3162\,\mathrm{GeV/c}$ corresponding to an excess energy of $Q = 4.8\,\mathrm{MeV}$ (see Table 3.2). Therefore, the subthreshold data was scaled according to the available phase space and luminosity ratio as explained above. The luminosity was adapted by ratio of the histogram sums outside the η peak region of $\pm 4\,\sigma$ level. The measured data after event selection is shown as black line, the smooth background description as grey line, and the resulting background-subtracted pure $\mathrm{d\,p} \to {}^3\mathrm{He}\,\eta$ signal is shaded grey. All that remains in the difference spectra is a ${}^3\mathrm{He}\,\eta$ Gaussian like peak with a width of $\sigma \approx 8\,\mathrm{MeV/c}$ sitting on a vanishing background. The background description has same quality for all the twelve energies above threshold[8]. The peaks are quite slightly asymmetric because of different resolutions in the three momentum components.

The width is composed of various contributions as the beam momentum smearing or the intrinsic η width, but, it is dominated by the momentum resolution of the ANKE Fd system. The influences of resolution effects on the p_f distribution was be investigated in greater detail by studying the $\cos\vartheta$ and ϕ dependence of the

[8] For completeness the spectra for all twelve excess energies above threshold are shown in the appendix in Section A.4.

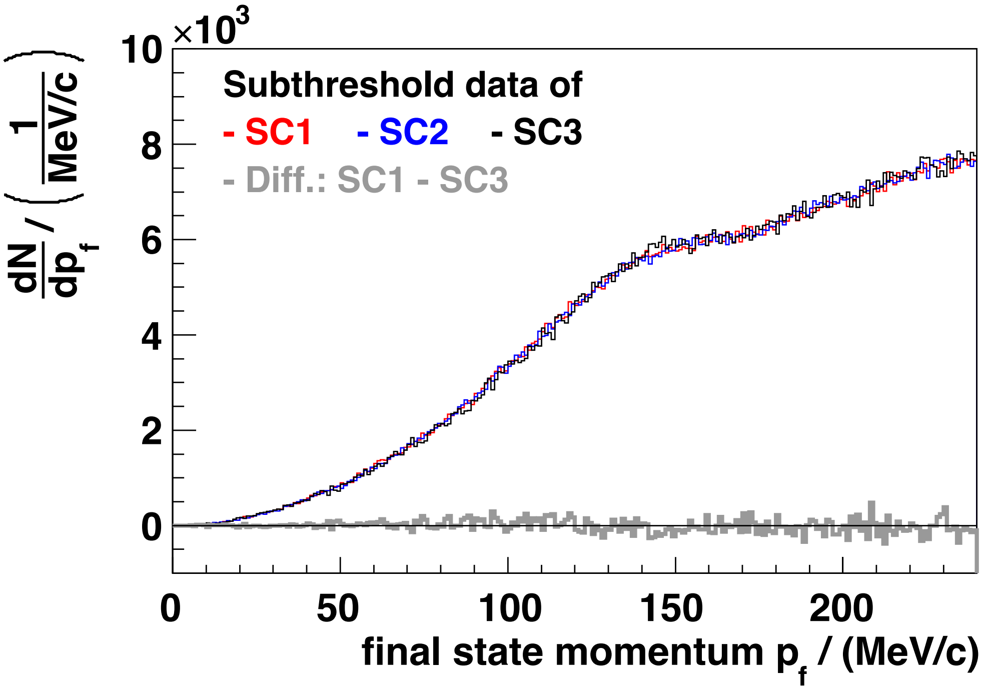

Figure 6.8.: Final state momentum background distributions shown for data taken in the 1st (red SC1), 2nd (blue SC2), and 3rd (black SC3) supercycle. For comparison they are luminosity corrected and transformed to the excess energy of the 1st and 2nd supercycle.

${}^3\mathrm{He}\,\eta$ final state momentum peak. Due to the very high statistics collected during the beam time, the distribution in p_f was investigated for twenty bins each in $\cos\vartheta$ and ϕ. This is illustrated in Figure 6.10 and 6.11, where examples of the p_f spectra summed over ϕ are shown for the lowest and highest excess energy, $Q = 1.0\,\mathrm{MeV}$ and $Q = 9.9\,\mathrm{MeV}$. Similar spectra are produced for the ϕ dependence after having integrated over ϑ.

Mean values of the ${}^3\mathrm{He}$ momentum p_f peaks as well as their widths were extracted from the background-subtracted $\mathrm{d\,p} \to {}^3\mathrm{He}\,\eta$ distributions by making Gaussian fits for the different $\cos\vartheta$ and ϕ bins. A variation of the width of 4-12 MeV/c (rms) was found, as well as a displacement of the mean value, both of which depended upon the polar and azimuthal angles. This striking effect, as mentioned above, results from the different resolutions of the ANKE Fd system in p_x, p_y, and p_z as it was explained in Section 6.1.1.

Such a careful investigation of the angular dependence of the p_f signal was indispensable for the η mass determination, because it brought two important benefits. First, the "angular dependence analysis" was used to verify and improve the stan-

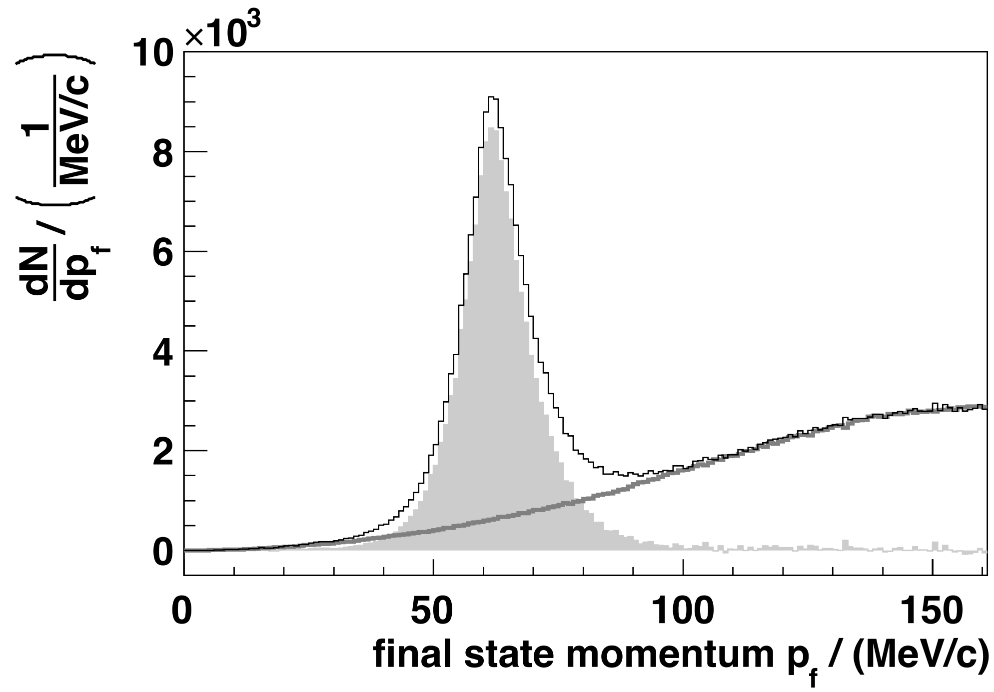

Figure 6.9.: The CM distribution of the ^{3}He momentum is shown for a beam momentum of $p_d = 3162\,\text{GeV/c}$ corresponding to an excess energy of $Q = 4.8\,\text{MeV}$. The measured data after event selection is shown as black line, the background estimated from subthreshold data as grey line, and the resulting background-subtracted $\mathrm{d\,p} \to {}^3\mathrm{He}\,\eta$ signal is shaded grey.

dard calibration by the parameter fine tuning. It exploits the symmetry requirement of the momentum sphere for the two-body reaction $\mathrm{d\,p} \to {}^3\mathrm{He}\,\eta$ as it was discussed in Section 6.1. The refined momentum calibration fine tuning will be presented in the next Section 6.3.
In the second step, resolution and smearing effects were quantified by studying the modification of the sphere provoking an anisotropy of the measured p_f signal. This allowed to calculate correction parameters for the extracted p_f in order to guarantee an accurate p_f determination (see Section 6.4).

The contribution of the background description to the final η mass error is negligible in contrast to other effects. This is because of its sturdiness and insensitivity regarding to the other analysis steps. For example, when affecting the signal to background ratio by changing the event selection parameters, this results in an η mass shift of below $5\,\text{keV/c}^2$. Even smaller, i.e., below $1\,\text{keV/c}^2$, is the influence that is caused by varying the region of a $\pm 4\,\sigma$ level chosen for fixing the scaling parameter for luminosity adaption of the subthreshold data.

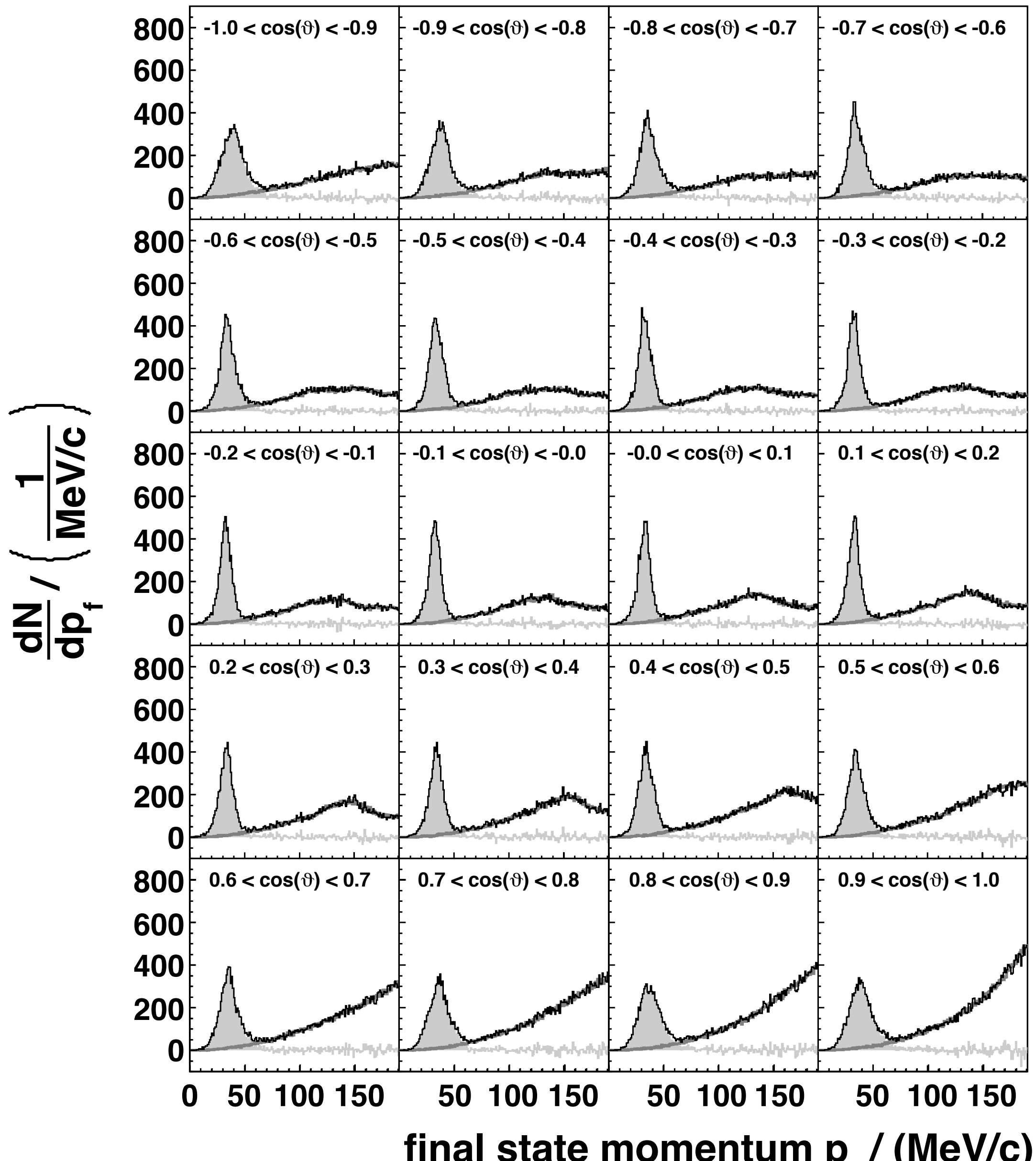

Figure 6.10.: CM distributions of the ${}^3\mathrm{He}$ momentum from the $\mathrm{d\,p} \to {}^3\mathrm{He}\,X$ reaction for twenty polar angle bins at the lowest excess energy, $Q = 1.0\,\mathrm{MeV}$. The experimental data summed over ϕ is shown by the black line and the background estimation from subthreshold data by the grey one. The resulting background subtracted $\mathrm{d\,p} \to {}^3\mathrm{He}\,\eta$ signal is shaded grey.

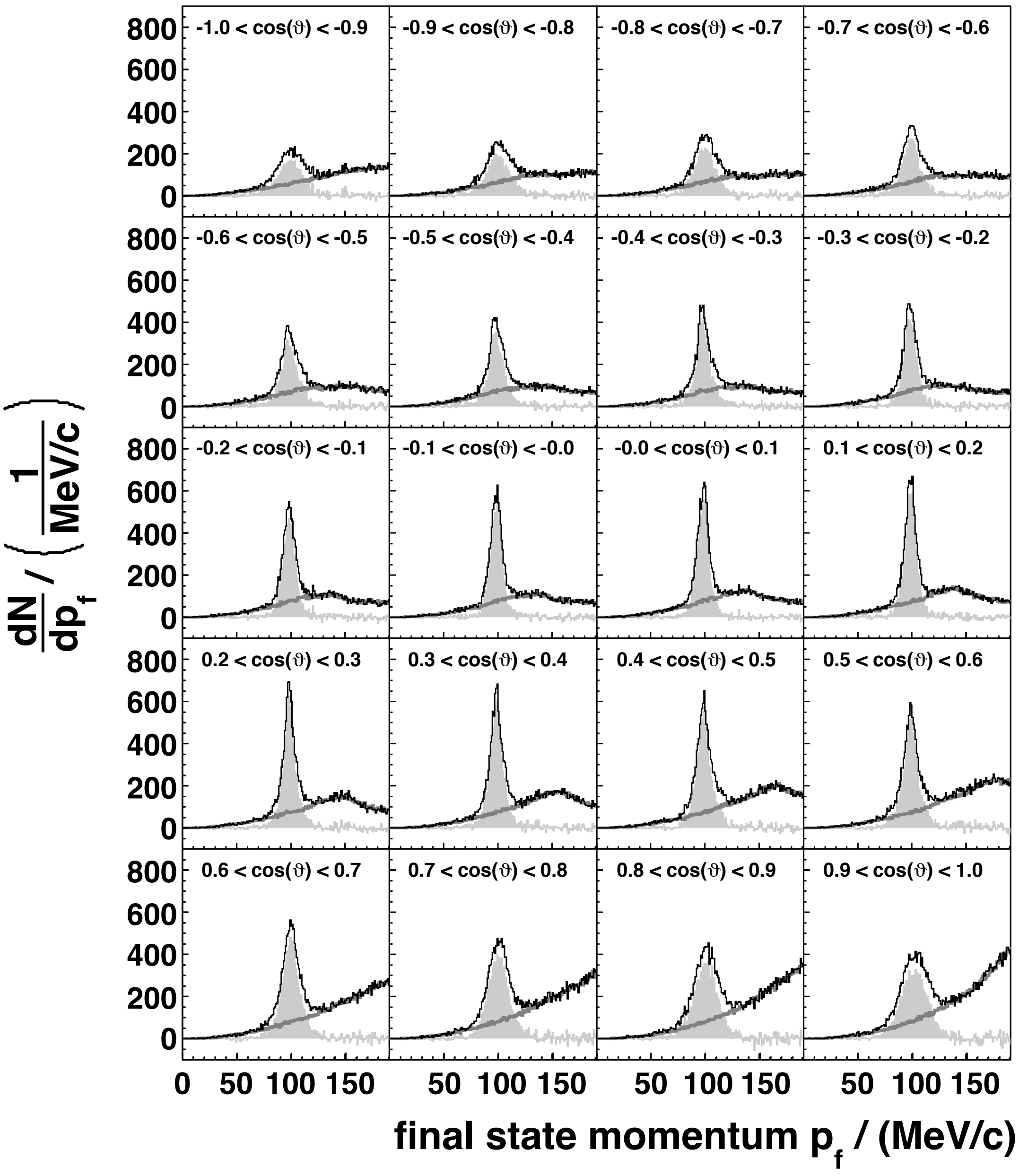

Figure 6.11.: CM distributions of the ^{3}He momentum from the $\mathrm{d\,p} \to {}^3\mathrm{He}\,X$ reaction for twenty polar angle bins at the highest excess energy, $Q = 9.9\,\mathrm{MeV}$. The experimental data summed over ϕ is shown by the black line and the background estimation from subthreshold data by the grey one. The resulting background subtracted $\mathrm{d\,p} \to {}^3\mathrm{He}\,\eta$ signal is shaded grey.

6.3. Refined momentum calibration fine tuning

The shapes of the momentum spheres were investigated for all twelve energies above threshold in order to verify and improve the standard calibration settings. The momentum spheres for data at two different excess energies, 1.5 MeV and 9.9 MeV, are visualised in Figure 6.12 as semi-circles by plotting the magnitude of the transverse momentum $p_\perp$ versus the longitudinal momentum p_z for reconstructed events. This is the same depiction as described in Section 6.1.1.

Solid lines indicate the expected mathematical kinematic loci for the two reactions $\mathrm{d\,p} \to {}^3\mathrm{He}\,\eta$ (small circle) and $d\,p \to {}^3\mathrm{He}\,\pi^0$ (large circle). The radii of the semi-circles are exactly the final state momenta associated to the available CM energy. At first glance, the semi-circles for data match with the calculated ones very well. Obviously, they are much broader because of resolution effects.
It is clear that the number of events varies along the circles due to the differential cross sections, but the method used for fine tuning calibration parameters depends exclusively on the position of a kinematic curve and not on its population. For better visualisation of the angular distribution, each event was weighted with a factor $1/p_\perp$ as it was done in previous works [Mer07]. In addition to single meson production, one can notice a large accumulation of events near the forward direction for $p_f \approx 350\,\mathrm{MeV/c}$. This corresponds to the two-pion production, $d\,p \to {}^3\mathrm{He}\,(\pi\pi)^0$ reaction.

The figure makes clear, that ANKE has full geometrical acceptance for the reaction of interest, so that the complete shape of the momentum sphere can be investigated. This was executed by studying the p_f signal as function of the polar ϑ and azimuthal angle ϕ. Figure 6.13 illustrates another representation of the momentum sphere for the low excess energy of 1.5 MeV by plotting p_f versus $\cos\vartheta$ and ϕ in a two dimensional histogram.

These illustrations hint at the structures caused by the momentum smearing effects originated by the measurement process. It turns out that the final state momentum increases for $\cos\vartheta \to \pm 1$, oscillating in the ϕ spectrum. The structures are only barely visible, so that the maxima at $\phi = \pm 180^\circ, \pm 90^\circ, 0^\circ$ cannot be clearly identified in particular; so a quantification of resolution effects is impossible. This fact emphasises the need for another representation. Figures 6.12 and 6.13, which showing the final state momentum, do not allow to draw conclusions about the quality of the calibration. They are not sensitive enough. Additionally, the p_f signal of the ${}^3\mathrm{He}\,\eta$ final state is not background free, so it could be shifted or modified.

A more accurate investigation of the p_f dependence is apparently provided by the background-subtracted $\mathrm{d\,p} \to {}^3\mathrm{He}\,\eta$ distributions for twenty individual $\cos\vartheta$ and ϕ bins (see Figures 6.10 and 6.11).

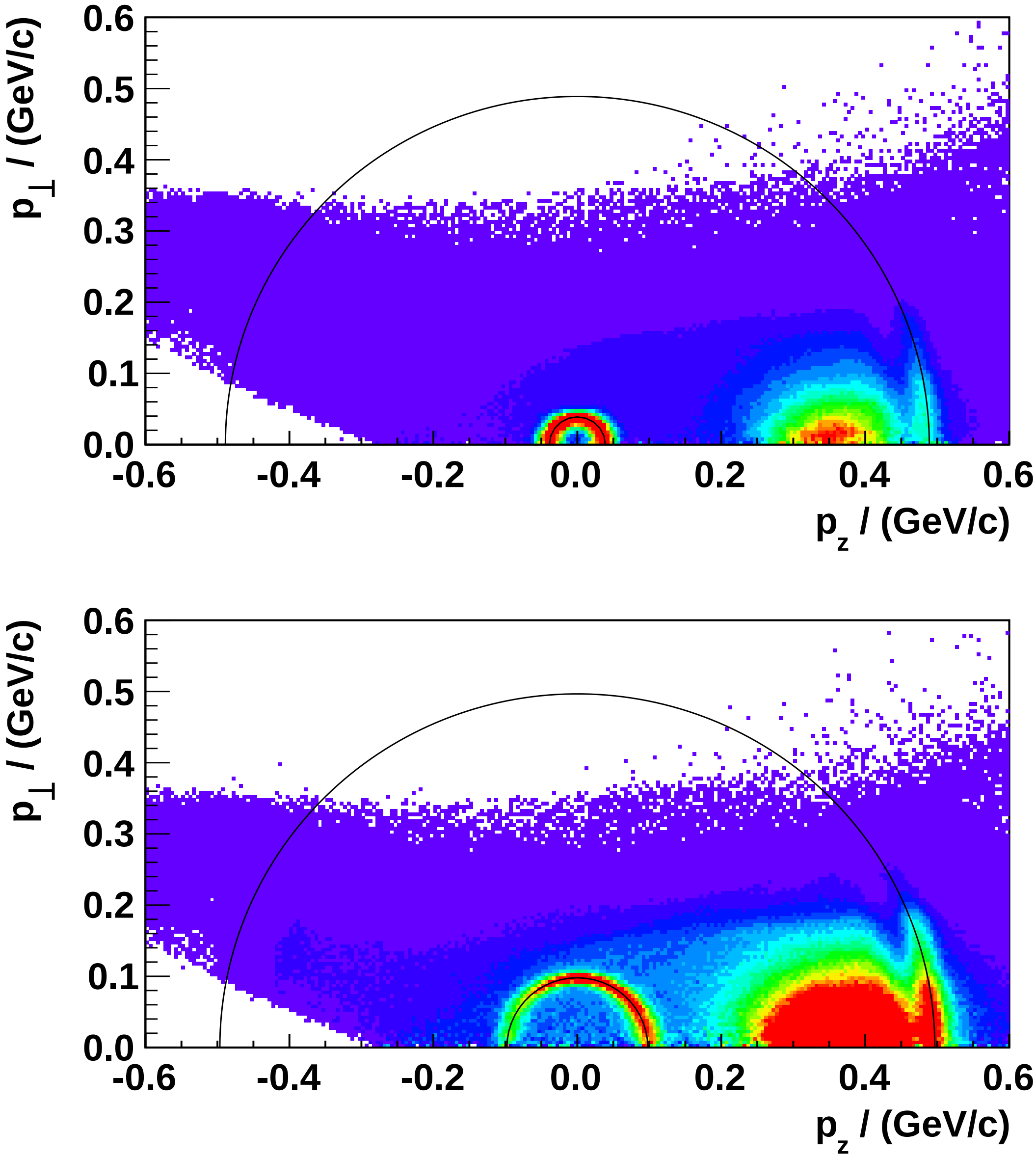

Figure 6.12.: The momentum spheres as semi-circles for 1.5 MeV (top) and 9.9 MeV (bottom) with respect to the η threshold. The magnitude of the reconstructed transverse CM momentum $p_\perp$ in the $\mathrm{d\,p} \to {}^3\mathrm{He}\,X$ reaction is plotted against the longitudinal CMcomponent p_z. For better visualisation of the angular distribution, each event is weighted with a factor $1/p_\perp$. The small and large circle indicated as solid black lines correspond to the kinematical loci for the $\mathrm{d\,p} \to {}^3\mathrm{He}\,\eta$ and $d\,p \to {}^3\mathrm{He}\,\pi^0$ reactions, respectively. ANKE covers the full solid angle for η production near threshold. In contrast, it is for single pion production only, that the forward ^{3}He nuclei are detected.

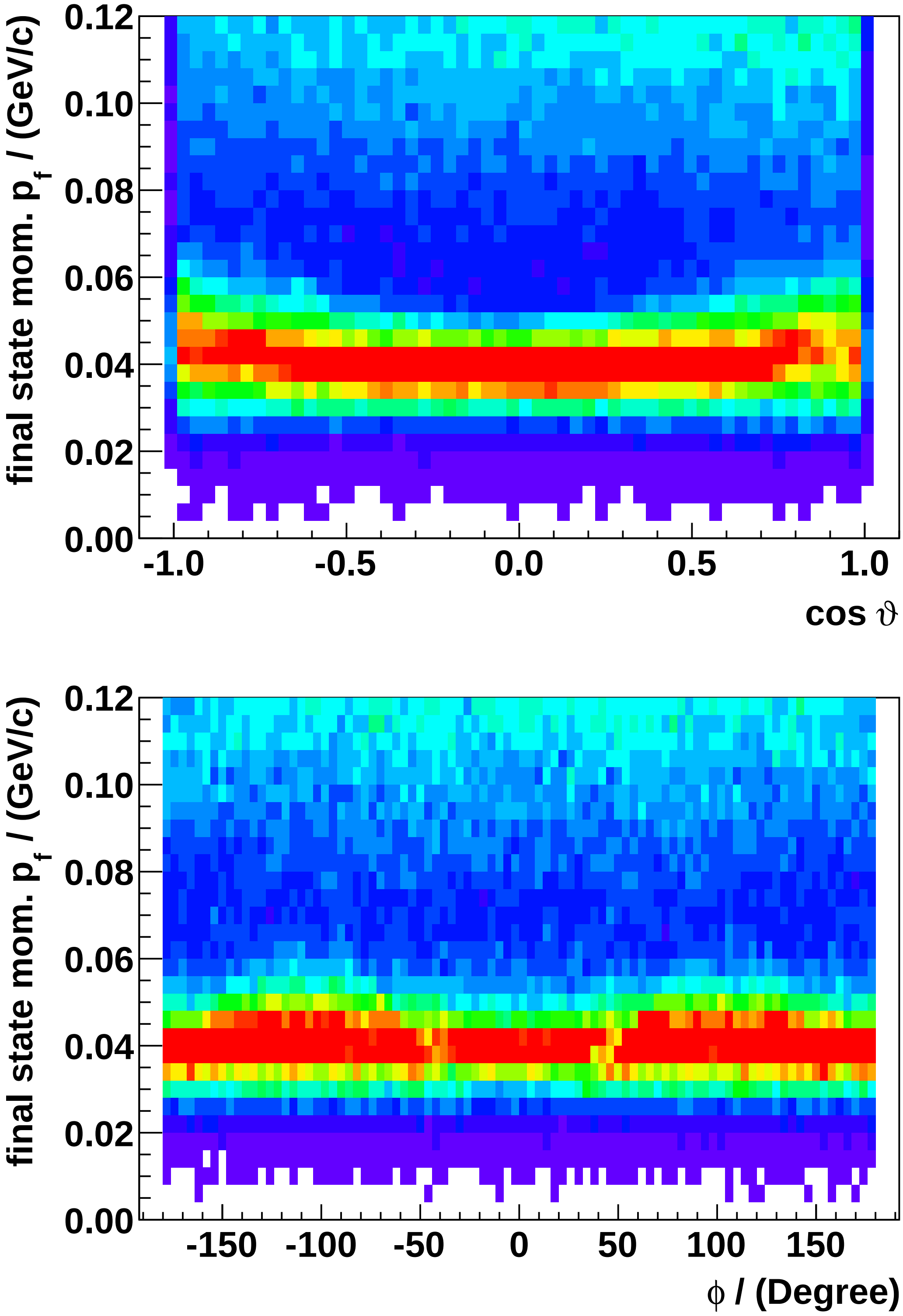

Figure 6.13.: Two-dimensional histograms for the final state momentum p_f of a event versus its $\cos\vartheta$ (top) or its ϕ angle (bottom) for an excess energy of $Q = 1.5\,\mathrm{MeV}$.

6.3.1. Fine tuning of the momentum calibration parameters

The background subtracted p_f peaks for different $\cos\vartheta$ and ϕ bins as shown in Figures 6.10 and 6.11 allow for a precise study of the momentum sphere. They were described by Gaussian fits as mentioned in Section 6.2.4, so that mean values and widths were extracted. Figure 6.14 shows mean values, i.e., the $p_f = p_f(\cos\vartheta)$ and $p_f = p_f(\phi)$ dependence, at an excess energy of $Q = 1.0\,\text{MeV}$ as one of twelve examples. The markers p_x, p_y, p_z, and $p_\perp$ indicate the momentum component, which dominates the final state momentum in the corresponding $\cos\vartheta$ and ϕ range.

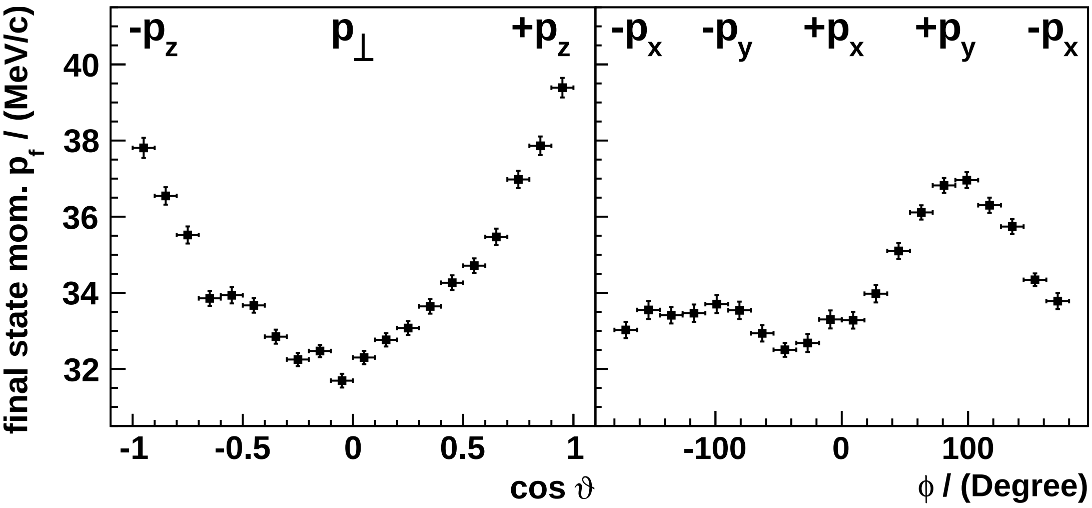

Figure 6.14.: Mean values of the twenty individual $\cos\vartheta$ and ϕ final state momentum distributions for the standard calibration at an excess energy of $Q = 1.0\,\text{MeV}$.

This depiction illustrates better than Figures 6.12 and 6.13 that the momentum sphere, represented by p_f, is neither centred nor symmetric.
The momentum sphere is shifted to higher p_z. It is on average for all twelve energies that p_f is higher for ^{3}He when produced in the forward direction ($\cos\vartheta = 1$) than in the backward ($\cos\vartheta = -1$) one. The semi-circle must be perfectly centred around zero for a perfect calibration. A shift to the left or to the right might have two different reasons. A shift in p_z could be caused by assuming a wrong beam momentum when changing from the laboratory system to the CM frame. This is highly improbable and can be excluded because the beam momenta were measured in an independent manner. The other reason might be an insufficient calibration. If, for example, one adopts a slightly different magnetic field strength of the D2 magnet, this assumption will imply a really wrong p_z reconstruction as will be shown later.

The oscillation in the ϕ spectrum is also far from being symmetric, and this is particularly evident at $\phi \approx \pm 90°$, where the p_y momentum component dominates. The p_x component fulfils the requirement for symmetry at is its best.

However, the asymmetric pattern is rather similar at all twelve energies and this stresses the need to improve the calibration for determining correct momenta. This is especially necessary because, otherwise, the deviations between the measured final state momenta and the true ones cannot be quantified.

The different calibration parameters were optimised at COSY-ANKE by studying the deformation of the momentum sphere, i.e., the modification in the $p_f = p_f(\cos\vartheta)$ and $p_f = p_f(\phi)$ behaviour, when varying one selected calibration parameter. For this so called fine tuning of the spectrometer, it was necessary to identify and choose useful calibration parameters. Therefore, the best would be if each momentum component was adjusted mainly by one selected parameter, whereas the impact on the others would be negligible.
On account of the movable design as mentioned in Sections 4.3 and 6.2.1, one can find a lot of calibration parameters at ANKE, for example: target vertex position, deflection angle of the beam, D2 field strength, and positions of the tracking detectors of the Fd system.

At magnetic spectrometers the amount of a particle's momentum is measured by the determination of its rigidity, i.e., its radius of curvature in the magnetic field. For a fixed target experiment, it is evident that, the reconstructed momentum in the laboratory system is primarily dominated by the p_z component, whereas the contributions of p_x and p_y are smaller. The three components, especially p_x and p_z, are interdependent at the track- and momentum reconstruction of the ANKE software. Nevertheless, it is for each momentum component that one corresponding calibration parameter was identified having high impact and twice negligible one on the other two components.

The p_z component mainly depends on the particle's radius of curvature in the magnetic field. On the one hand, it can be changed by adjusting the magnetic field strength of D2 and on the other by shifting the tracking detectors or the target vertex position in xz-plane.
In the first place the p_x component is defined by the beam deflection angle where the target is hit, in the second one, by the incident angle of the produced particles on the chambers. The p_x component can be optimised, firstly, when rotating the chambers about the y-axis or when changing the COSY beam deflection angle.
The p_y component is reconstructed from the y hit positions of the particle track in the first and second MWPC. The p_y component can be adjusted, if one changes the y position of the second chamber relative to the first one.

The relative positions of the Fd system tracking detectors as well as their global position on the moveable platform were optimised in the standard calibration[9]. In this procedure, one particular centre of interest was put on the position in the xz-plane because of the interdependence of these two momentum components. The fine tuning of the spectrometer was executed without changing the xz-positions of the forward tracking detectors, but, by focusing on the other calibration parameters:

- The magnetic field strength of D2 was optimised to correct for p_z
- The deflection angle of the COSY beam was used to rectify p_x
- The component p_y was adjusted by changing the y position of the second MWPC relative to the first one.

Starting from the standard calibration the following three step procedure was applied for the calibration fine tuning.

Step one: Each of the three calibration parameters was changed separately to investigate the corresponding modifications in the $p_f = p_f(\cos\vartheta)$ and $p_f = p_f(\phi)$ spectra. By minimising the asymmetry of p_f at these spectra a new value was fixed for the associated calibration parameter.

Step two: The stability of this new setting was confirmed by repeating step one using smaller parameter variations. In both cases, the first fifth of all the data collected during the beam time was used in order to observe reliable changes in the p_f spectra.

Step three: This kind of calibration procedure was also applied on the last fifth of data in order to get an additional cross check for the stability of the calibration parameters. By this, possible systematic variations were able to be revealed during the beam time.

It should be mentioned, that the computation time was reduced for practical reasons by using a reduced amount of data for the calibration. It makes no sense to increase the precision of the calibration by increasing the amount of data used, because its contribution to the final η mass uncertainty is very small compared to other factors. The changes for each single calibration parameter will be discussed in the following.

[9] See page 93.

6.3.2. Magnetic field strength of D2 and its correction for p_z

The reconstruction of the p_z momentum component was optimised at COSY-ANKE by using the magnetic field strength of D2 as calibration parameter. For the twelve energy settings above threshold the magnetic field of D2 ranged from $B_{\mathrm{D2}} = 1.4162\,\mathrm{T}$ to $B_{\mathrm{D2}} = 1.4350\,\mathrm{T}$. It was changed for each energy above threshold by $\pm\,0.01\,\mathrm{T}$ in the first step and by $\pm\,0.005\,\mathrm{T}$ in the second one of the calibration fine tuning. Figure 6.15 shows the impact on the final state momentum for a change of $\pm\,0.01\,\mathrm{T}$ for an excess energy of $Q = 1.1\,\mathrm{MeV}$ in an exemplary manner. The curves are in black for the standard calibration, in blue for decreasing the magnetic field and in red for increasing it.

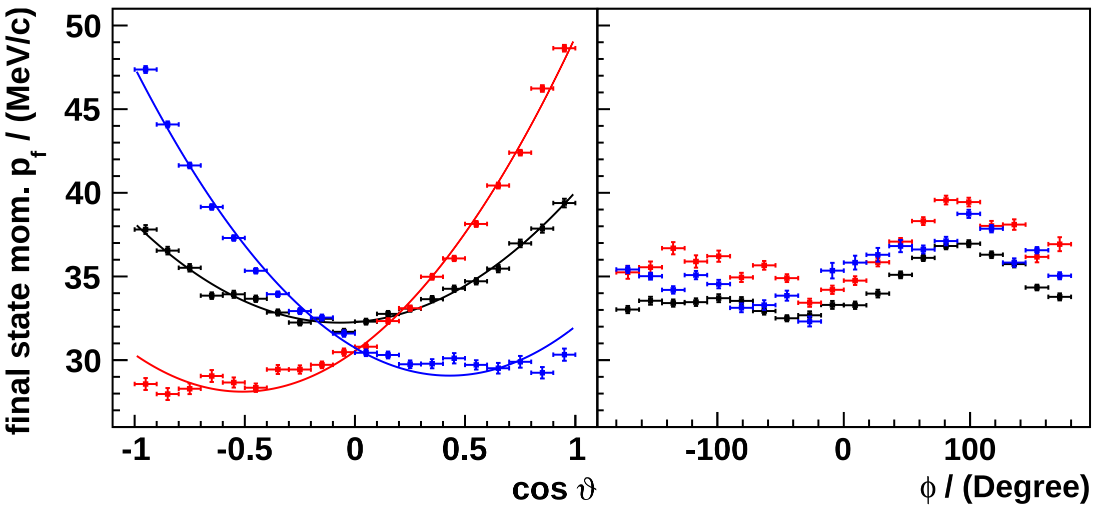

Figure 6.15.: Influence on p_f when changing the magnetic field strength of D2 by $\pm\,0.01\,\mathrm{T}$ at $1.4\,\mathrm{T}$; in black for the standard calibration, in blue for decreasing, and in red for increasing the magnetic field.

While $p_f = p_f(\phi)$ is showing negligible modifications, $p_f = p_f(\cos\vartheta)$ is changing dramatically. When increasing the magnetic field the final state momentum is rising for forward scattered ^{3}He nuclei ($\cos\vartheta \to 1$) and decreasing for backward scattered ones ($\cos\vartheta \to -1$). The process of lowering the magnetic field strength is causing an inverse behaviour. Finally, a variation of the magnetic field strength leads to a shift of the semi-circle in $\pm p_z$ direction, figuratively, On the other side there are no significant modifications in p_x and p_y. This behaviour is similar, if not, even equal for all twelve energies.

In order to optimise the magnetic field strength, each of the three different $p_f = p_f(\cos\vartheta)$ spectra (black, blue and red) were described by a second order polynomial

$$p_f = p_f(\cos\vartheta) = a + b\,\cos\vartheta + c\,(\cos\vartheta)^2\ , \qquad (6.7)$$

as shown in Figure 6.15. The linear term b, representing the slope, was used as control parameter for the symmetry requirement in p_z. That means if b becomes equal zero, the momentum sphere will be perfectly symmetric in p_z. By that a set of three slope parameters (•, •, •) was determined for each of the twelve energies.

Figure 6.16 summarises all twelve sets of slope parameters. The slopes marked

- • as black points belong to the standard calibration
- • as red points to the increased magnetic field strength
- • as blue points to the decreased one.

A straight line from a linear fit connects one set of slope parameters corresponding to one single excess energy.

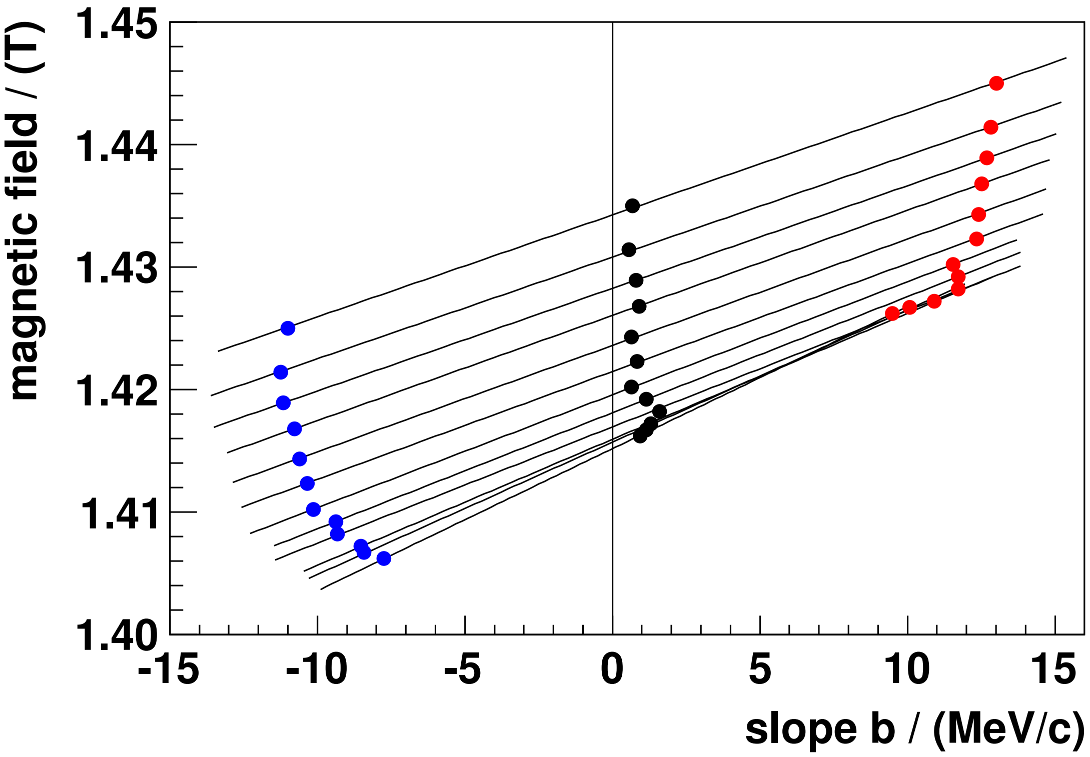

Figure 6.16.: Determination of the correct magnetic field strength by a simple linear fit to the three slope parameters for one excess energy.

The figure shows clearly, that the magnetic field strengths chosen in the standard calibration are systematically too high for all twelve energies. The slope parameters range from (0.6 ± 0.1) MeV/c to (1.6 ± 0.1) MeV/c, resulting in an average value of 1.0 MeV/c. Within the bounds of their uncertainties they are not in agreement with zero. The process of increasing the magnetic field led to an average slope of about 12.0 MeV/c and that one of decreasing to -10.0 MeV/c.

The optimal magnetic field strength was fixed for each energy by using a simple linear fit through the three various slopes. Presenting the field strength as function of the slope parameter as it is done in Figure 6.16 was an ideal method to extract the optimal value. The offset of a linear function, i.e., the intersection with the y-axis, stands in fact for the optimal value of the magnetic field strength. At this point the slope is equal zero. Consequently, $p_f = p_f(\cos\vartheta)$ is perfectly symmetric in p_z.

It is just a reduction by up to 0.0015 T at a magnetic field strength of 1.4 T, i.e., a change of the order of 0.1%, that was necessary for adjusting the p_z component. The comparison between the values of the standard calibration and the new ones is summarized in Section A.5 of the appendix. The fine calibration made it possible to reduce the slope by one order of magnitude for nearly each energy down to $\approx (0.1 \pm 0.1)$ MeV/c. Within their uncertainty limits the slope parameters are consistent with zero and by that in agreement with the results of Monte Carlo simulations. The simulation shows also an average slope of about (0.1 ± 0.1) MeV/c , equally.

It is every time that the fine calibration resulted in the almost same values for magnetic field strength, even when it is repeated using smaller changes in step two or when using the last fifth of data in step three. A difference of only ± 0.0001 T was observed standing for the systematic uncertainty of this method. It should be mentioned that the new determined magnetic field strengths do not necessarily match with the true values, because the reconstruction of p_z also depends on the positions of the tracking detectors or the vertex position in the xz plane. Another correction for p_f in p_z would also be possible by adjusting these other parameters.

6.3.3. Vertical position of the multiwire proportional chambers and its correction for p_y

The p_y component compared to the other two ones has the largest asymmetry in p_f. It was corrected by changing the y-position of the second MWPC relative to the first one. In contrast to the magnetic field strength this parameter is identical for all twelve energies. Therefore it cannot be changed for each setting individually. According to the standard calibration the first chamber is placed at -0.11 mm of the axis and the second one at 0.73 mm. Figure 6.17 emphasises the variation in p_f caused by a change of the y-position for the second MWPC by ± 1 mm. The colour coding is the same as for the p_z case. The black points stand for the standard calibration, blue for decreasing and red for increasing the y-position. One has to keep in mind that step two reduced the variation to $\pm0.3\,$mm, whereas step three used the last fifth of data as input.

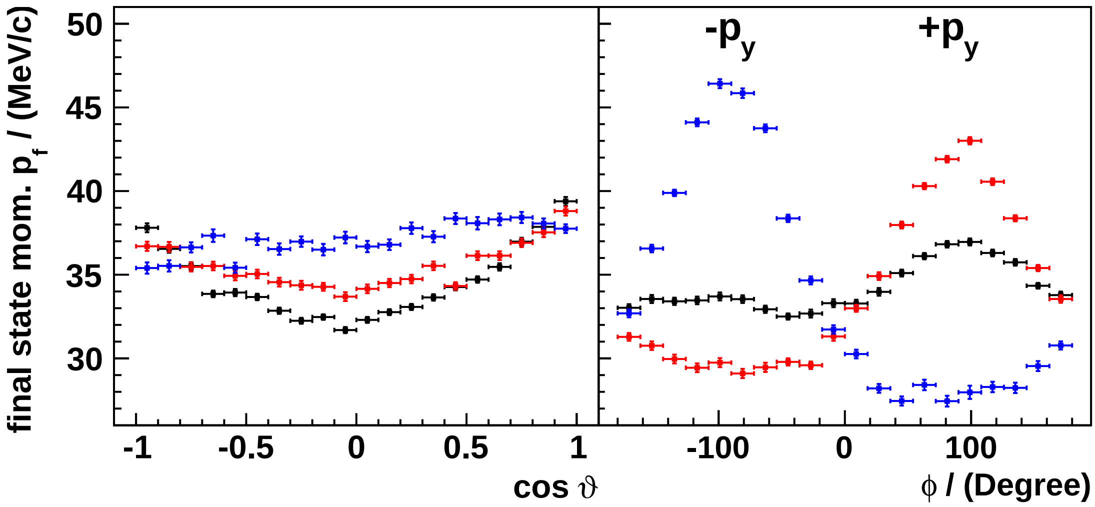

Figure 6.17.: Influence on p_f when changing the y position of the second MWPC by $\pm1\,$mm; in black for the standard calibration, in blue for decreasing, and in red for increasing the y-position of the 2$^{\text{nd}}$ MWPC.

The strongest changes occur in the $p_f = p_f(\phi)$ spectrum at angles of $\pm90°$, where the final state momentum is dominated by the p_y momentum component. The $p_f = p_f(\cos\vartheta)$ spectrum indicates slight modifications, too. At first glance, it seems that they are not negligible at such big changes in the y-position. Finally, the position was corrected by a much smaller value, so that a really significant modification at the $p_f = p_f(\cos\vartheta)$ spectrum did not appear at all.

Again a slope factor, but this time from a linear function was in use as control parameter for the symmetry requirement in p_y. Therefore, the entries at $\phi = \pm90°$ only were taken into account at the $p_f = p_f(\phi)$ spectra, i.e., the entries for the bins $\pm81°$ and $\pm99°$. In contrast all other values were removed. Describing these last four data points by a linear functions leads to a slope parameter, which is exactly a measure for the asymmetry of p_f in p_y.

A set of three slopes was extracted for each of the twelve momentum spheres. They are depicted in Figure 6.18, by plotting the MWPC position against the slope, i.e., asymmetry parameter. This kind of representation as well as the colour coding are the same as for the p_z component. The asymmetry in p_y is shown in black for the standard calibration, in blue for decreasing and in red for increasing the y-position of the second MWPC. From the figure, it becomes more than clear that the y-position was chosen too high in the standard calibration by about 0.4 mm.

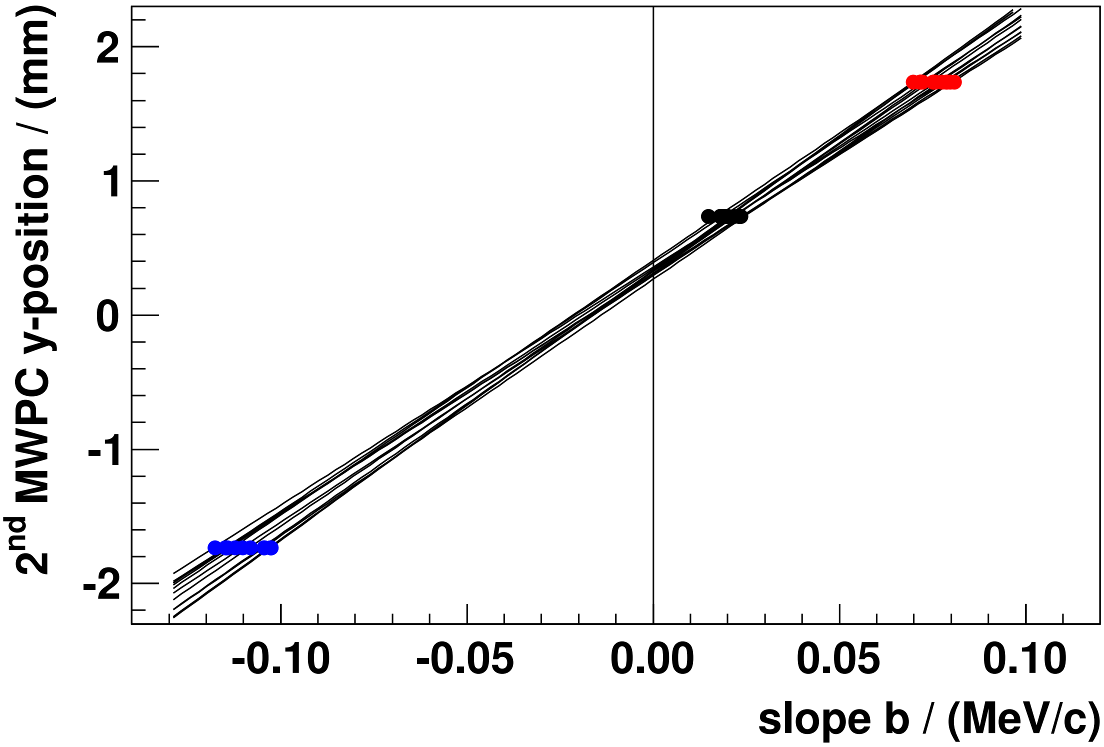

Figure 6.18.: Determination of the correct y position of the second MWPC by a simple linear fit to the three slope parameters extracted for each excess energy.

The optimal y-position for each of the twelve energies was determined by applying a linear fit to the three different slopes. The intersection between the linear function with the y-axis provides the correct y-position of the second MWPC. At this point the slope is equal zero and thus p_f perfectly symmetric in p_y. The new y-positions range from 0.3 mm to 0.36 mm for the twelve various energies. The further analysis made clear that an average value of (0.34 ± 0.02) mm was valid and could be used for all energies. So it is only by a tiny change of $\approx$ 0.39 mm from 0.73 mm to 0.34 mm for the y-position of the 2$^{\text{nd}}$ MWPC, that the shape of the momentum sphere could be corrected in p_y. The scale of this correction proves the sensitivity of the method. Even when repeating the procedure using smaller variations in the y-position or referring to the last fifth of the data leads to an uncertainty of $\pm$0.02 mm, only, showing the stability of the new calibration parameter.

6.3.4. Beam deflection angle and its correction for p_x

The deflection angle of the COSY beam caused by the D1 magnet was chosen in order to optimise the symmetry requirement of p_f in p_x. In the standard calibration the deflection angle ranges from 5.803° to 5.816° at the different energy settings (see Table A.1). Figure 6.14 clearly reveals that this component fulfils the symmetry requirement at its best. Consequently, the corrections will be very limited, if not even negligible. Figure 6.19 illustrates the modification in p_f after having changed the deflection angle by $\pm 0.1°$ in the first step of the fine tuning. Afterwards a variation of $\pm 0.02°$ was carried out in the second step.

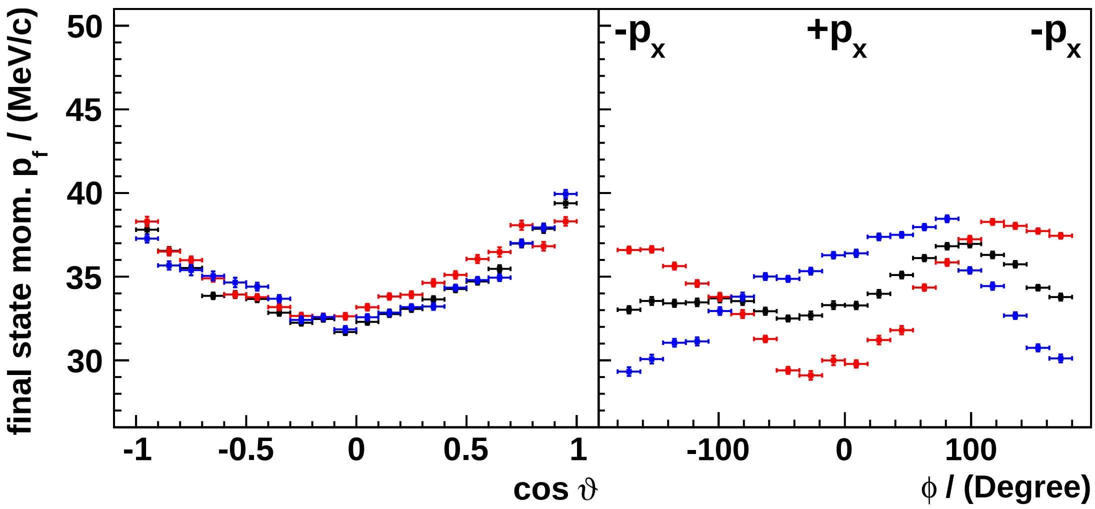

Figure 6.19.: Influence on p_f when changing the deflection angle of the COSY beam onto the target by $\pm 0.1°$; in black for the standard calibration, in blue for decreasing, and in red for increasing the deflection angle.

As expected the strongest modifications appear in the ϕ spectrum at angles of $\pm 180°$ and 0°, where the p_x contribution dominates the final state momentum. It is at $\phi = \pm 90°$, i.e., in p_y, as well as in the $p_f = p_f(\cos\vartheta)$ spectrum that the figure does not show any significant changes. A slope parameter from a linear function was used again as control parameter for the symmetry requirement in p_x. Therefore, exclusively the entries for the bins $\pm 9°$ and $\pm 171°$ were taken into consideration, exclusively. They were shifted by 90° for linear fitting. The slopes, i.e., the asymmetry of p_f in p_x, are shown for the three cases in Figure 6.20 for all twelve energies. At the standard calibration almost all asymmetry parameters of p_x are already distributed around zero, that means there is no significant systemic deviation. This is contrary to the cases of p_z and p_y. It is only the highest excess energy revealing an asymmetry.

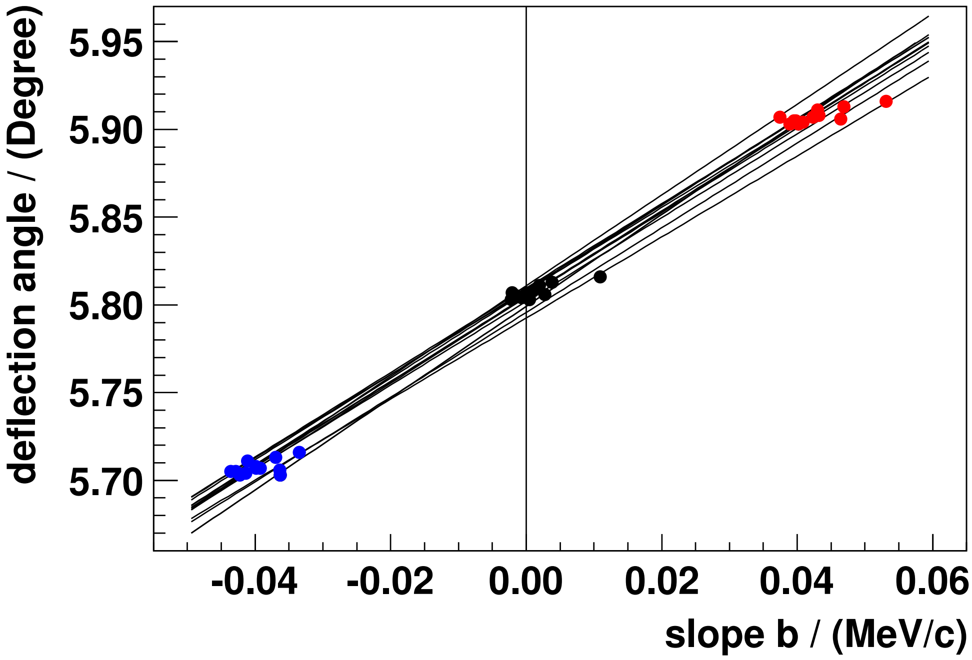

Figure 6.20.: Determination of the correct deflection angle of the beam onto the target by a simple linear fit to the three slope parameters extracted for each excess energy.

As for both other components new calibration parameters, i.e., deflection angles, were determined by using a linear fit. These are listed in Table A.1 of the appendix. In the p_x case the corrections at deflection angles of 5.8° were below 0.03°, that means just 0.4%. The correction decreases even below 0.01° when excluding the highest and most deviating excess energy. The variation of the deflection angle becomes even less to about ±0.004° when repeating the fine calibration procedure at smaller changes of ±0.02° in step two. The changes will even move in the same scale as previously, if one considers the last fifth of the data as input. This is a clear indicator for the stability of the new calibration parameters. The values for some of the twelve new deflection angle match with the old ones in the scope of their uncertainty limits. That means, a readjustment was not urgently necessary, in principle.

However, a correction for the reconstruction of p_z and p_y was inevitable for a precise determination of resolution parameters (see next Section 6.4). The magnitudes of the calibration parameter changes are so small that they have no impact on the values of the missing masses for the different reactions used in the standard calibration [Dym12]. The calibration parameters for both settings, the standard ones and the improved ones, are compared in the appendix in Section A.5.

6.4. Determination of final state momenta

The previous discussion in Section 6.1.2 made clear that resolution effects cause a deviation of the reconstructed final state momentum from the kinematically correct value. Therefore, it is absolutely needed to extract from data the resolutions of the individual momentum components $(\sigma_x, \sigma_y, \sigma_z)$. This is indispensable in order to quantify correction parameters for the measured p_f by Monte Carlo simulations.

At two previous analysis [Mer07, Rau09], the resolution in p_x and p_y was not considered separately, but merged into a smearing of the transverse component $p_\perp$. At that time this consideration was sufficient, because in contrast to the η mass analysis, the previous ones focussed on the amount of events for extracting cross sections, instead of the absolute position. A smearing of $(\sigma_\perp, \sigma_z) = (8, 22)\,\mathrm{MeV/c}$ was chosen for the excess energy range from threshold up to $Q = 60\,\mathrm{MeV}$ in order to realise the smearing of the $^3\mathrm{He}$ laboratory momenta in Monte Carlo simulations. Those parameters were determined by studies of widths for missing mass peaks at different $\cos\vartheta$ bins[10].
Examining the shape of the momentum sphere, i.e., the dependence $p_f = p_f(\cos\vartheta)$ and $p_f = p_f(\phi)$, allows one to determine the momentum smearing in the three directions in a more elegant way. This was made only possible by the fine tuning of the calibration parameters which improved the $p_f = p_f(\cos\vartheta)$ and $p_f = p_f(\phi)$ spectra.

Figure 6.21 summarises exemplarily for one energy the success of the refined spectrometer fine tuning and it allows for an exact comparison. The top panel shows the shape of the momentum sphere at the standard calibration, whereas the bottom panel indicates the improved sphere after having fine tuned the spectrometer.
The asymmetric contributions in the $p_f = p_f(\cos\vartheta)$ and $p_f = p_f(\phi)$ spectra, i.e., the asymmetry of the momentum sphere, make clear that the standard calibration was just able to provide a rough and inexact momentum reconstruction with regard to the $\mathrm{d\,p} \to {}^3\mathrm{He}\,\eta$ reaction. It is only by an exact fine tuning that the momentum spheres become almost perfectly symmetric in the three momentum components. The remaining structures are mainly due to resolution and smearing effects of the ANKE setup as well as to momentum reconstruction algorithms as explained in Section 6.1.1.
Monte Carlo simulations without smearing are represented by the red horizontal line in Figure 6.21, showing the isotropy of p_f. The red crosses symbolise simulations with smearing effects, matching very well with the data. The implementation of resolution parameters in Monte Carlo simulations allows one to calculate correction parameters for the measured final state momenta.

[10] The p_f signal for $\cos\vartheta \to \pm 1$ was used to extract σ_z and $\cos\vartheta \to 0$ to fix $\sigma_\perp$. This is composed of $\sigma_\perp^2 = \sigma_x^2 + \sigma_y^2$.

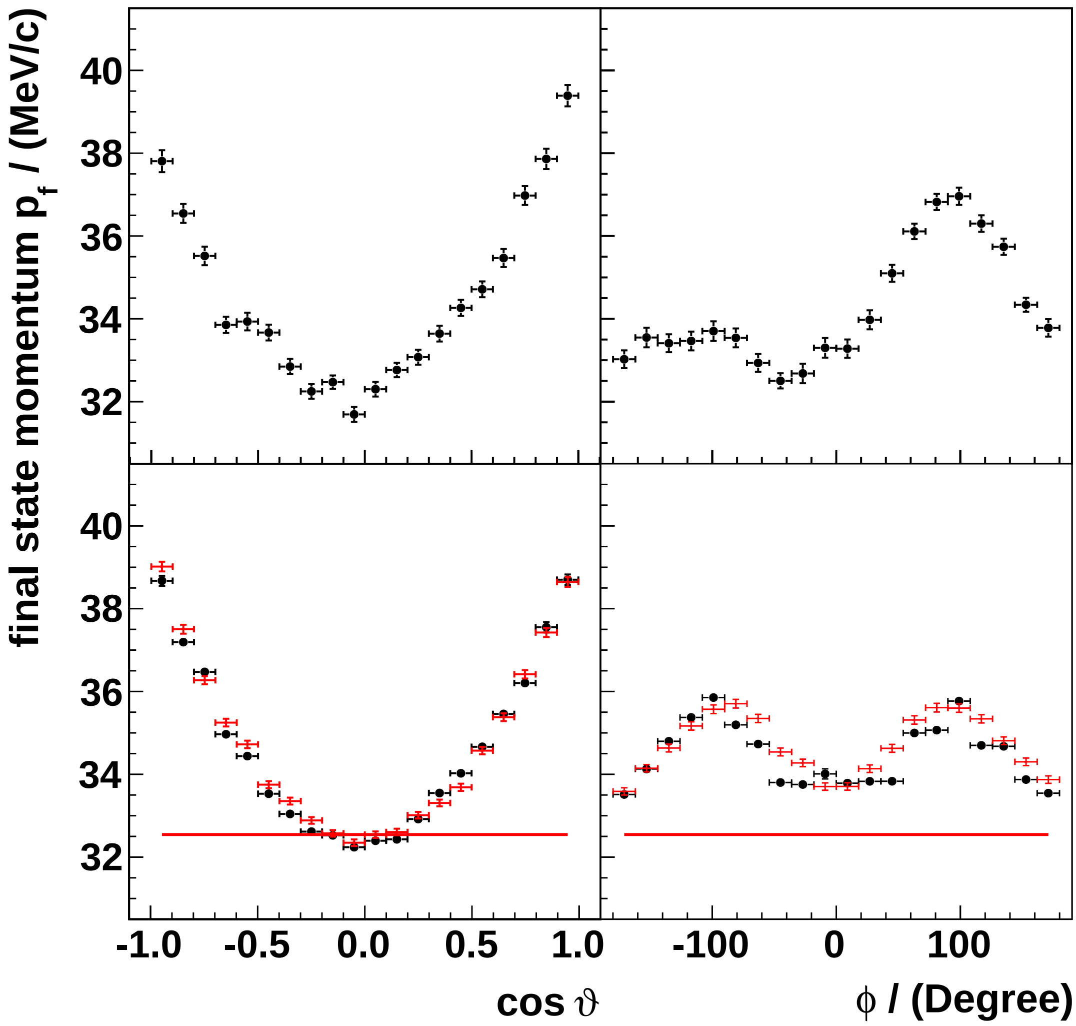

Figure 6.21.: Mean values of the p_f distributions are shown for individual $\cos\vartheta$ and ϕ bins for the standard (top) and improved (bottom) calibration at $Q = 1.1\,\text{MeV}$ (black circles). The results of Monte Carlo simulations are shown without (red, horizontal line) and with momentum smearing (red crosses). The comparison of the data with simulations permits the determination of the momentum resolution in the three directions.

6.4.1. Determination of resolution parameters

An iterative procedure was developed, then applied in order to determine the resolution parameters for the three momentum components. It turned out to be the best and fastest way if focussing on three control parameters extracted from data. The smearing $(\sigma_x, \sigma_y, \sigma_z)$ was extracted for each of the twelve energies.

- The values for σ_x and σ_y were determined from the amplitude and the phase of the oscillation in the $p_f = p_f(\phi)$ spectrum.
- The smearing σ_z was extracted from the magnitude of the quadratic term in the $p_f = p_f(\cos\vartheta)$ spectrum.
- In addition, an important constraint is fixed by the measured width of the $^3\text{He}\,\eta$ final state momentum signal when integrating over all $\cos\vartheta$ and ϕ. This quantity covers all resolution and smearing effects at once and must be reproduced by Monte Carlo simulations that comprises the ANKE resolution.

Firstly, the $p_f = p_f(\phi)$ spectra were described by a general sine function

$$p_f = p_f(\phi) = a + b\sin(c\phi + d) \tag{6.8}$$

in order to determine σ_x and σ_y. The boundary conditions for this case fix the frequency parameter c and phase d ($c = 2$ and $d = \pi/2$), consequently the free parameters are reduced from four to two. The least square fit takes into account the offset parameter a and the amplitude of the oscillation b, exclusively.
The amplitudes for the twelve energies range from (1.07 ± 0.05) MeV/c to (0.73 ± 0.05) MeV/c, indicating a decrease with rising excess energy. These values comprise information about the ratio of σ_x/σ_y. It is optimal how the simulations describe the oscillation curves for each energy by using the extracted smearing parameters listed in Table 6.1. In this case the amplitudes of the oscillations for data and Monte Carlo simulations match within their uncertainty limits.

Secondly, the $p_f = p_f(\cos\vartheta)$ spectra were described by a polynomial function of second order as explained in Section 6.3.2. The quadratic fit parameter[11] c is a direct measure for the magnitude of the smearing in p_z. To be more precise, it is a measure of the ratio $\sigma_\perp/\sigma_z$. The quadratic term is (7.03 ± 0.08) MeV/c for the data closest to threshold and decreases steadily up to (2.75 ± 0.08) MeV/c with growing excess energy. This behaviour is reasonable, because the final state momentum rises with increasing excess energy, whereas the resolution stays nearly constant. The same quadratic parameters were realised using Monte Carlo simulations, in which the smearing of the laboratory p_z component was modelled by Gaussian distributions with the widths σ_z listed in Table 6.1.

[11] See Equation (6.7) on page 116.

Technically the ratio of σ_x/σ_y and $\sigma_\perp/\sigma_z$ can be extracted only, if one considers the amplitude of the oscillation in $p_f(\phi)$ and the quadratic term in $p_f(\cos\vartheta)$, exclusively. An additional parameter was needed in order to fix the absolute values and found in the width of the p_f signal. It ranges from (8.00 ± 0.02) MeV/c to (8.17 ± 0.02) MeV/c for the twelve energies studied because of alignment and calibration limitations. These one define the uncertainties for the determined resolution parameters.

Data Points	Resolution σ_x /(MeV/c)	σ_y /(MeV/c)	σ_z /(MeV/c)
1	4.5	7.5	16.7
2	4.2	7.6	16.5
3	3.6	7.7	16.1
4	3.8	7.9	16.1
5	4.0	7.2	16.5
6	3.4	7.3	16.9
7	2.4	7.7	16.7
8	3.0	8.0	16.2
9	2.0	8.2	16.4
10	1.1	8.5	16.5
11	1.0	8.5	16.2
12	1.0	9.1	16.4
	Uncertainties $\Delta\sigma_x$ /(MeV/c)	$\Delta\sigma_y$ /(MeV/c)	$\Delta\sigma_z$ /(MeV/c)
	±0.2	±0.2	±0.1

Table 6.1.: Individual smearing $(\sigma_x, \sigma_y, \sigma_z)$ for the three momentum components extracted from data and used in Monte Carlo simulations.

The smearing parameters $(\sigma_x, \sigma_y, \sigma_z)$ were determined in an iterative way. The values $(\sigma_x, \sigma_y, \sigma_z) = (5, 7, 16)$ MeV/c were used as starting point for each energy. These ones are average values from the peak widths extracted at special $\cos\vartheta$ and ϕ bins where one of three momentum component clearly dominates p_f. The final values resulted from the iterative procedure by varying the resolution parameters as long as all three control parameters, i.e., the amplitude of the oscillation in $p_f(\phi)$, the quadratic term in $p_f(\cos\vartheta)$, and finally the total p_f width, agreed for data and Monte Carlo simulations. They are listed in Table 6.1 for all twelve energies. The precision of the resolution parameters $(\Delta\sigma_x, \Delta\sigma_y, \Delta\sigma_z) = (0.2, 0.2, 0.1)$ MeV/c is defined by the uncertainty limits of the control parameters. Those ones in turn depend on the calibration limitations.

In contrast to σ_z, which is constant within 1 MeV/c, it seems as if σ_x is decreasing, while σ_y is increasing with excess energy. This behaviour is reasonable because the cone angle of the ^{3}He ejectiles from the $\mathrm{d\,p} \to {}^3\mathrm{He}\,\eta$ reaction increases with excess energy. It is close to threshold, that the hit positions are located in a small area near the centre of the wire chambers, whereas hits at higher excess energies are more widely distributed. However, the transversal smearing $\sigma_\perp$, calculated from σ_x and σ_y, is nearly constant at about 8.5 MeV/c for all twelve energies. This is a similar value compared to that one used in previous analysis [Mer07, Rau09]. As expected the resolution for p_z is the worst at a fixed target experiment.

6.4.2. Correction of final state momenta

The resolution effects are optimally described for each energy when implementing the smearing parameters listed in Table 6.1 in Monte Carlo simulations. The widths for the individual $\cos\vartheta$ and ϕ bins are reproduced to high precision in combination with the deformation of the momentum sphere, depicted in Figure 6.21. Figure 6.22 proves the clear agreement of data and smeared simulations. It shows the background subtracted distribution of p_f integrated over all $\cos\vartheta$ and ϕ at an excess energy of $Q = 7.0\,\mathrm{MeV}$[12].

Due to resolution effects, the p_f distribution for data shown as red filled area is slightly asymmetric. It is reproduced in an almost identical manner by Monte Carlo simulations depicted as black crosses. The vertical line indicates the kinematically correct final state momentum without smearing effects.
Correction parameters were calculated for all twelve energies by comparing the mean values from the Monte Carlo simulations with and without momentum smearing. The deviation of the reconstructed mean value from the true one is directly the correction for p_f. The mean values of the smeared distributions were extracted from a $\pm 3\,\sigma$ region around the peaks as it was done for data. It is important that the extraction of the average p_f values was treated equally referring to data and simulations. This is for avoiding an additionally systematic error. The determined correction parameters are listed in Table 6.2 and plotted versus the kinematically correct p_f value in Figure 6.23.

The deviation is about (2.22 ± 0.08) MeV/c for the lowest momentum, decreasing steadily down to (0.74 ± 0.04) MeV/c with growing final state momentum. It should decrease exactly with $1/p_f$ for a perfect calibrated detector as discussed in Section 6.1.2. But there is still a scatter in the points about any smooth line, because the input parameters, i.e., the smearing values, were obtained by fitting

[12] For the sake of completeness the final state momentum distribution for all energies are shown together for data and smeared Monte Carlo simulations in the appendix Section A.6

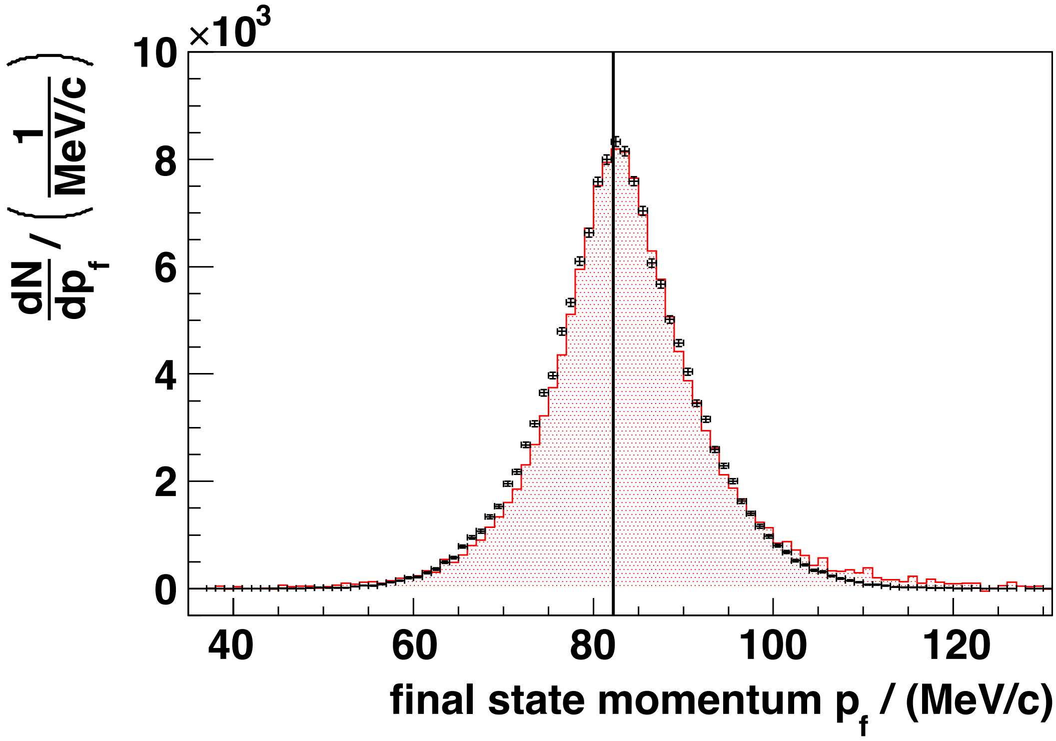

Figure 6.22.: Final state momentum distribution for background subtracted $\mathrm{d\,p} \to {}^3\mathrm{He}\,\eta$ data (filled red area) and simulation including resolution effects (black crosses) at an excess energy of $Q = 7.0\,\mathrm{MeV}$. The vertical line indicates the kinematically correct final state momentum.

experimental data (see Section 6.4.1). This approach includes alignment and calibration limitations provoking in a deviation from the $1/p_f$ fit, shown as red line. The good $\chi^2/\mathrm{NDF} \approx 0.9$ of the fit proves the validity of the determined uncertainties for the correction. The error bars result from error propagation, transforming the uncertainties of the smearing values $(\Delta\sigma_x, \Delta\sigma_y, \Delta\sigma_z) = (0.2, 0.2, 0.1)\,\mathrm{MeV/c}$ into those ones of p_f correction parameters.

Mathematically, the correction parameters for p_f are primarily defined by the resolution parameters. Nevertheless, they are also dependent on the η mass value assumed in simulations.
For example the simulated p_f momenta of the reaction $\mathrm{d\,p} \to {}^3\mathrm{He}\,\eta$ are higher, when assuming a lower mass of $m_\eta = 547.3\,\mathrm{MeV/c^2}$ instead of the PDG value. Consequently, the determined resolution parameters would be higher leading to larger correction parameters and finally to a lower η mass value. The difference of $\Delta m_\eta \approx 550\,\mathrm{keV/c^2}$ in simulations provokes a shift of the obtained η mass of

Data Points	p_f correction parameter / (MeV/c)	Uncertainty / (MeV/c)
1	2.22	0.08
2	1.94	0.06
3	1.69	0.06
4	1.57	0.05
5	1.35	0.05
6	1.28	0.04
7	1.07	0.05
8	0.95	0.04
9	0.88	0.03
10	0.84	0.04
11	0.76	0.04
12	0.74	0.04

Table 6.2.: Correction parameters for the measured p_f estimated by Monte Carlo simulations.

$\approx 20\,\mathrm{keV/c^2}$. However, this is smaller than the finally systematic uncertainty of the COSY-ANKE outcome.

The PDG estimation was used for the η mass in the COSY-ANKE analysis, making it possible to determine a final COSY-ANKE η mass value. The analysis was repeated a second time using the previous COSY-ANKE outcome as new input for Monte Carlo simulations. The new result showed just a very tiny deviation of below $2\,\mathrm{keV/c^2}$ in contrast to the previous value. This examination underlines the insensitivity to the mass assumed in simulations. In comparison to other contributions its influence on the final uncertainty is very small. So it must be concluded that the dependence of the correction parameters on the value assumed for the mass in simulations is negligible.

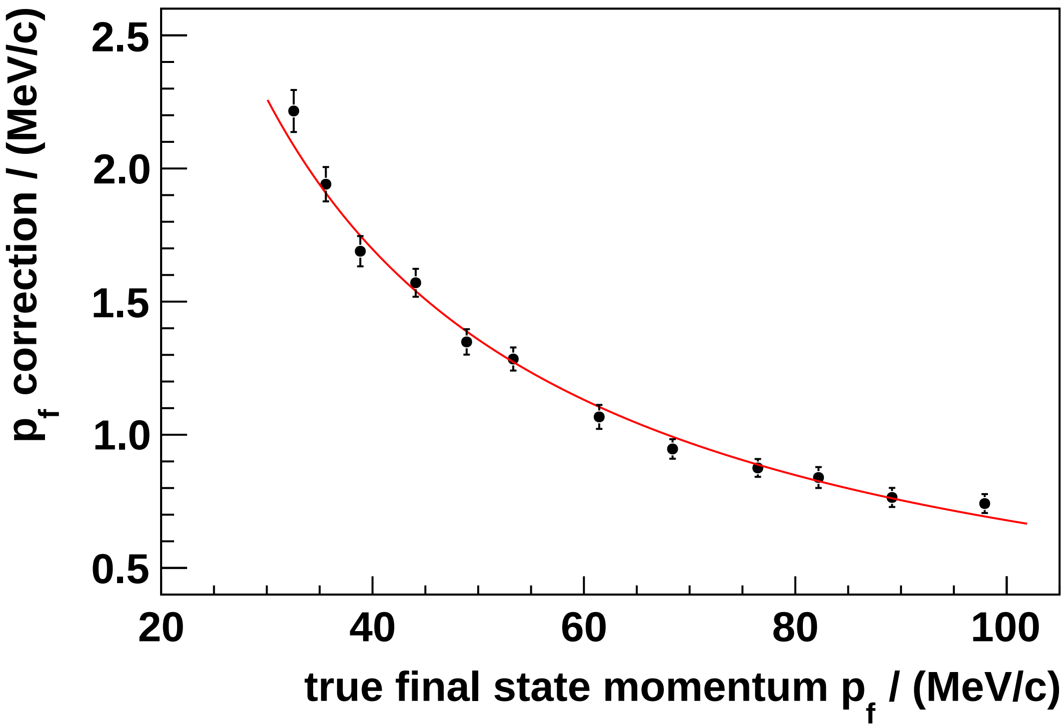

Figure 6.23.: Deviation of the measured final state momenta from the true ones due to resolution effects evaluated in Monte Carlo simulations. The twelve measured final state momenta in the near threshold region from $Q = 1 - 10\,\mathrm{MeV}$ have to be corrected by values from $0.7 - 2.2\,\mathrm{MeV/c}$ in order to compensate for such effects. The curve is a $1/p_f$ fit to the points.

6.4.3. Reconstructed final state momenta

Table 6.3 presents the already corrected final state momentum values and their statistical uncertainties for all twelve data points. These ones were used in the threshold extrapolation.
The values of the p_f averages were determined statistically within $\pm 3\,\sigma$ limits from the pure background subtracted p_f distributions as shown in Figure 6.22 for a typical energy. The good statistics of $\approx 1.3 \times 10^5$ $^3\mathrm{He}\,\eta$ events for each energy meant that the uncorrected value for p_f could be extracted with an uncertainty of $\approx 23\,\mathrm{keV/c}$. The experiment collected $\approx 1.5 \times 10^6$ $^3\mathrm{He}\,\eta$ events in total. After having applied the resolution correction for the measured p_f, the total uncertainty increased. By this, it was dominated by the errors of the correction parameters, as indicated in Table 6.3.

Data Points	Final state mom. p_f / (MeV/c)	Uncertainty Δp_f / (MeV/c)
1	32.46	0.08
2	35.56	0.07
3	39.00	0.06
4	44.09	0.06
5	49.25	0.05
6	53.66	0.05
7	61.70	0.05
8	68.77	0.04
9	76.92	0.04
10	82.64	0.05
11	89.81	0.04
12	98.64	0.04

Table 6.3.: Final state momenta and their statistical uncertainties for all twelve energy settings used in the threshold extrapolation.

Although the p_f distributions for data and simulations match mostly acceptably (see Figure 6.22), this is not perfect naturally, especially in the high momentum tail. Such discrepancies might arise from slight imperfections in the spectrometer calibration, ^{3}He scattering in the wire chambers, or limitations in the background subtraction approach. If data and simulations matched perfectly, the corrected p_f averages would be completely independent of the interval used for their determination. The explanation of this fact is very simple: By changing the p_f interval for average extraction, a slightly different average is expected. This small difference will be compensated by the correction parameter if its interval is adapted in the same manner.

But in real, the small deviation in the p_f distributions for data and simulations must to be taken into account as an additional systematic uncertainty. In order to quantify this systematic contribution the interval was varied between $\pm 2\,\sigma$ to $\pm 4\,\sigma$, where σ represents the peak width. Such a variation leads to a collective shift in the extracted final state momenta of approximately 0.16 MeV/c. This systematical error is not included in Table 6.3 because the values in there are of purely statistical nature. However, its contribution must be taken into consideration at the final η mass determination, introducing a systematic uncertainty of 12 keV/c^2.

A more detailed discussion about systematic uncertainties of p_f and their impact on the final η mass value will follow in the next section.

7. COSY - ANKE η mass result

In order to obtain a robust value for the mass of the η meson, it was necessary to extrapolate the experimental data with high precision to threshold as described in Chapter 3. The beam momentum at threshold corresponds directly by Equation (3.16) to the η mass. Table 7.1 lists the set of twelve COSY beam momenta and associated corrected final state momenta (p_d, p_f) which were used for this purpose (see also Tables 5.6 and 6.3).

Excess energy Q / (MeV)	Beam momentum p_d / (MeV/c)	Final state momentum p_f / (MeV/c)
1.0	3146.41 ± 0.03	32.46 ± 0.08
1.2	3147.35 ± 0.03	35.56 ± 0.07
1.5	3148.45 ± 0.03	39.00 ± 0.06
2.0	3150.42 ± 0.03	44.09 ± 0.06
2.4	3152.45 ± 0.03	49.25 ± 0.05
2.9	3154.49 ± 0.03	53.66 ± 0.05
3.9	3158.71 ± 0.03	61.70 ± 0.05
4.8	3162.78 ± 0.03	68.77 ± 0.04
6.0	3168.05 ± 0.03	76.92 ± 0.04
7.0	3172.15 ± 0.03	82.64 ± 0.05
8.2	3177.51 ± 0.03	89.81 ± 0.04
9.9	3184.87 ± 0.03	98.64 ± 0.04

Table 7.1.: Values of the laboratory beam momenta p_d and associated corrected final state CM momenta p_f with statistical uncertainties are noted for all twelve different excess energies. The approximate values of Q quoted here are merely used to label the twelve settings.

The extrapolation of the data to threshold is illustrated in Figure 7.1 for both p_f and p_f^2 versus p_d. As first sight p_f^2 depends linearly on p_d in the first approximation. However, the analysis take into consideration the full dependence $p_f = p_f(m_\eta, S, p_d)$ as given by Equations (3.13) and (3.15). The η mass only, chosen as a free parameter, defines the production threshold. The scaling factor S, discussed in Section 3.2.3, allows for a possible systematic energy dependence of p_f. This would represent yet a further fine tuning, describing the measurement process. Nevertheless, it is crucial to note that its introduction does not affect the value obtained for the threshold momentum and hence m_η.

The overall least square fit to the data in Figure. 7.1 has a χ^2/NDF = 1.28 providing the best value of the mass $m_\eta = (547.873 \pm 0.005)\,\mathrm{MeV/c^2}$. The error is primarily statistical and quoted together with the final results in Table 7.2. The corresponding deuteron momentum at threshold is $p_d = (3141.688 \pm 0.021)\,\mathrm{MeV/c^2}$. A linear fit of p_f^2 versus p_d, which is only an approximation of the kinematics as already discussed in Section 3.2.2, would give a poorer reduced χ^2 and a 10 keV/c^2 higher mass value.

Supercycle	Scaling factor S	η mass m_η / (MeV/c^2)
1+2	1.008 ± 0.001	547.873 ± 0.005
1	1.008 ± 0.001	547.870 ± 0.007
2	1.008 ± 0.001	547.877 ± 0.007

Table 7.2.: Values of the η mass and scaling factor evaluated separately for the two supercycles and for the complete data set. The errors do not include the systematic uncertainties of COSY beam and p_f determination estimated in the analysis.

The scaling factor $S = 1.008 \pm 0.001$ is well determined by the least square fit. It differs very slightly from unity which means that the twelve momentum spheres are about 0.8% bigger in average than expected. One consequence of this is that the missing mass is not constant, so one would get a slightly different value at each of the twelve energies. It would be necessary to improve the absolute momentum calibration of ANKE in order to eliminate this behaviour, ensuring by this a scaling factor of $S = 1$. This can only be realised by studying kinematics of other reference reactions. However, the approach chosen in this analysis compensates such effects and does not require an absolute calibration.
If one fixed $S = 1.0$ in the least square fit, the fit would deviate systematically from the data points. This implies at the same time a jump of χ^2/NDF to 24.7 that proves a completely wrong description of the measured data. By this the extracted value for the η mass would be lowered by 64 keV/c^2 to 547.809 MeV/c^2. The threshold

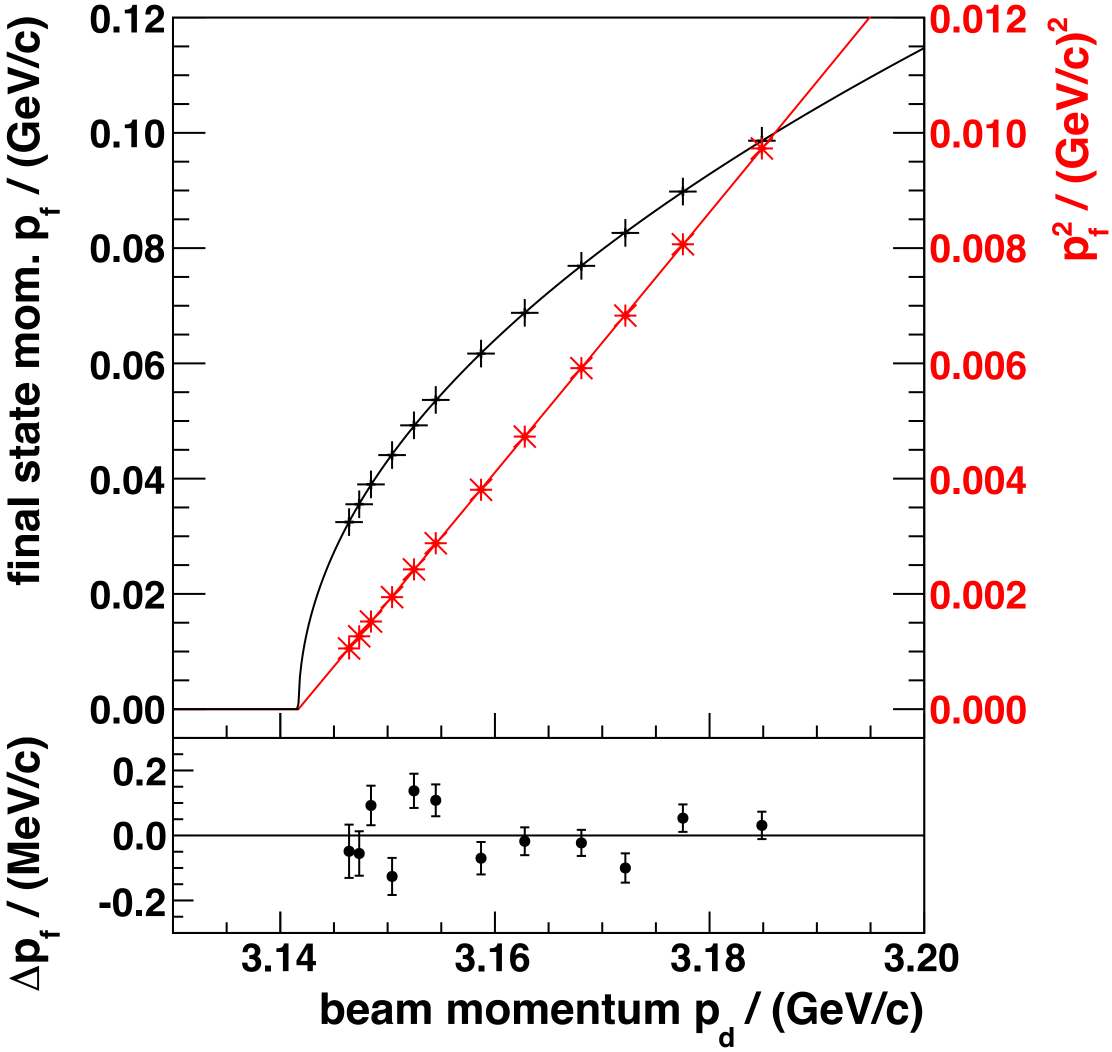

Figure 7.1.: Corrected values of the final state CM momentum p_f (black crosses) and its square (red stars) plotted against the deuteron laboratory momentum p_d. The error bars are too small to be shown on the figure. The extrapolation to threshold was carried out on the basis of Equation (3.15), whereby a scaling factor S was introduced. The lower panel shows the deviations of the experimental data from the fitted curve in p_f. The errors shown here do not include the total systematic uncertainty in p_f listed in Table 7.3.

determination method chosen at COSY-ANKE avoids such a systematic error as shown in Section 3.2 by investigation a larger number of data points. In general, a measurement at one single energy is not able to recognise a possible energy dependence represented by S.

The totally systematic uncertainty of the obtained η mass is composed of various systematic errors based on the COSY beam momentum determination and the various steps in the final state momentum analysis. They are all summarised in Table 7.3.
The dominant systematic error by far results from the determination of the absolute COSY beam momentum value. The analysis showed a possible systematic variation of $\Delta p_d^{\text{syst.}} = 95\,\text{keV/c}$ for the average COSY momentum, calculated from the values of the first and second spin resonance measurement. According to the following equation

$$\Delta m_\eta = \frac{m_p\, p_d}{(m_{^3\text{He}} + m_\eta)\, E_d}\, \Delta p_d = 23\,\text{keV/c}^2 \tag{7.1}$$

the systematic COSY beam momentum uncertainty translates into one in the η meson mass of $\Delta m_\eta = 23\,\text{keV/c}^2$.
Besides that the various steps of the final state momentum analysis contribute differently to the systematic uncertainty of the determined p_f values. The biggest error is caused when determining correction parameters to p_f. If simulations and data matched perfectly (see Figure 6.22), the corrected p_f values should be independent of the interval chosen for p_f mean extraction as explained in Section 6.4.3. However, this is not the fact because of limitations in momentum calibration and determination of resolution parameters. This produces an almost normal systematic uncertainty. Variations between $\pm 2\,\sigma$ to $\pm 4\,\sigma$ region of the used interval for determining the p_f means provoke a collective shift in the extracted p_f of about $160\,\text{keV/c}$. This translates into a systematic mass uncertainty of $\pm 12\,\text{keV/c}^2$.

In comparison, all other sources have less impact on the final state momenta and consequently on the final η mass value.
For example, the "Experimental settings" summarise different effects from the time stability and further contributions from the fine calibration. The first and last fifth of data exclusively were used for fine tuning of calibration parameters, allowing a verification of the time stability. The extraction of the η mass for both setting shows a tiny negligible deviation of $2\,\text{keV/c}^2$ only.
The variations of cuts in the event selection, i.e., energy loss cut and path length one, are another possible source for systematic errors. They affect the background description and so the final p_f values. The systematic uncertainty of the event selection cuts was estimated to be $\approx 5\,\text{keV/c}^2$ by changing the cut intervals in the analysis.
The mass value assumed in simulations also influences the final η mass value as

Source	Variation	$\Delta m_\eta/(\mathrm{keV/c^2})$
Absolute beam momentum	95 keV/c	23
Experimental settings		2
$\Delta E \times \beta^2$ cut	$6\sigma \to 2\sigma$	5
Flight length cut	$3\sigma \to 2\sigma$	1
m_η assumed in simulations	$20\,\mathrm{keV/c^2}$	< 2
p_f correction parameters	$4\sigma \to 2\sigma$	12
Total systematic uncertainty		27

Table 7.3.: Systematic uncertainties of m_η determination. The small "Experimental settings" include effects resulting from turning calibration parameters. The PDG value of m_η [N$^+$10] was used in the simulations but, if the COSY-ANKE one was applied, a $2\,\mathrm{keV/c^2}$ change only would follow. Also listed are the effects when putting stricter cuts on $\Delta E \times \beta^2$ and the flight length.

discussed in Section 6.4.2. All individual systematic uncertainties give rise to a totally systematic one of $27\,\mathrm{keV/c^2}$, resulting in a final COSY-ANKE η mass value of

$$m_\eta = (547.873 \pm 0.005_{\mathrm{stat}} \pm 0.027_{\mathrm{syst}})\,\mathrm{MeV/c^2}\ . \tag{7.2}$$

In order to investigate more possible hidden systematic effects the data set (p_d, p_f) obtained in the two supercycles were extrapolated separately. In this way each supercycle represents an independent measurement. Table 7.2 shows the individual values of the η mass and the scaling factor S with regard to the two supercycles. There is only a very tiny difference of $7\,\mathrm{keV/c^2}$ between the two separately determined η mass values, which is much smaller than the estimated systematic uncertainty.
In addition the (p_d, p_f) data set was subdivided into seven equally time periods of approximately 18 hours for investigating possible systematic changes in time. One example for a quantity which might change in time is the beam momentum of COSY (see Section 5.3.3). Figure 7.2 illustrates the results of the threshold extrapolation for the seven reduced data sets; in black for both supercycles together, in red only for the 1$^{\mathrm{st}}$ supercycle, and in blue only for the 2$^{\mathrm{nd}}$ one. The minimum and maximum of the ordinate of the plot were chosen in this way to cover the total systematic uncertainty of about $\Delta m_\eta^{\mathrm{syst.}} = \pm 0.027\,\mathrm{MeV/c^2}$ of the COSY-ANKE result. The black dashed line represents the final COSY-ANKE value. The time dependence of the COSY-ANKE η mass value shows solely statistical fluctuations

and no systematic drift in time. The statistical variations are much smaller than the total systematic uncertainty. This agreement supports the validity for taking the mean values of the beam momenta which were determined at the beginning and the end of the measuring period. Finally, it emphasises the correct handling of systematic uncertainties.

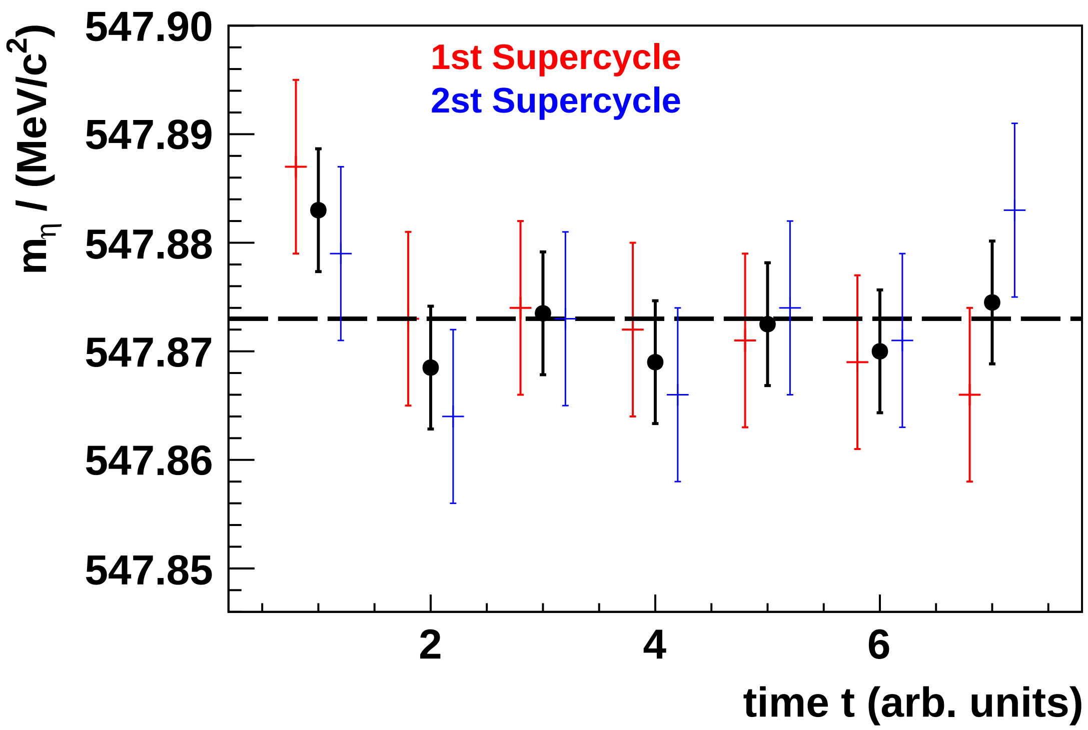

Figure 7.2.: Results of the threshold extrapolation using seven reduced data sets, each one consisting of approximately 18 hours of data taking. The black points symbolise the results using data of both supercycles together, the red one stand for the 1$^{\text{st}}$ supercycle, and the blue for the 2$^{\text{nd}}$ one.

8. Conclusions

The COSY-ANKE experiment determined the mass of the η meson in a missing-mass approach by identifying precisely the production threshold in the $\mathrm{d\,p} \to {}^3\mathrm{He}\,\eta$ reaction. The final outcome is presented together with all the other results from previous experiments in Table 8.1 and Figure 8.1.

Year	Experiment	η mass (MeV/c^2)	Stat. error (MeV/c^2)	Sys. error (MeV/c^2)
2012	COSY-ANKE [G+12]	**547.873**	0.005	0.027
2012	MAMI-CB (prel.) [Nik12]	**547.851**	0.031	0.062
2007	DAFNE-KLOE [M+07b]	**547.874**	0.007	0.029
2007	CESR-CLEO [A+07b]	**547.785**	0.017	0.057
2005	COSY-GEM [AB+05]	**547.311**	0.028	0.032
2002	CERN/SPS-NA48 [L+02]	**547.843**	0.030	0.041
1995	MAMI-TAPS [K+95]	**547.120**	0.060	0.250
1992	SATURNE-SPES [P+92]	**547.300**	0.150	
1974	Ruth.Lab. [D+74]	**547.450**	0.250	

Table 8.1.: Results of different η mass measurements in chronological order. The notation "Experiment" comprises the used accelerator facility and detector.

The η meson mass obtained is consistent with all recent measurements in which the meson decay products were studied [L+02, A+07b, M+07b, Nik12]. The precision achieved is similar to these works. It is important to underline the fact that the deviation from the PDG best value [N+10] is only 20 keV/c^2 which is less than the systematic error. The COSY-ANKE outcome is the first missing mass experiment that strengthens the higher η mass value. So the hypothesis of background distortion under the η peak, which might cause a shift in the missing mass, must be discarded (see Section 5.4).

It is worth to emphasise the almost perfect agreement with the KLOE result. It is expected that together with the KLOE outcome the PDG estimation will be shifted to a higher value in near future.

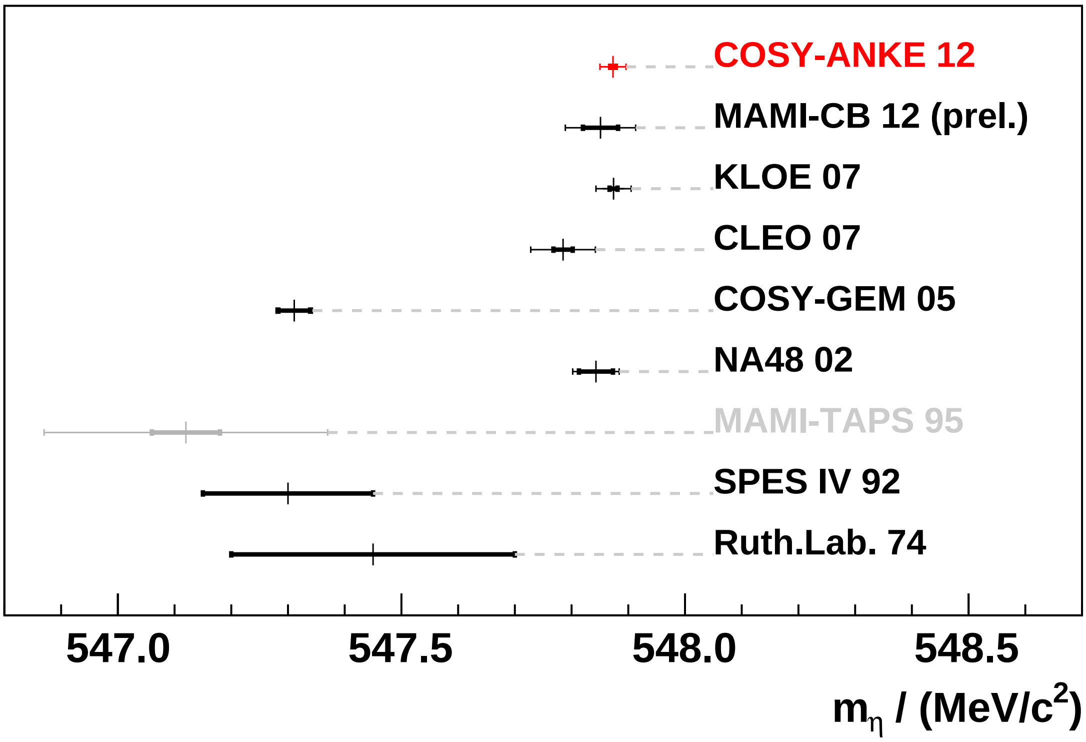

Figure 8.1.: Results of different η mass experiments. It is only where two error bars are shown, the heavy line indicates the statistical uncertainty and the faint one the systematic. The earlier missing mass experiments, marked Rutherford Laboratory 74 [D$^+$74], SPES IV 92 [P$^+$92], and COSY-GEM 05 [AB$^+$05], all obtained low values for m_η compared to recent experiments identifying the meson by its decay products, viz. NA48 02 [L$^+$02], CLEO 07 [M$^+$07b], KLOE 07 [A$^+$07b], and MAMI-CB 12 [Nik12]. The COSY-ANKE outcome is completely consistent with these more refined experiments.

The final success of COSY-ANKE is based upon precise determination of the beam momentum using the resonant depolarisation technique [Gos08, G$^+$10], clear identification of the η signal, and systematic study of the measurement of the $^3\mathrm{He}\,\eta$ final state momentum in the ANKE spectrometer [G$^+$12]. The latter one was only made possible by the complete geometric acceptance of ANKE for the $\mathrm{d\,p} \to {}^3\mathrm{He}\,\eta$ reaction close to threshold. Consequently, this allowed to verify if the CM momentum in the final state is identical in all directions as demanded by kinematics. This

symmetry requirement is a powerful technique for calibration purposes, that might be useful for other two-body reactions, too.
Unlike the MAMI methodology focussed on yields [Nik12], the COSY-ANKE experiment is purely based on kinematics to determine the threshold momentum and thus the meson mass. However, it is important to keep in mind that the anomalous behaviour of the production cross section, where the cross section jumps so rapidly with excess energy, leads to the desirable high count rates near threshold.

The most accurate result for the η meson mass from COSY-ANKE differs by about $0.5\,\mathrm{MeV/c^2}$ from earlier missing mass evaluations [D+74, P+92, AB+05]. An intense discussions with scientists of the other missing mass experiments could not explain and clarify this discrepancy. It is, of course, impossible to speak for other experiments, but never mind, at this points the effects revealed in the COSY-ANKE analysis, which, in the end, would lead to a lower η mass value, will be shortly summarised.
The careful analysis of the $\mathrm{d\,p} \to {}^3\mathrm{He}\,\eta$ reaction showed a deviation of the measured quantities, i.e., missing mass as well as final state momentum, from the kinematically correct one due to resolution effects. In the case of ANKE the strength for the difference depends on the production angle $\cos\vartheta$ and azimuthal angle ϕ. This is due to different resolutions and smearings of the three momentum components (p_x, p_y, p_z). Such effects must be quantified as well as disentangled in the analysis for a precise mass determination.
In particular, if ANKE had access to events scattered in forward and backward direction, only, one would found a deviation to a lower mass value of about $\approx 500\,\mathrm{keV/c^2}$. It is without consideration of these resolution and smearing effects that the missing mass will shift to $\approx 547{,}3\,\mathrm{MeV/c^2}$ showing clearly the influence on the final result.
If the detector has full geometrical acceptance, so that all the events on the whole momentum sphere of the two-body reaction are taken into account, even then one will always find a smaller deviation for the missing mass. In the case of the COSY-ANKE experiment the is shift is about $\approx 150\,\mathrm{keV/c^2}$ to a lower mass value. This shows very clearly that it is of highest importance to factor in such effects from resolution when determining particle masses.

Finally, twelve energies above threshold were investigated, allowing a reliable extrapolation for fixing the production threshold. Such an approach is intrinsically subject to far fewer systematic uncertainties than a measurement at a single energy. Therefore, it is very evident that a missing mass approach taken with care can compete with experiments reconstructing the η mesons by its decay products.

A. Appendix

A.1. Invariant Mass and Missing Mass

Depending on construction and components of a detector facility and on the particle properties it is obviously not always possible to measure or detect directly all particles produced at nuclear reactions. As described in Section 2.2 especially unstable neutral charged particles, like the η meson, can only be reconstructed and identified indirectly by the calculation of the invariant mass of its decay products or by the determination of the missing mass.

Invariant Mass of decay products

There are two possible ways how particles can be produced in scattering experiments. On the one hand they can be directly produced at various reactions and on the other hand they can be generated by decays of heavier particles. The decay of a particle x, which is not directly detectable, into lighter ones a, b, c is completely described by energy and momentum conservation via the relation of the four momentum vectors:

$$\mathbb{P}_x = \mathbb{P}_a + \mathbb{P}_b + \mathbb{P}_c \ . \tag{A.1}$$

According to Equations (3.1) and (3.2) and due to "Minkowski metric" the absolute of the sum of the four momenta of the particle system a, b, c gives the rest mass m_x of the particle x:

$$m_x = |\mathbb{P}_a + \mathbb{P}_b + \mathbb{P}_c| \ . \tag{A.2}$$

If the four momenta of the particles a, b, c, produced in a scattering experiment and detected with a detector are reconstructed the invariant mass (IM) spectrum can be determined via:

$$\mathrm{IM} = |\mathbb{P}_a + \mathbb{P}_b + \mathbb{P}_c| \ . \tag{A.3}$$

Particles coming from the direct production create a continuous distribution defined by the reaction's kinematics and cross sections. Particles from the decay of the heavier particle x create due to Equation (A.2) a peak at the particle's mass m_x in the invariant mass spectrum. In this way the unstable and not directly detectable particle x can be reconstructed and identified.

Missing Mass reconstruction at a two-body reaction

Another method to reconstruct a not detectable particle or particle system x, that is produced in the reaction $a\,b \to c\,x$, is given by the calculation of the missing mass spectrum. The reaction kinematics is specified entirely by the four momentum equation

$$\mathbb{P}_a + \mathbb{P}_b = \mathbb{P}_c + \mathbb{P}_x \;, \tag{A.4}$$

whereas the four momenta of the initial state are given exclusively by energy and momentum of the accelerator beam and the target. If the particle c is detected with the detector setup and its four momentum reconstructed, the missing mass MM of the particle or particle system x will be defined by

$$\mathrm{MM}(\mathbb{P}_c) = |\mathbb{P}_a + \mathbb{P}_b - \mathbb{P}_c| = \mathbb{P}_x = m_x \tag{A.5}$$

and with it the invariant mass is determined. In the case that x is a particle system a continuous missing mass distribution is calculated, which is defined by the kinematics of this system, i.e., by the relative movement of the components. If the reaction described by Equation (A.4) is a two-body reaction the missing mass determination will give the rest mass of the particle x and the missing mass spectrum will show a peak at the value of m_x. The width of this peak is defined by the decay width of the particle and the detector resolution for measuring $\mathbb{P}_c$. of the accelerator beam and the target.

A.2. Polynomial approximation method for momentum reconstruction

All three components of the particle's momentum in the laboratory system $\vec{p}_{\mathrm{LS}}$ are approximated by a third order polynomial when using the polynomial approximation method [V+91]

$$p_i = \sum_{k,l,m,n=0}^{3} C^i_{k,l,m,n} x^k y^l \tan^m(\theta_{xz}) \tan^n(\theta_{yz}) \ , \tag{A.6}$$

with four track parameters

$$\tan(\theta_{xz}),\ \tan(\theta_{yz}),\ x,\ y\ . \tag{A.7}$$

Thereby x and y represent the track coordinates on the D2 forward exit window and $\tan(\theta_{xz})$ and $\tan(\theta_{yz})$ are the angles when projecting the particle's track on the xz and yz plane. In order to fix these parameters the straight track, reconstructed with the track finding algorithm, is interpolated onto the D2 exit window. The polynomial coefficients $C^i_{k,l,m,n}$ are determined from a typical teaching sample of events, produced by Geant4 simulations. This method is nearly 30% faster than the Runge-Kutta-Nyström tracing, but relies on an accurate implementation of the ANKE detector in simulations.

A.3. ^{3}He meson production at COSY-ANKE

After having applied the ^{3}He event selection cuts the different mesonic contributions of ^{3}He meson production become visible in the final state momentum distribution. Due to their different masses the η production corresponds to the peak at lowest final state momenta, whereas the single π^0 production appears as a peak at $\approx$ 0.5 GeV/c. The two pion production is present as a continuous distribution, because it is produced in a three particle reaction for that only the ^{3}He nuclei is measured. It is mainly responsible for the continuous distribution from $0.1 - 0.45$ GeV/c.

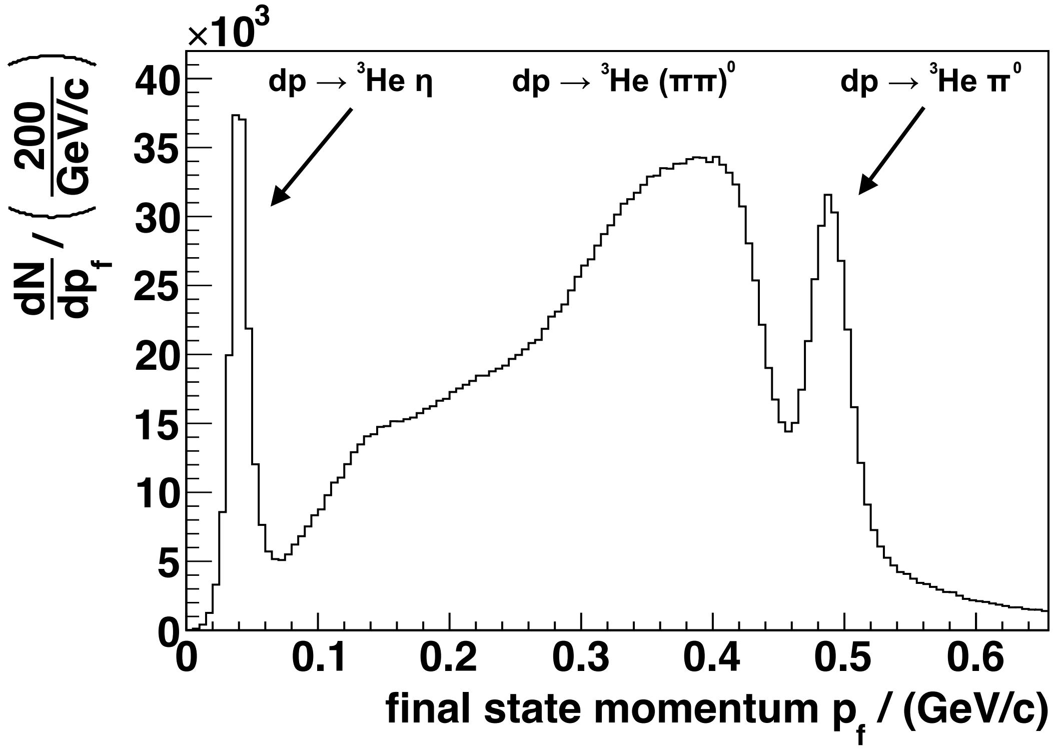

Figure A.1.: The ^{3}He final state momentum distribution after having applied the ^{3}He event selection cuts. The different components, i.e. single π^0, $(\pi\pi)^0$, and η production, are visible.

A.4. Background description for all energies

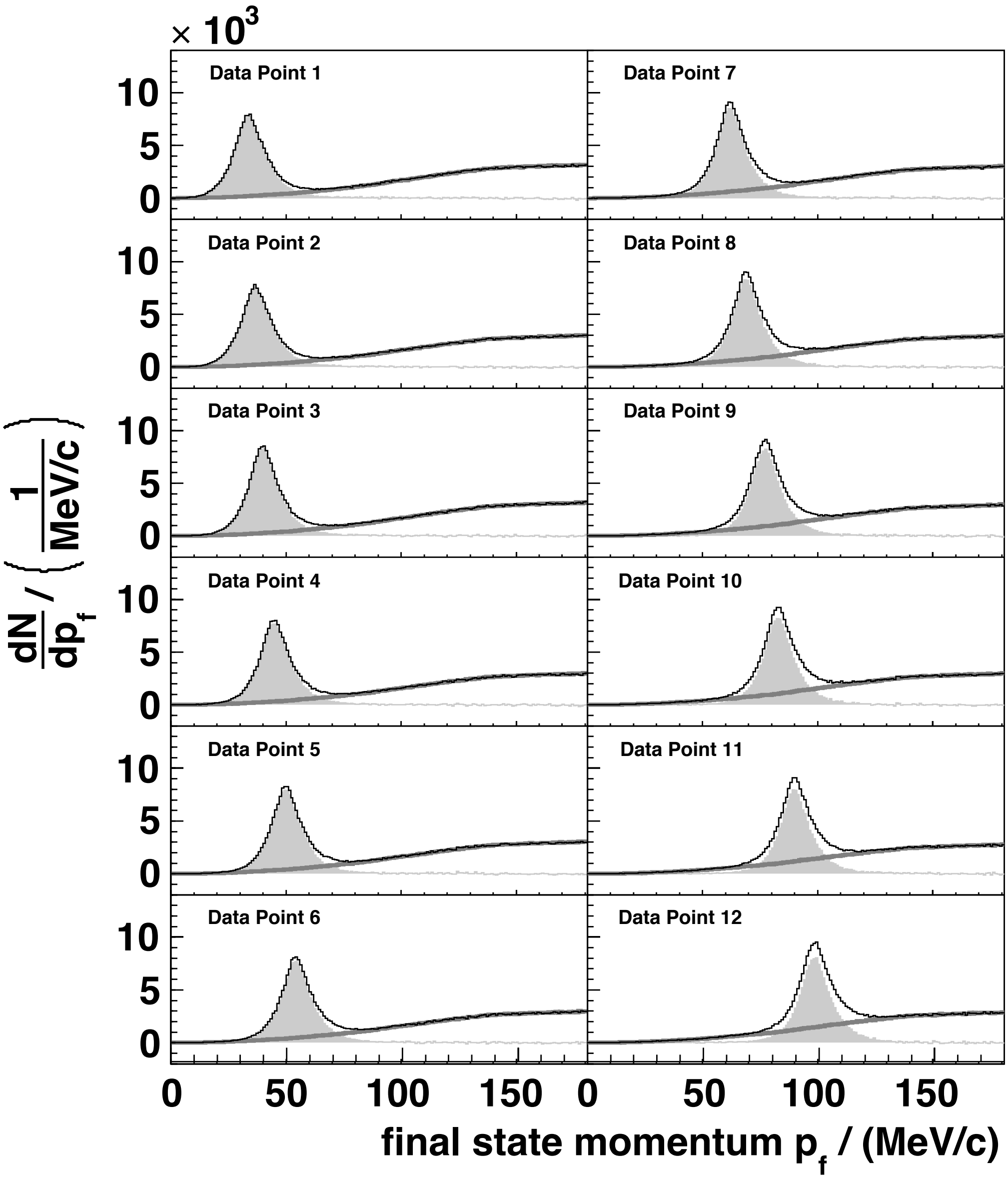

Figure A.2.: The CM distribution of the ^{3}He momentum, i.e., final state momentum, from the $\mathrm{d\,p} \rightarrow {}^3\mathrm{He}\,\eta$ reaction is shown for all twelve energies studied above threshold. The measured data after event selection is shown as black line, the background estimated from subthreshold data as grey line, and the resulting background-subtracted $\mathrm{d\,p} \rightarrow {}^3\mathrm{He}\,\eta$ signal is shaded grey.

A.5. Results of calibration fine tuning

For the sake of completeness, the changes of the calibration parameters between the standard calibration and the fine tuning (see Section 6.3) are summarised in the following.

The vertical position of the 2^{nd} MWPC was changed from 0.7348 mm to 0.3397 mm on the y-axis in order to correct for p_y. For adjusting p_x the deflection angle of the COSY beam caused by the D1 magnet was optimised and for p_z the magnetic field strength of the D2 magnet. The changes made for all twelve energies are summarized in Table A.1.

Data	Magnetic field strength of D2		Deflection angle of beam	
Points	Standard Cali.	Fine Tuning	Standard Cali.	Fine Tuning
1	1.4162	1.4152	5.803	5.799
2	1.4167	1.4157	5.807	5.804
3	1.4172	1.4159	5.803	5.808
4	1.4182	1.4169	5.807	5.811
5	1.4192	1.4181	5.804	5.805
6	1.4202	1.4196	5.808	5.805
7	1.4223	1.4215	5.805	5.810
8	1.4243	1.4236	5.811	5.808
9	1.4268	1.4260	5.805	5.809
10	1.4289	1.4283	5.813	5.802
11	1.4314	1.4308	5.806	5.796
12	1.4350	1.4343	5.816	5.793

Table A.1.: Comparison between calibration parameters for the standard calibration and after having fine tuned the ANKE spectrometer.

A.6. Agreement between data and smeared simulations

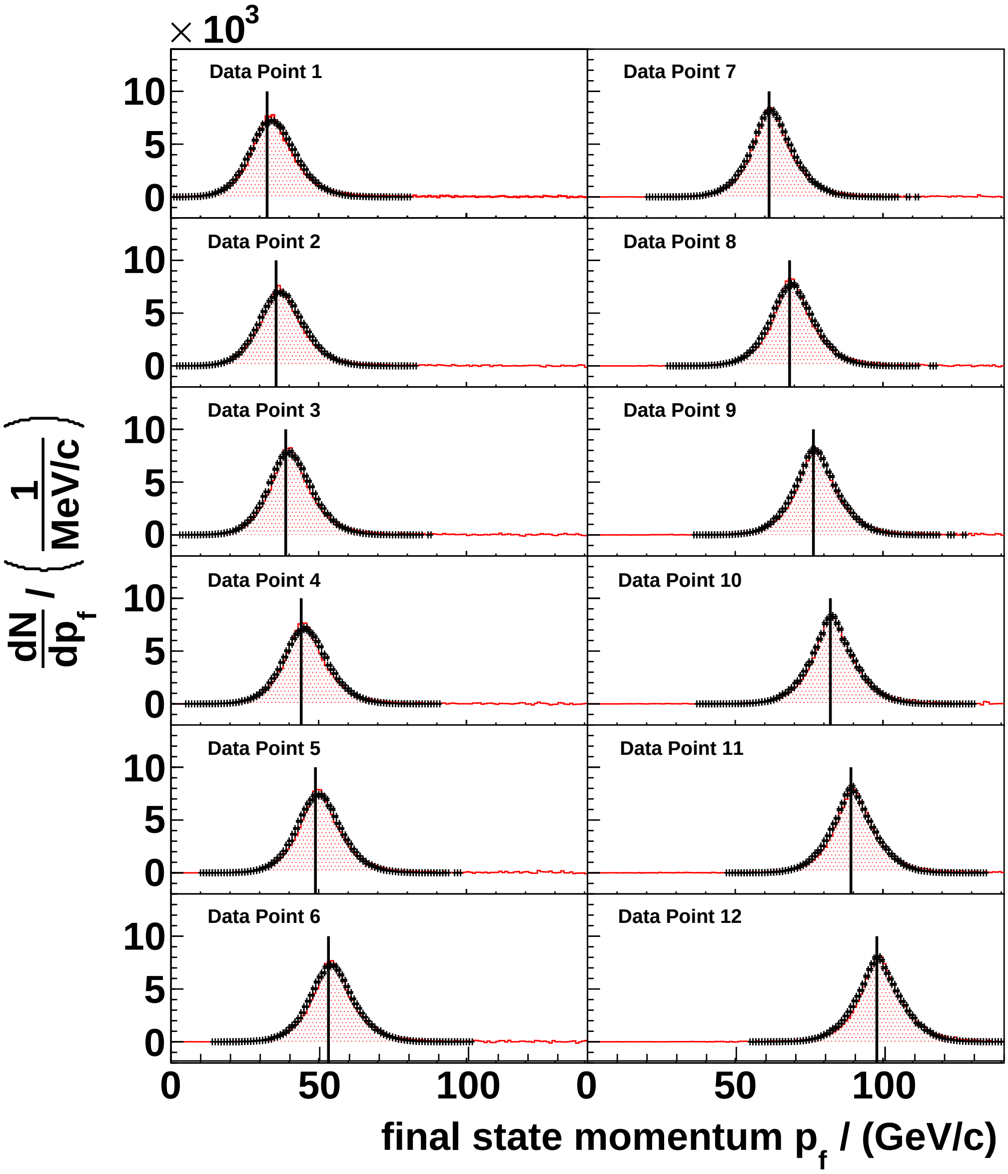

Figure A.3.: Final state momentum distributions for background subtracted $\mathrm{d}\,\mathrm{p} \to {}^{3}\mathrm{He}\,\eta$ data (filled red area) and Monte Carlo simulations including resolution effects (black crosses) for all twelve energies. The figure emphasises the excellent agreement between data and simulations. The vertical line indicates the kinematically correct final state momentum.

Bibliography

[A$^+$82] A.S. Artamonov et al. A high precision measurement of the Υ-meson mass. *Physics Letters B*, 118:225–229, 1982.

[A$^+$92] L. Arnaudon et al. Measurement of lep beam energy by resonant spin depolarization. *Physics Letters B*, 284:431–439, 1992.

[A$^+$03] V.M. Aulchenko et al. New precision measurement of the J/ψ- and ψ'-meson masses. *Physics Letters B*, 573:63–79, 2003.

[A$^+$05] M. Altmeier et al. Excitation functions of the analyzing power in elastic proton-proton scattering from 0.45 to 2.5 GeV. *European Physical Journal A*, 23:351–364, 2005.

[A$^+$07a] F. Ambrosino et al. Measurement of the slope parameter α for the $\eta \to 3\pi^0$ decay at KLOE. http://arxiv.org/abs/0707.4137v1, July 2007.

[A$^+$07b] F. Ambrosino et al. Precise measurements of the η meson and the neutral kaon masses with the KLOE detector. *Journal of High Energy Physics*, 0712:073, 2007.

[AB$^+$05] M. Abdel-Bary et al. A precision determination of the mass of the η meson. *Physics Letters B*, 619:281–287, 2005.

[ABC60] A. Abashian, N.E. Booth, and K.M. Crowe. Possible anomaly in meson produciton in p+d collisions. *Physical Review Letters*, 5(6):258–260, 1960.

[ATL12] Collaboration ATLAS. Observation of a new particle in the search for the Standard Model Higgs boson with the ATLAS detecter at the LHC. *Physics Letters B*, 716:1–29, 2012.

[B$^+$62] P.L. Bastien et al. Decay modes and width of the η meson. *Physical Review Letters*, 8(3):114–117, 1962.

[B$^+$84] D.P. Barber et al. A precision measurement of the Υ' meson mass. *Physics Letters B*, 135:498–504, 1984.

[B+87] A.D. Bukin et al. The phi meson: Precision measurement of its mass, observation of the omega phi interference. *Yadernaya Fizika*, 27:976, 1987.

[B+01] S. Barsov et al. ANKE, a new facility for medium energy hadron physics at COSY-Jülich. *Nuclear Instruments and Methods in Physics Research A*, 462:364–381, 2001.

[Ber09] F. Bergmann. *Studien zum seltenen Zerfall des η-Mesons $\eta \to \pi^0 + e^+ + e^-$ am Experimentaufbau WASA-at-COSY*. Diplomarbeit, Westfälische Wilhelms-Universität Münster, 2009.

[Ber13] F. Bergmann. *In preperation*. PhD thesis, Westfälische Wilhelms-Universität Münster, 2013.

[BK73] E. Byckling and K. Kajantie. *Particle Kinematics*. John Wiley and Sons, 1973.

[BLN90] B. Bagchi, A. Lahiri, and S. Niyogi. $\eta' - \eta - \pi^0$ mixing. *Physical Review D*, 41(9):2871–2876, 1990.

[BM81] L. Bugge and J. Myrheim. Tracking and track fitting. *Nuclear Instruments and Methods*, 179:365–381, 1981.

[BMT59] V. Bargmann, L. Michel, and V.L. Telegdi. Precession of the polarization of particles moving in a homogeneous electromagnetic field. *Physical Review Letters*, 2:435–436, 1959.

[Bou87] D. Boussard. Schottky noise and beam transfer function diagnostics. In S. Turner, editor, *Proceedings of CERN Accelerator School: Advanced Accelerator Physics*, volume CERN 87-03, pages 416–452, 1987.

[C+02] B. Chiladze et al. The forward detector of the ANKE spectrometer. Scintillation and cherenkov hodoscopes. *Particles and Nuclei, Letters*, 113(4):95–100, 2002.

[CMS12] Collaboration CMS. Observation of a new boson at a mass of 125 gev with the cms experiment at the lhc. *Physics Letters B*, 716:30–61, 2012.

[D+74] A. Duane et al. New Upper Limit on the Width of the $X^0(958)$. *Physical Review Letters*, 32(8):425–428, 1974.

[D+80] Ya.S. Derbenev et al. Accurate calibratoin of the beam energy in a storage ring based on measurement of spin precession frequency of polarized particles. *Particle Accelerators*, 10:177–180, 1980.

[D+97] H. Dombrowski et al. The Münster cluster target for internal storage ring experiments. *Nuclear Instruments and Methods in Physics Research A*, 386:228–234, 1997.

[D+04] S. Dymov et al. The forward detector of the ANKE spectrometer. Tracking system and its use in data analysis. *Particles and Nuclei, Letters*, 119(2):40–53, 2004.

[Dym01] S. Dymov. An approach for tuning the FD momentum scale. ANKE internal notes, 2001.

[Dym09] S. Dymov. Fd momentum calibration for March08 beam time. ANKE internal notes, March 2009.

[Dym12] S. Dymov. Momentum calibration of the η mass beam time. Private communication, 2012.

[EB64] F. Englert and R. Brout. Broken symmetry and the mass of gauge vector mesons. *Physical Review Letters*, 13(9):321–323, 1964.

[Fri11] Christopher Fritzsch. *Energiekalibrierung für das ANKE-Experiment.* Bachelorarbeit, Westfälische Wilhelms-Universität Münster, 2011.

[Fri13] Christopher Fritzsch. *In preperation.* Masterarbeit, Westfälische Wilhelms-Universität Münster, 2013.

[G+10] P. Goslawski et al. High precision beam momentum determination in a synchrotron using a spin-resonance method. *Physical Review Special Topics - Accelerators and Beams*, 13:022803, 2010.

[G+11] P. Goslawski et al. COSY Proposal and Beam Time Request: Investigation of the η^3H final state in deuteron-neutron collisions at ANKE. http://collaborations.fz-juelich.de/ikp/anke/proposal/ProposalDDtoTEtaP.pdf , 25.03.2013, April 2011.

[G+12] P. Goslawski et al. New determination of the mass of the η meosn at COSY-ANKE. *Physical Review D*, 85:112011, 2012.

[GAMM83] J.E. Griffin, C. Ankenbrandt, J.A. MacLachlan, and A. Moretti. Isolated Bucket RF Systems in the Fermilab Antiproton Facility. *IEEE Transactions on Nuclear Science*, NS-30(4), 1983.

[GM62] M. Gell-Mann. Symmetries of Baryons and Mesons. *Physical Review*, 125(3):1067–1084, 1962.

[Gos08] P. Goslawski. *Hochpräzise Impulsbestimmung des COSY-Beschleunigerstrahls im Rahmen der Messung zur Bestimmung der η-Masse am Experimentaufbau ANKE*. Diplomarbeit, Westfälische-Wilhelms-Universität Münster, December 2008.

[H+99] F. Hibou et al. Near-Threshold Production of ω Mesons in the $pp \rightarrow pp\omega$ Reaction. *Physical Review Letters*, 83(3):492–495, 1999.

[Hag63] R. Hagedorn. *Relativistic Kinematics*. W. A. Benhamin, Inc., 1963.

[Hig64] P. W. Higgs. Broken symmetries and the masses of gauge bosons. *Physical Review Letters*, 13(16):508–509, 1964.

[Hin08] F. Hinterberger. *Physik der Teilchenbeschleuniger und Ionenoptik*. Springer-Verlag, 2008.

[HL86] Q. Haider and L.C. Liu. Formation of an eta-mesic nucleus. *Physics Letters B*, 172(2):257–260, May 1986.

[K+95] B. Krusche et al. Mass and $\Gamma_{3\pi^0}/\Gamma_{\gamma\gamma}$ decay branching ration of the η-meson from the $\mathrm{p}(\gamma,\eta)\mathrm{p}$ reaction. *Zeitschrift für Physik A*, 351:237–240, 1995.

[K+99] A. Khoukaz et al. Systematic studies on hydrogen cluster beam production. *European Physical Journal D*, 5:275–281, 1999.

[K+06] A. Khoukaz et al. COSY Proposal and Beam Time Request: Investigation of the ^{3}He η final state in the $\vec{d}p \rightarrow {}^3\mathrm{He}\,\eta$ reaction at ANKE. http://collaborations.fz-juelich.de/ikp/anke/proposal/New_proposal_eta.ps , 25.03.2013, April 2006.

[K+12] A. Khoukaz et al. COSY Proposal and Beam Time Request: Measurement of the quasi-free $pn \rightarrow d\eta$ cross section at ANKE. http://collaborations.fz-juelich.de/ikp/anke/proposal/Proposal_211_pndeta.pdf , 25.03.2013, April 2012.

[Kho07] A. Khoukaz. COSY Proposal and Beam Time Request: Precision Measurement of the η Mass at COSY. http://collaborations.fz-juelich.de/ikp/anke/proposal/public_proposal_187.pdf , 25.03.2013, November 2007.

[Köh10] E. Köhler. *Das Münsteraner Cluster-Jet Target MCT2, ein Prototyp für das PANDA-Experiment, und die Analyse der Eigenschaften des Clusterstrahls*. Diplomarbeit, Westfälische-Wilhelms-Universität Münster, Februar 2010.

[Köh13] E. Köhler. *In preperation.* PhD thesis, Westfälische Wilhelms-Universität Münster, 2013.

[KSTY85] N. Katayama, F. Sai, T. Tsuboyama, and S.S. Yamamoto. Measurement of dp cross sections in the momentum range 2.0-3.7 GeV/c. *Nuclear Physics A*, 438:685–696, 1985.

[L$^+$02] A. Lai et al. New measurements of the η and K^0 masses. *Physics Letters B*, 533:196–206, 2002.

[L$^+$03] A. Lehrach et al. Acceleration of Polarized Protons and Deuterons at COSY. *AIP Conference Proceedings*, 675:153, 2003.

[L$^+$04] M.A. Leonova et al. Achieving 99.9% proton spin-flip efficiency at higher energy with a small rf diploe. *Physical Review Letters*, 93:224801, 2004.

[Lee97] S.Y. Lee. *Spin Dynamics and Snakes in Synchrotrons*. World Scientific Publishing Co. Pte. Ltd., 1997.

[Lee07] S.Y. Lee. *Accelerator Physics*. World Scientific Publishing Co. Pte. Ltd., 2007.

[Leh97] A. Lehrach. *Erarbeitung und Umsetzung eines Konzepts zur Beschleunigung polarisierter Protonen im Kühlersynchrotron COSY*. PhD thesis, Rheinische Friedrich-Wilhelms-Universtität Bonn, 1997.

[LPS86] A.P. Lysenko, A.A. Pilunin, and Yu.M. Shatunov. Spin-frequency spread measrurements in a storage ring. *Particle Accelerators*, 18:215–222, 1986.

[M$^+$84] W.W. MacKay et al. Measurement of the Υ mass. *Physical Review D*, 29(11):2483–2490, 1984.

[M$^+$04] V.S. Morozov et al. Spin manipulation of 1.94 GeV/c polarized protons stored in the COSY cooler synchrotron. *Physical Review Special Topics - Accelerators and Beams*, 7:024002, 2004.

[M$^+$05] V.S. Morozov et al. Spin manipulating stored 1.85 GeV/c vector and tensor polarized spin-1 bosons. *Physical Review Special Topics - Accelerators and Beams*, 8:061001, 2005.

[M$^+$07a] T. Mersmann et al. Precision study of the η^3He system using the $dp \to {}^3\mathrm{He}\eta$ reaction. *Physical Review Letters*, 89:242301, 2007.

[M$^+$07b] D. H. Miller et al. Measurements of the η-Meson Mass Using $\psi(2S) \to \eta J/\psi$. *Physical Review Letters*, 99:122002, 2007.

[Mai97] R. Maier. Cooler synchrotron COSY - performance and perspectives. *Nuclear Instruments and Methods in Physics Research A*, 390:1–8, 1997.

[MB79] J. Myrheim and L. Bugge. A fast Runge-Kutta method for fitting tracks in a magnetic field. *Nuclear Instruments and Methods*, 160:43–48, 1979.

[Mer03] T. Mersmann. *Untersuchungen zur Proton-Deuteron-Streuung an einem Deuterium Clusterstrahl am Magnetspektrometer ANKE*. Diplomarbeit, Westfälische Wilhelms-Universität Münster, 2003.

[Mer07] T. Mersmann. *Untersuchung der Wechselwirkung zwischen η-Mesonen und* ^{3}He-*Kernen am Experimentaufbau ANKE*. PhD thesis, Westfälische Wilhelms-Universität Münster, 2007.

[Mie13] M. Mielke. *In preperation.* PhD thesis, Westfälische Wilhelms-Universität Münster, 2013.

[MTN12] P.J. Mohr, B.N. Taylor, and D.B. Newell. CODATA Recommanded Values of Fundamental Physical Constant: 2010*, National Institute of Standards and Technology, Gaithersburg, Maryland 20899-8420, USA. http://physics.nist.gov/constants, March 2012.

[N$^+$10] K. Nakamura et al. (Particle Data Group). *Journal of Physics G*, 37:075021, 2010.

[Nik11] A. Nikolaev. Private communication, November 2011.

[Nik12] A. Nikolaev. *Determination of the η mass from the production threshold for the $\gamma p \to p\eta$ reactoin.* PhD thesis, Rheinische Friedrich-Wilhelms-Universtität Bonn, 2012.

[oC12] $\overline{\text{P}}$ANDA Collaboration. The Cluster-Jet Target and Developments for the Pellet Target. Technical report, not yet published, 2012.

[Ohl72] G.G. Ohlsen. Polarization transfer and spin correlation experiments in nuclear physics. *Reports on Progress in Physics*, 35:717–801, 1972.

[P$^+$61] A. Pevsner et al. Evidence for a three-pion resonance near 550 Mev. *Physical Review Letters*, 7(11):421–423, 1961.

[P$^+$92] F. Plouin et al. The η-meson mass. *Physics Letters B*, 276:526–530, 1992.

[Pap13] M. Papenbrock. *In preperation.* PhD thesis, Westfälische Wilhelms-Universität Münster, 2013.

[PS08] D. Prasuhn and H. Stockhorst. Independence of the beam momentum on the ion source used. Private communication, 2008.

[PZ02] A.Yu. Petrus and B.Zh. Zalikhanov. Electro-mechanical properties of narrow-gap multiwire proportinal chambers. *Nuclear Instruments and Methods in Physics Research A*, 485:399–410, 2002.

[R+09] T. Rausmann et al. Precision study of the $dp \to {}^3\mathrm{He}\eta$ reaction for excess energies between 20 and 60 MeV. *Physical Review C*, 80:017001, 2009.

[Rau09] T. Rausmann. *Untersuchung der Reaktion $d + p \to {}^3\mathrm{He} + \eta$ im Bereich zwischen 20 und 60 MeV Überschussenergie am Experimentaufbau ANKE.* PhD thesis, Westfälische Wilhelms-Universität Münster, 2009.

[S+76] S.I. Serednyakov et al. Study of the radiative polarization of beams in the VEPP-2M storage ring. *Zh. Eksp. Teor. Fiz.*, 71:2025–2032, 1976.

[S+07a] H. Stockhorst et al. Beam-energy calibration. Internal note, October 2007.

[S+07b] H. Stockhorst et al. RF-Solenoid and Beam-Energy Calibration. *Forschungszentrum Jülich, Institut für Kernphysik, Annual Report 2007*, pages 22–23, 2007.

[S+08a] V. Serdyuk et al. Drift Chambers for the ANKE Forward Detector. Technical report, IKP Forschungszentrum Jülich, 2008.

[S+08b] R. Stassen et al. The HESR rf-system and tests in COSY. *Proceedings of EPAC08, Genoa, Italy*, A04 Circular Accelerators:361–363, 2008.

[S+08c] H.J. Stein et al. Determination of target thickness and luminosity from beam energy losses. *Physical Review Special Topics - Accelerators and Beams*, 11(052801), 2008.

[Sch18] W. Schottky. Über spontane Stromschwankungen in verschiedenen Elektrizitätsleitern. *Annalen der Physik*, 362:541–567, 1918.

[Sch99] V. Schwarz. *Kontinuierliche Messung der Polarisation eines Synchrotronstrahls während der Hochbeschleunigung.* PhD thesis, Rheinische Friedrich-Wilhelms-Universtität Bonn, 1999.

[Sch13] D. Schroeer. *In preperation.* PhD thesis, Westfälische Wilhelms-Universität Münster, 2013.

[SKBK01] H.J. Stein, G. Krol, S. Barsov, and V. Koptev. Application and methodological improvements to the floating-wire technique to characterize the magnetic properties of a spectrometer dipole. *Review of Scintific Instruments*, 72:2003–2010, 2001.

[T+11] A. Täschner et al. High density cluster jet target for storage ring experiments. *Nuclear Instruments and Methods in Physics Research A*, 660:22–30, 2011.

[Täs12] A. Täschner. *Entwicklung und Untersuchung von Cluster-Jet-Targets höchster Dichte*. PhD thesis, Westfälische Wilhelms-Universität Münster, 2012.

[Tho27] L.H. Thomas. The kinematics of an electron with an axis. *Phiosophical Magazine*, 7:1–22, 1927.

[V+91] A.D. Volkov et al. Method for the calculation of charged particle momentum in magnetic spectrometers. *Nuclear Instruments and Methods in Physics Research A*, 306:278–282, 1991.

[W+05] A. Wronska et al. Near-threshold η-meson prodcution in the dd $\rightarrow$ ^{4}Heη reaction. *European Physical Journal A*, 26:421–428, 2005.

[W+07] C. Wilkin et al. Is there an η^3He quasi-bound state? *Physics Letters B*, 654:92–96, 2007.

[Win11] A. Winnemöller. *Analyse des verbotenen η-Meson Zerfalls $\eta \rightarrow \pi^0 + e^+ + e-$ am Experimentaufbau WASA-at-COSY*. PhD thesis, Westfälische Wilhelms-Universität Münster, 2011.

[Y+06] W.-M. Yao et al. (Particle Data Group). *Journal of Physics G*, 33:1, 2006.

[Zwe64] G. Zweig. An SU_3 model for strong interaction symmetry and its breaking. CERN Report No. CERN-TH-401, http://cdsweb.cern.ch/record/352337, 1964.

List of Figures

List of Tables

Danksagung - Acknowledgements

Zu guter Letzt möchte ich mich bei allen bedanken, die zum Gelingen dieser Arbeit beigetragen haben.

Mein erster Dank gilt Prof. Dr. Alfons Khoukaz für die Möglichkeit frei und selbstbestimmt mit einem spannenden und umfangreichen Themengebiet promovieren zu dürfen. Vielen Dank für die freundschaftliche Unterstützung, das stets offene Ohr und die wohl dosierten sowie immer passenden und treffenden Worte.

Prof. Dr. J. P. Wessels danke ich für die Übernahme des Korreferats und Priv.-Doz. Dr. J. Heitger für den Einsatz als Drittprüfer.

I wish to express my gratitude to Prof. Dr. H. Ströher, Dr. Andro Kacharava and Prof. Dr. Colin Wilkin for their motivating eagerness to see the final results and alway supporting and "pushing" my work, the resulting publications, and me.
A big "Thank You" to all members of the ANKE collaboration, especially, for your big contributions to the three "Münster" beam times. Thanks to Dr. Sergej Dymov for his calibration of the March 2008 data.
I would also like to thank all members of the WASA collaboration and the people of the IKP at the Forschungszentrum Jülich for their help when (once again) the cluster-jet or pellet target needed to be orpetpiamiirzeedd during beam times.

Der gesamten COSY-Crew danke für die erfolgreiche Zusammenarbeit bei der Strahlimpulsbestimmung und für die Möglichkeit, hin und wieder mit dem Beschleuniger "spielen" zu dürfen. Ein großer Dank gilt der äußerst sympathischen Fußballrunde, die auf Strahlzeiten stets für den sportlichen Ausgleich sorgte.

Des Weiteren möchte ich mich bei der gesamten Arbeitsgruppe "and friends" für die immer freundschaftliche Arbeitsatmosphäre - besser gesagt für den großen Spaß, den wir beim gemeinsamen Forschen hatten - bedanken. Eure zahlreichen und ehrlichen Beiträge auf der Zitatewand werden mir auch zukünftig so manchen Tag aufheitern. Michael Papenbrock danke ich, dass er eine so tolle Linie bei der ANKE Software, die uns das alltägliche Arbeiten erleichtert, vorgegeben hat. Esperanza Köhler und Malte Mielke danke ich für ausdauerndes Korrekturlesen und Diskutieren dieser Arbeit, deren Schreibprozess Sie vom ersten bis zum letzten Tag begleitet haben.

Das fünfte Kapitel möchte ich Hartmut Kühne widmen, der so intensiv wie kein anderer nahezu jeden einzelnen Satz mit mir zusammen studiert hat. Ich möchte Dir für unser gemeinsames Abenteuer in das "physikalische Englisch" danken.

Zuletzt möchte ich mich bei meiner kleinen "Rodzinka" bedanken. Vielen Dank - Julia, Mama, Papa und Michael - für das gemeinsame Promovieren, den starken Rückhalt, für Eure unermüdliche Unterstützung, Euer Vertrauen und Eure Liebe.